ABSTRACT

Title of Thesis: UNDERSTANDING OF LOW REYNOLDS NUMBER AERODYNAMICS AND DESIGN OF MICRO ROTARY-WING AIR VEHICLES

Justin Michael Winslow

Master of Science, 2016

Thesis Directed By: Professor Inderjit Chopra

Department of Aerospace Engineering

The goal of the present research is to understand aerodynamics at low Reynolds numbers and synthesize rules towards the development of hovering micro rotary-wing air vehicles (MRAVs). This entailed the rigorous study of airfoil characteristics at low Reynolds numbers through available experimental results as well as the use of an unsteady Reynolds-Averaged Navier-Stokes solver. A systematic, experimental, variation of parameters approach with physical rotors was carried out to design and develop a micro air vehicle-scale rotor which maximizes the hover Figure of Merit. The insights gained in low Reynolds number aerodynamics have been utilized in the systematic design of a high endurance micro-quadrotor. Based on available characteristics, the physical relations governing electric propulsion system and structural weights have been derived towards a sizing methodology for small-scale rotary-wing vehicles.

UNDERSTANDING OF LOW REYNOLDS NUMBER AERODYNAMICS AND MICRO ROTARY-WING AIR VEHICLES

by

Justin Michael Winslow

Thesis submitted to the Faculty of the Graduate School of the
University of Maryland, College Park, in partial fulfillment
of the requirements for the degree of
Master of Science
2016

Advisory Committee:

Professor Inderjit Chopra, Chair

Associate Professor James Baeder

Assistant Professor Anya Jones

Dedication

To Harambe

Table of Contents

List of Tables

List of Figures

Nomenclature

A	=	rotor disk area, πR^2
C	=	battery capacity
c	=	blade chord
C_d	=	sectional drag coefficient
C_l	=	sectional lift coefficient
C_m	=	sectional moment coefficient
C_P	=	power coefficient, $P/\rho A(\Omega R)^3$
C_T	=	thrust coefficient, $T/\rho A(\Omega R)^2$
d_{BL}	=	brushless motor diameter
d_{DC}	=	brushed DC motor diameter
I	=	electric current
I_{cont}	=	maximum sustainable current
I_{max}	=	maximum burst current
K_v	=	motor speed constant
l_{BL}	=	brushless motor length
l_{DC}	=	brushed DC motor length
m_A	=	airframe weight
m_B	=	battery weight
m_{BL}	=	brushless motor weight
m_{DC}	=	brushed DC motor weight
m_R	=	rotor weight
N_b	=	number of blades
P	=	rotational power
Q_{max}	=	maximum motor torque
R	=	rotor radius
T	=	thrust
t/c	=	thickness-to-chord ratio
α	=	airfoil angle of attack
ρ	=	air density
σ	=	rotor solidity, $N_b c/\pi R$
Ω	=	rotational speed

List of Abbreviations

BEMT	Blade Element Momentum Theory
CFD	Computational Fluid Dynamics
CTR	Chord Taper Ratio, tip chord / root chord
DL	Disk Loading, T/A
EPL	Electric Power Loading, grams per Watt

FM	Figure of Merit
LSB	Laminar Separation Bubble
MAV	Micro Air Vehicle
MRAV	Micro Rotary-wing Air Vehicle
PL	Power Loading, *T/P*
Re	Reynolds Number
RTL	Research and Technology Labs
S	*S*attery cells in series
UAV	Unmanned Aerial Vehicle
VTOL	Vertical Take-Off and Landing

Chapter 1: Introduction

1.1 Motivation

Micro Air Vehicle (MAV) research is a continuously growing field, which is envisioned to have a wide range of military and civilian applications such as search and rescue, reconnaissance, surveillance, as well as terrain and building mapping. By fixing visual, infrared, and chemical sensors to MAVs, they can be used by soldiers as reconnaissance platforms to scout ahead in uncertain environments, as depicted in the various scenarios shown in Figure 1.1. In each of these scenarios, the primary function of the MAV is to minimize the operator's exposure to hazards while providing greater situational awareness at the point-of-need. The small size of MAVs offers several advantages such as portability, rapid deployment, real-time data acquisition capability, low radar cross section, low noise signatures and low production cost. Recent interest has also been generated for Mars exploration MAVs as a fast and mobile alternative to ground-based rovers.

The motivation behind the present research has been driven by various national security agencies such as the Defense Advanced Research Projects Agency (DARPA) and Army Research Laboratory (ARL). These organizations realized the critical role MAVs can fulfill by providing ground soldiers greater situational awareness in confined environments such as buildings and caves. In 1997, DARPA set three goals for MAVs: (1) they must fit within a 6 in. cube, (2) have a gross take-off weight

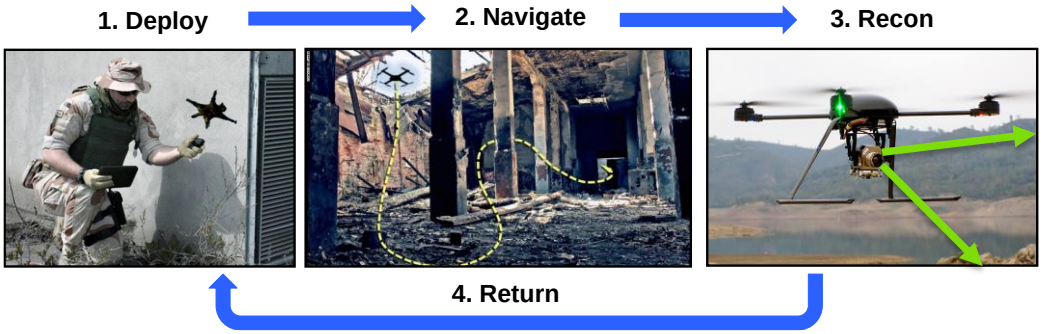

a) Interior Urban Reconnaissance

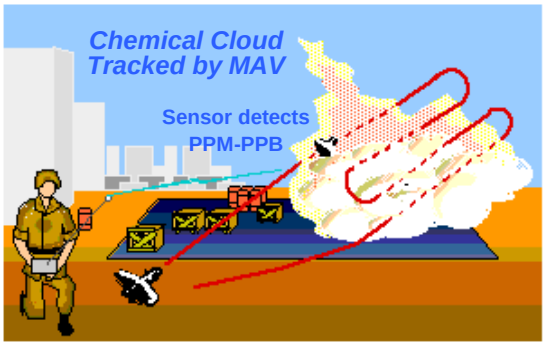

b) Biohazard Sensing[1]

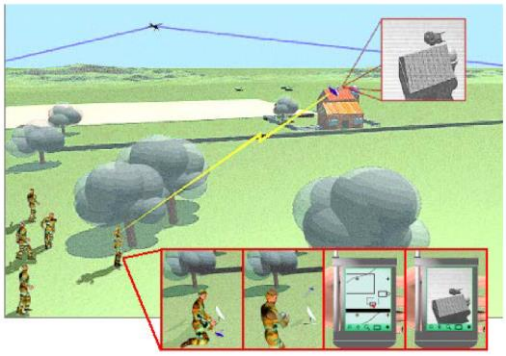

c) Beyond Line-of-Sight Surveillance[1]

Figure 1.1: Potential MAV applications

(GTOW) below 100 g, and (3) have a flight endurance of at least 1 hour[1]. Other agencies with objectives to improve MAV efficiency and design include the NASA Langley Research Center (LaRC) Concept Design Group. Specifically, these groups are focused on developing physics-based sizing and performance algorithms to conceptually model small MAVs. The conceptual models would simplify the design process for MAVs built for specific missions as the need arises. Ideally, this would reduce design-fabricate-assemble-fly time from months to hours by combining proven

sizing and performance models with additive manufacturing processes, such as 3D printing.

Overall, there is a need to make MAVs that are smaller, lighter, easier to design, and fly longer. Reaching these objectives requires greater understanding and improvements in many areas including low Reynolds number aerodynamics, small-scale power transmission, and small-scale sizing relations.

1.2 Previous MAV Development

Even though the concept of MAVs appears attractive, MAV research is still in its incipient stage. It should be noted that less than two decades of research have gone into these vehicles and the key technical barriers are only currently being resolved. Some of these barriers include low Reynolds number aerodynamics, efficient small-scale power generation and storage, ultra-light fabrication processes, robust micro-electronics, out-of-sight navigation and communications, and autonomous control. Various attempts have been made to develop and improve the capabilities of aerial vehicles operating in the low Reynolds number range. Within the MAV category of aircraft, there are three major subcategories: flapping-wing, fixed-wing, and rotary-wing, each with its own advantages and disadvantages.

1.2.1 Flapping-Wing

Flapping-wing MAVs based on insect-kinematics may have the capability for vertical takeoff and landings (VTOL), hovering, high maneuverability, and blending in

with the natural environment. However, these have the least understood aerodynamics, most complex kinematics and control algorithms, and very few successful prototypes. The successful prototypes include AeroVironment's Nano Hummingbird[2], shown in Figure 1.2(a) and the University of Maryland - Texas A&M University flapping wing demonstrator[3]. However, much of the work for these vehicles has been focused on maintaining control and stability. As such, less emphasis has been placed on examining payload capacity or expanding flight endurance. Much more development is needed for flapping wing vehicles to achieve wide-spread practical application.

1.2.2 Fixed-Wing

Fixed-wing MAVs are the most efficient of the MAV configurations and can maintain high flight endurances. Already, multiple fixed-wing models have been successfully built and tested. For example, AeroVironment's Black Widow, shown in Figure 1.2(d), has a wingspan of only 6 in. and a GTOW less than 100 g but can achieve a 30 min. endurance and a 13.4 m/s cruising speed[4]. However, these fixed-wing MAVs do not have hovering capabilities. As a result, they have poor surveillance qualities and cannot navigate restricted interior spaces.

1.2.3 Rotary-Wing

Micro Rotary-wing Air Vehicles (MRAVs), like flapping-wing vehicles, have the ability to hover, but do not sacrifice as much control authority because their lifting surfaces are arranged in a more stable configuration. A typical MRAV is known as a

a) Flapping-wing MAV[2]

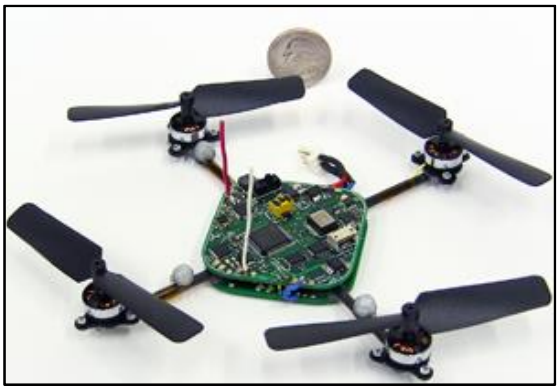

b) Quadrotor MAV[5]

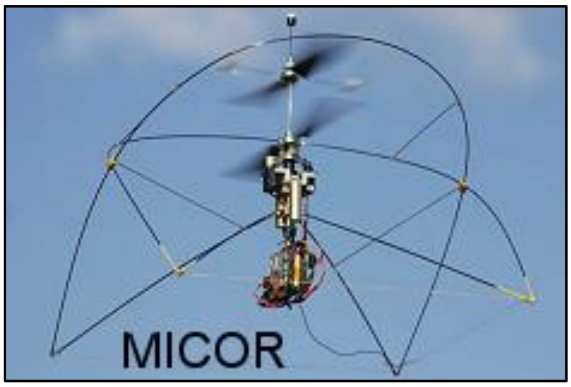

c) Co-axial rotor MAV[6]

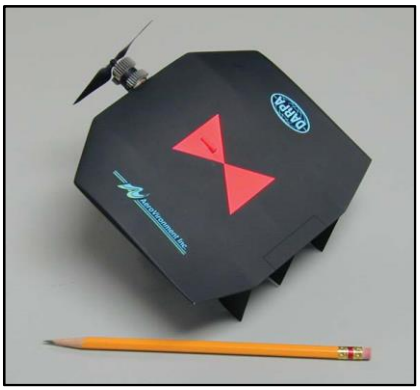

d) Fixed-wing MAV[4]

Figure 1.2: Examples of various MAV configurations

quadrotor since four rotors in a square arrangement provide the necessary thrust, as shown in Figure 1.2(b). This configuration is less mechanically complex than a conventional main rotor and tail rotor configuration and does not require additional devices, such as the tail rotor, to counteract main rotor torque. Furthermore, the symmetric rotor layout allows the quadcopter more quickly pitch and roll for omnidirectional planar movement and permits large shifts in center of gravity.[7] Some co-axial MRAVs have also been developed, as shown in Figure 1.2(c). While MRAVs cannot reach the cruising speeds that fixed-wing MAVs achieve, their higher

maneuverability means they can fly a greater variety of mission profiles, particularly in constrained interior spaces. MRAVs have become increasingly popular among hobbyists and research institutions, such as the University of Pennsylvania GRASP Lab[5], due to their simple mechanics and wide range of applications. For these reasons, rotary-wing MAVs were chosen to be the focus of this thesis.

1.3 Current State of Micro Rotary-wing Air Vehicles

Despite the advances made in quadrotor and multicopter flight dynamics and control within the past decade, they still exhibit very poor flight endurance for their gross weight compared to larger helicopters. This is evident in Table 1, which provides examples of typical MRAVs developed by universities and commercial vendors with

Table 1. Typical MRAV Performance

MAV	Largest Dimension, cm	Weight, g	Endurance, min
Cheerson CX-10 (Quadrotor)[8]	4	15.4	4-8
Heli-Max 1Si (Quadrotor)[9]	13.8	45.9	5
Scorpion Mini Multicopter RTF (Multicopter)[10]	12	55	6.5
DFS/UMD Micro Quad[11]	14.8	59.6	9
QR W100S (Quadrotor)[12]	14.5	89	10
MICOR (Coaxial)[6]	15.24	155	10
Blade Nano QX[13]	14	18	10
GRASP Micro Quadrotor[5]	21	73	11
Liang Mini Quadcopter[14]	24	170	12

their associated flight endurance The MRAVs listed have similar dimensions and weights to the DARPA objectives of 6 in. (15.2 cm) and 100 g GTOW. It should be noted that none of these rotary-wing MAVs listed in Table 1 can achieve even 15 minute flight endurance, meaning their mission capabilities can be quite limited. Even the best performing vehicle, a quadrotor developed by Liang, only has a hover endurance of 12 minutes[14]. Low endurance can be attributed to multiple factors such as rotor/motor efficiency, limited battery storage, and the Reynolds number regime in which these MRAVs operate.

1.4 Low Reynolds Number Challenges

The small scale of these vehicles also means that they operate within a low Reynolds (Re) number range (10,000 – 100,000), which introduces many aerodynamic performance issues. In the MRAV Reynolds number range, viscous forces dominate inertial forces. This results in lower lift-to-drag ratios, more induced losses in the viscous-dominant rotor wake structure, and laminar separation bubbles[15]. At this stage, the state-of-the-art on the aerodynamic characteristics of airfoils at low Reynolds numbers is quite limited.

In previous studies, most researchers have generally focused on high Reynolds numbers in excess of 10^5. However, this excludes the lower Re which is of most interest to MAV designers. In the present research, chord based Re between $10^4 – 10^5$ is defined as the low Re range. This range is two orders of magnitude smaller than those of large-scale conventional aircraft, which typically operate at Re above 10^6. Although large-

scale airfoil characteristics, such as thickness-to-chord ratio (*t/c*), leading edge profile, and camber distribution, have been extensively researched and optimized for decades, these same design characteristics may not be directly applicable to the low Re regime. Figure 1.3 shows the variation of maximum sectional lift-to-drag ratio with Reynolds number and it can be seen that Re has a strong effect on conventional airfoil performance. While conventional airfoils perform best at high Reynolds numbers (10^6 – 10^8), their performance quickly deteriorates at lower Reynolds number and a geometrically simple flat-plate is seen to out-perform the conventional airfoils. Therefore, it is evident that simply trying to downsize these airfoils to low Re scales (Re below 10^5) drastically reduces their aerodynamic efficiency in terms of the lift-to-drag ratio and stall characteristics[16,17]. Consequently, aerodynamic profiles operating in low Re designed with conventional airfoils incur high power requirements because

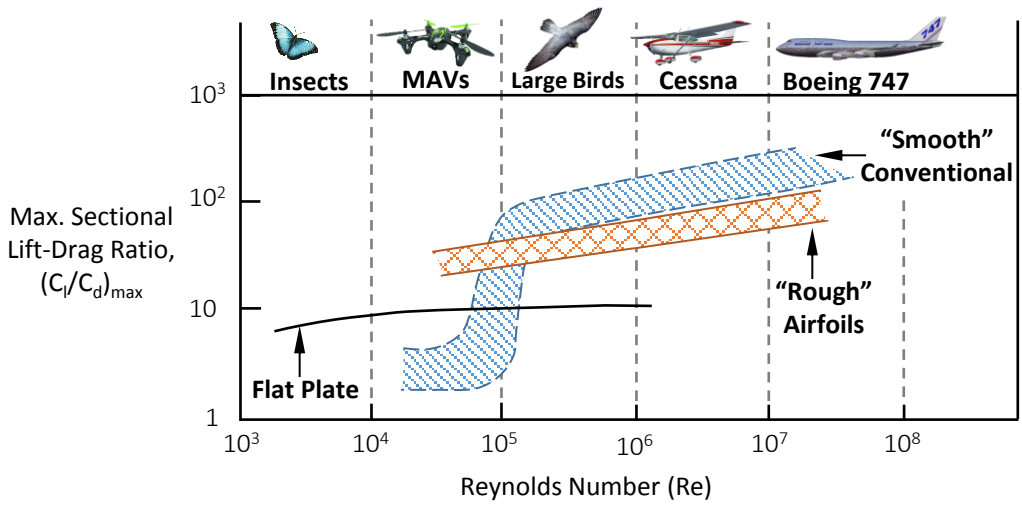

Figure 1.3: Effect of Reynolds number on airfoil maximum sectional lift-to-drag ratio (adapted from [16,17])

of excessive aerodynamic drag. There is a need to systematically understand the characteristics of airfoils at these low Re numbers and their sensitivities to geometric variations, such as camber and thickness.

1.4.1 Flow Physics

Flow field studies, such as particle image velocimetry (PIV), smoke flow visualization, and hot-wire turbulence measurement, have been conducted by researchers to provide physical insight into the effect of Reynolds number, highlighting the difference between low and high Reynolds number flows. The sensitivity of airfoil performance within high or low Re ranges is strongly related to the boundary layer characteristics at a given Re. Figure 1.4 shows a schematic of the flow development over a representative conventional airfoil at various Reynolds numbers.

At higher, more conventional, Re, represented in Figure 1.4(c), laminar flow over the upper airfoil surface is subjected to a large adverse pressure gradient close to the leading edge. Because of the inherently lower kinetic energy of the laminar boundary layer, the flow separates as a shear layer. The shear layer gains momentum from the free-stream, and reattaches as a turbulent boundary layer creating a laminar separation bubble (LSB)[18]. Because the turbulent boundary layer is energized from the free-stream, it is much less prone to separation and usually remains attached until the trailing edge. However, at sufficiently high angles of attack, α, the turbulent boundary layer will begin to separate close to the trailing edge resulting in increased pressure drag and decreased lift. Once the turbulent separation reaches the leading edge, the drag

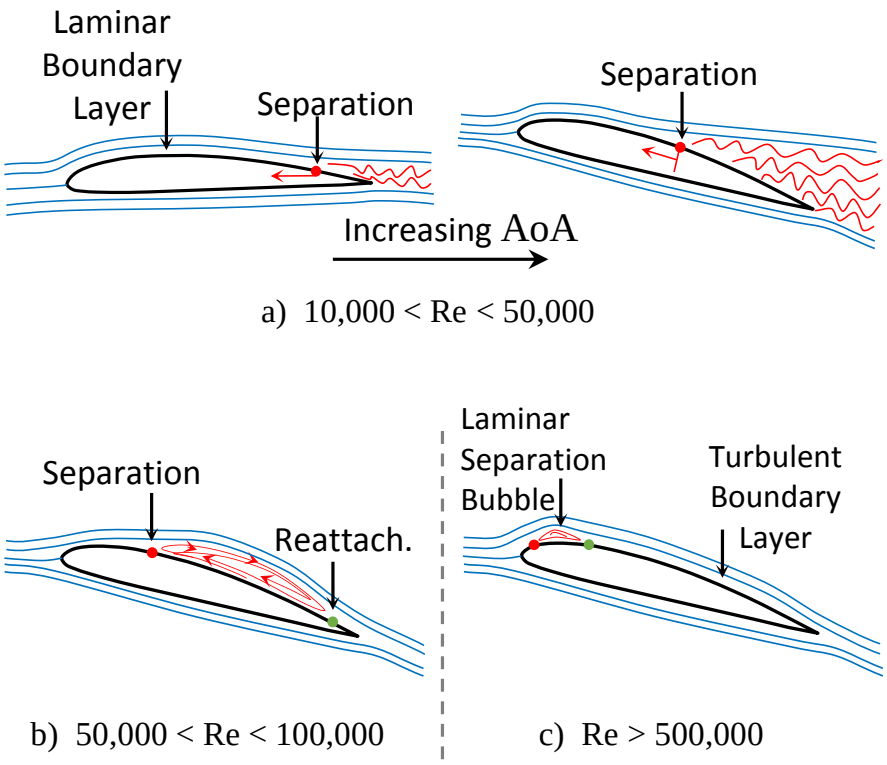

Figure 1.4: Conventional airfoil characteristics at Re < 10^6

rises dramatically, the lift abruptly drops, and the airfoil is considered stalled. This form of separation is known as trailing edge separation and is typically associated with thick, rounded leading edge airfoils.

As Re decreases, the separation bubble and turbulent boundary layer thickness both increases in size, resulting in increased parasitic drag. At $5x10^4$ < Re < 10^5, shown in Figure 1.4(b), the separated shear layer still gains enough momentum from the free-stream to reattach to the airfoil surface as a turbulent boundary layer. However, in this Re range, the reattachment point is relatively far back on the airfoil. As α increases, the reattachment point moves towards the trailing edge, creating relatively large separation

bubbles (15% to 40% chord) [19]. When the airfoil is close to stall α, the flow fluctuates between reattachment and complete separation, resulting in hysteresis which can make lift and drag measurements difficult. At $10^4 < Re < 5x10^4$, shown in Figure 1.4(a), the laminar separation point is delayed until close to the trailing edge, even at very low angles of attack, α [19]. As α increases, the separation point moves towards the leading edge, increasing the separation distance of the shear layer. Unlike at high Re, the shear layer is not able to transition and reattach to the airfoil as a turbulent boundary layer, resulting in high pressure drag and poor lift generation[19]. The airfoil is effectively in trailing edge stall for most or all of its operational range. The trailing edge separation increases in thickness as Re is further decreased for a given angles of attack, resulting in even lower airfoil efficiency[20].

1.4.2 Previous Experimental Airfoil Studies

The effects of decreasing Re on airfoil performance were initially investigated by researchers, such as Schmitz[21], as early as 1930. Schmitz conducted experiments on three airfoils, thin flat plate, thin cambered plate, and a conventional N60 airfoil (12.4% *t/c*, 4% camber) within a Re range of $2x10^4$ to $2x10^5$. This study resulted in two key conclusions, i.e., thin plate airfoils consistently performed better below Re 10^5, and the flow is more susceptible to separation below Re 10^5, especially for the thicker N60. Schmitz named the low Re range in which the flow is more susceptible to separation the "Subcritical" range, as depicted in Figure 1.5. This range is characterized by poor lift generation and high drag due to the flow separation.

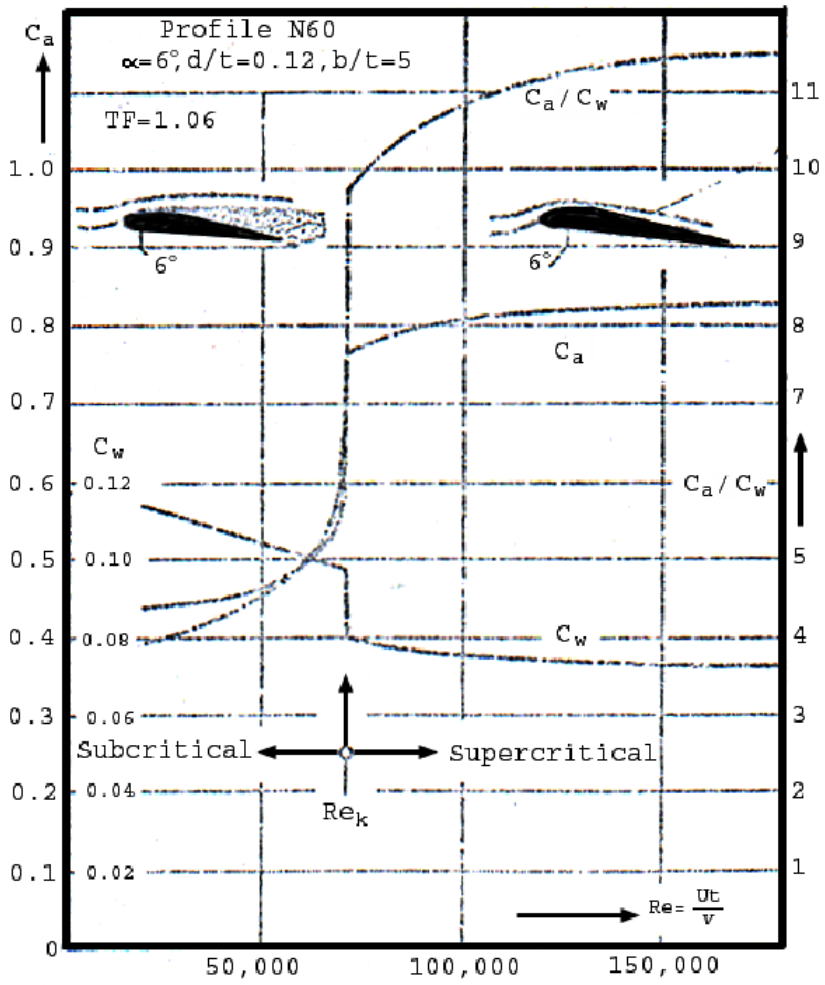

Figure 1.5: Effect of Reynolds number on N60 maximum lift and minimum drag (C_a is maximum C_l and C_w is minimum C_d; figure from Schmitz[21])

In the 1980's, interest in low Re aerodynamics was renewed by researchers such as Mueller, Selig, and Hoerner, whose studies[22] also agreed with those of Schmitz's experiments. Specifically, thin flat and cambered plates are more efficient than conventional airfoils below Re 4×10^4. Another observation was that cambered plates show less variation of lift coefficient (C_l) and drag coefficient (C_d) with Re while flat

plates remain virtually unchanged, which also evident in Figure 1.3. Hoerner showed that from Re = $4x10^4$ to Re = $1.2 x10^5$, cambered plate C_{lmax} rose by 4% whereas N60 C_{lmax} rose by over 180%.[22] Furthermmore, low Re experiments by Selig[23] and Mueller[24] on a range of airfoils also concluded that C_{lmax} will consistently increase with Re and that minimum C_d significantly decreases above Re 10^5. Another observation made by Selig was that for the 60 sailplane-type airfoils tested, the drag polar is visually similar and is more insensitive to Re variation once above Re 10^5. But below this Re, there is a large degree of non-linearity in the drag polar with Re variation[23]. The initial results from each of these studies indicated that low Re airfoil performance is very dependent on airfoil geometry and the specific Re at which they operate.

The specific airfoil characteristics, such as camber and thickness, significantly affect airfoil lift and drag. For example, Okamoto conducted wind tunnel experiments on flat plates of 1, 3, 5, and 10% thickness at Re = 10^4. His measurements showed that each time thickness was decreased, lift and drag characteristics improved, with the 1% flat plate being the most efficient[25]. Similarly, Okamoto also measured the effect of the amount of camber on the performance of thin plates. 1% thick plates with cambers of 3, 6, and 9% were tested at Re = 10^4. The measurements showed that as camber was increased, so too did lift by a significant margin. However, there was also increased drag as camber was increased. The drag polar revealed that moderate camber (6%) yields the highest lift-to-drag ratio[25].

Another peculiar observation made by Okamoto was the effect of leading edge shape on airfoil performance. 10% thick flat plates with rectangular, rounded, and sharp leading edges were tested at Re = 10^4. The rectangular leading edge performed the worst while the sharp leading edge exhibited the highest lift and lowest drag of the three airfoils[25]. Furthermore, Okamoto tested conventional Clark-Y type airfoils of varying thickness in forward and reversed flow. As shown in Figure 3, the airfoils in the reversed configuration effectively have the same maximum thickness as their counterparts, but with a sharp leading edge. The reversed airfoils exhibit higher peak lift and lower drag than their counterparts, particularly for the 9% and 12% thick

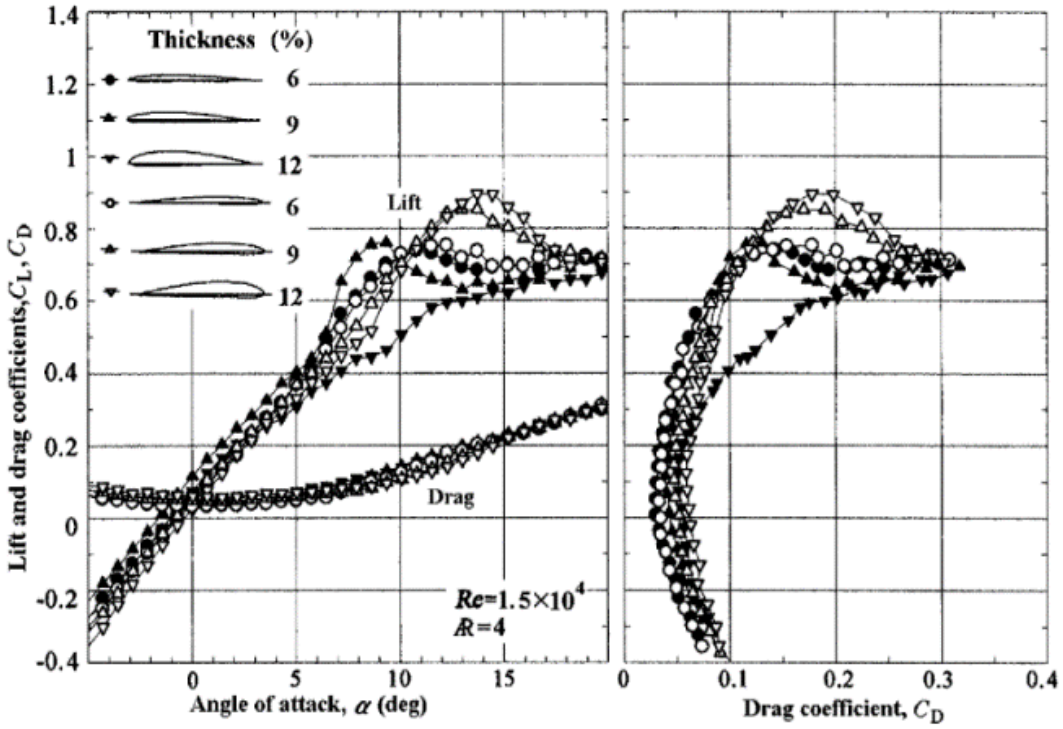

Figure 1.6: Effect of reversing Clark-Y type airfoils at Re = 10^4 (figure from Okamoto[25])

airfoils[25]. A similar effect was also observed in experiments by Laitone in which a conventional and reversed NACA 0012 were compared at Re = 20,700. At this Re, the reversed NACA 0012 was shown to yield improved lift-to-drag characteristics compared to its conventional configuration[26]. The results of these studies suggest that airfoil thickness distribution, particularly towards the leading edge, is an important factor in determining low Re performance, with sharper leading edges being more desirable.

While the experimental measurements of previous studies are useful for understanding some trends in low Re aerodynamics, they also have many limitations. Previous studies on Re < 10^5 typically contain lift and drag data only for a single Re[27] for each airfoil, which is not sufficient to fully characterize its performance across the Re spectrum. Furthermore, the data sets which are below 10^5 contain uncertainties and discrepancies. For instance, C_d measurements taken on the E387 airfoil (9.1% *t/c*, 3.2% camber) at Re 6×10^4 have been shown to vary by 28–68% between independent measurements, which have been taken at different facilities[28]. Whereas at Re 2×10^5, the drag measurements were much more consistent and vary by less than 13%[28]. These discrepancies are due to factors such as the drag measurement method used (wake-momentum deficit[29] or load measurement), inadequate force measurement sensitivity[26], and wind tunnel turbulence levels[30]. Additionally, below Re 10^5, even small changes in Re have a much more prominent effect on airfoil performance than they would at higher Re. It has been shown that for the NACA 0012 airfoil, the lift curve is highly non-linear[31], particularly for Re below 5×10^4. Additionally, C_l at Re 5×10^4 can be as

much as 3 times higher than C_l at Re 10^4 for a given angle of attack[31]. Since many of the airfoils tested below Re of 10^5 are only tested at one Re, there is not enough data to capture each airfoil's performance sensitivity to Re.

1.5 Computation Fluid Dynamics Development

One option for expanding the understanding of low Reynolds number airfoil characteristics is to perform a vast number of experiments to assess the performance of various airfoils over a wide range of angle of attack and different Re. However, these tests can be prohibitively expensive and time consuming making them practically infeasible. Therefore, the more favorable option is to utilize computational methods to approximate airfoil performance. Many computational tools and methods which have previously been used to calculate airfoil performance at high Re may not be applicable at Re less than 10^5 because of the nature of the flow. In this MAV Reynolds number regime, the viscous forces become quite significant and the second order viscous terms in the governing partial differential equations for fluid flow cannot be neglected[32]. Therefore, simplified theories, which neglect viscosity such as the inviscid Euler equations, thin airfoil theory, and thin boundary layer approximation cannot be applied at low Re[32]. Tools which use the vortex panel method, such as XFOIL, have been extensively used and validated for high Re flows[6]. However, XFOIL also does not correctly account for low Re viscous terms and has not been shown to satisfactorily predict airfoil performance below Re of 10^5.

Alternatively, computational fluid dynamics (CFD) has evolved significantly over the past few decades and has been routinely used by academia and industry to the point of accurately predicting both internal and external aerodynamic flows past complex geometries. Now, CFD codes, which numerically solve the Navier-Stokes equations, are being increasingly used to design and predict the performance of a wide range of single and multi-element airfoils at low Re. Therefore, an objective of the present research is to utilize a proven computational tool capable of generating reliable lift, drag, and moment data for an arbitrary 2D airfoil at any Re above 10^4 to extract the useful trends from the data to: 1) understand the behavior of airfoils at these low Reynolds number, and 2) provide insight and guidance for low Re rotor designs.

There are three primary types of CFD solvers 1) Direct Numerical Simulation (DNS), 2) Large Eddy Simulation (LES), and 3) Reynolds-Average Navier-Stokes (RANS)[33]. DNS solves the full, unsteady Navier-Stokes Equations without filtering or Reynolds-averaging operations in the domain of an extremely fine computation grid. LES instead solves the filtered Navier-Stokes equations for large scale eddies and accounts for energy at small scales with a sub-grid scale eddy viscosity model. Both of DNS and LES methods are high fidelity solvers, which can be useful for understanding the intricacies of low Re flow[33]. However, this accuracy comes at a computational cost since the equations being solved are more complex than RANS equations and these methods require a number of computational grid points on the order of 30 million to 500 million[33] (the present study uses a grid on the order of 30,000). Therefore, DNS

and LES would be prohibitive for expanding the amount of airfoil data at low Re. A faster approach is to utilize RANS equation solvers.

Two RANS-type solvers are the 2-Dimensional Incompressible Navier-Stokes solver (INS2d) and Fluent. INS2d was developed at NASA as an insect scale (Re < 10,000) CFD code. As such, it assumes fully laminar flow, which is known to be an invalid assumption for Re > 10,000 due to the evidence of laminar separation bubbles and turbulent boundary layers[33]. Furthermore, INS2d has been shown to yield poor agreement with exponential micro-rotor measurements when applied to a rotor analysis code[34,35]. Fluent is a popular commercial CFD code for 2-Dimensional incompressible implicit solutions. However, it was designed for use in more conventional Re regimes. Therefore, it has been shown in previous validation studies to be unable to model the complex viscous nature of the flow and the typical non-linearity of lift curves at low Re[6]. A more accurate RANS solver for low Re flows is required for the present study.

The CFD selected for this study is the *Transonic Unsteady Rotor Navier-Stokes* (TURNS2D) fluid dynamics solver developed at the University of Maryland, which is explained in detail in Section 2.1. Based on previous validation studies conducted by Benedict[36], Yang[37], and Medida[33], TURNS2D has provided good agreement with a variety of experimental airfoil measurements at MAV scales. By leveraging TURNS2D to compute trends in aerodynamic performance at low Re, appropriate airfoils can be selected for testing in micro-rotor design.

1.6 Micro-Rotor Design and Development

Much of the previous literature related to MRAVs has been focused on control authority and autonomous capability[5, 38, 39]. As such, the fundamental design and aerodynamic studies for MRAVs have been lacking. Previous attempts have been made by researchers, such as Hein and Chopra[40] and Ramasamy, Johnson, and Leishman[15], to investigate low Reynolds number micro-rotor aerodynamics. These works were focused on experimental parametric testing of various micro-rotors through load measurements and flow visualization. The Hein rotors had a radius of 76.2 mm and tip Re of approximately 40,000, and the Ramasamy rotors had a radius of 86 mm and tip Re of approximately 35,000. Results of these studies showed that rotors with moderately cambered (6.75%) plate airfoils yield high aerodynamic efficiencies and that sharpening the leading edge reduces viscous wake and profile losses[15]. It was also determined that blades with twist and chord-taper further improved performance somewhat, but the optimum amount was not quantified. The flowfield studies also indicated that micro-rotors have highly non-uniform inflow distributions and comparatively much larger tip vortices than full-scale rotors, resulting in lower performance. While these studies are useful for an initial understanding of low Reynolds number rotor effects, other parameters such as solidity and number of blades were not investigated and an optimum micro-rotor design was not sought after.

Bohorquez and Pines[6] developed an optimization method to design an efficient micro-rotor with a radius of 110 mm and tip Re of approximately 60,000. The method

utilized Blade Element Momentum Theory (BEMT) with CFD-generated tables (from INS2d) to optimize rotor efficiency based on blade camber, blade thickness, and chord-taper. The optimization study yielded a successful rotor with a figure of merit of 0.65, which was integrated into the coaxial MRAV design shown Figure 1.2(c). However, the design studies of the rest of the vehicle components, such as batteries and motors, were limited, resulting in a relatively poor vehicle endurance (10 minutes) to GTOW (155 g) [6].

Another study, conducted by Harrington[11], similarly focused on optimizing micro-rotor performance as well as motor-rotor coupling performance. The rotors in this study were designed for use on a quadrotor, and therefore had a smaller radius of 34 mm and nominal tip Re of 21,600 in hover. Harrington also concluded that micro-rotors with cambered plate airfoils, geometric twist, and chord-taper yield the highest performance. However, these studies did not include the effect of varying solidity by chord length or the advantages of stiffer blade materials like carbon fiber. Though extensive motor-rotor pairing tests were conducted, the maximum propulsion system efficiency that could be reached in hover was only 30%. Additionally, the quadrotor airframe was oversized, and amounted to nearly 20% of the GTOW. The final quadrotor design weighed 60 g but had a hover endurance of less than 10 minutes.

1.7 MRAV Design Algorithms

Given the recent emergence of quadrotor MRAVs, the guidelines for quadrotor design have been mostly ad-hoc and are not based on rigorous weight models as is the

case for full-scale rotorcraft. Limited attempts have been made by researchers to develop sizing methods for MRAVs. The ETH Zurich method utilizes an active database look-up function for components for each sizing iteration[41]. The National Technical University of Athens developed a parameterization method similar to present study. However, this method is limited since it primarily depends on only the physical lengths of each component[42]. More recently, Georgia Institute of Technology also developed a parameterization based method[43]. Unlike the present research, this method is limited to brushless motors and did not characterize brushed motors or speed controllers commonly used on smaller (<100 g, GTOW) quadrotors. Furthermore, a method for obtaining and validating edgewise flight performance characteristics, which is important for sizing quadrotors for different mission requirements, is not addressed. A popular online tool for MAV design is eCalc[44]. However this design program is based on manual user selection of specific vehicle components to estimate performance. Contrary to eCalc, the proposed methodology determines vehicle component requirements based on mission parameters such as endurance, flight speed, and payload capacity.

Conventional sizing methods for large-scale rotary-wing vehicles have been well described by Tishchenko, Boeing-Vertol, and Research and Technology Labs of the US Army Aviation R&D Command[45]. These methods are intended to be used for vehicles with fuel-based engines. As such, required fuel weight fraction is iteratively factored into the total vehicle weight based on required power and mission segments. However, small-scale rotary-wing MAVs are mostly electrically powered so

conventional sizing trends which encompass internal combustion engines and turbojet engines are not directly applicable. Furthermore, weight groups accounted for in conventional helicopter sizing include the main rotor hub and tail rotor, which are not present on a quadrotor. However, the general methodology used to derive sizing relations is applicable at MAV-scales. Specifically, multivariable linear regression is utilized by Research and Technology Labs to derive empirical sizing equations. This method has been shown to consistently yield accurate weight predictions for a range of large-scale helicopters[45]. Therefore, an objective of the present research is to derive a similar sizing methodology that is now applicable to small-scale multirotor vehicles.

1.8 Objectives

The focus of the present research is to develop accurate models for MRAV performance and to apply the models to improve MRAV capabilities and design processes. As such, there are four main objectives for the study:

1. Identify how low Reynolds number flows effect airfoil efficiency and profile power contribution.
2. Apply the insights gained from low Reynolds number sectional aerodynamics to micro-rotor design and improve rotor hover efficiency.
3. Integrate an optimal micro-rotor design into a high endurance quadrotor design to demonstrate improved aerodynamic and system level efficiency.

4. Identify key sizing relations in quadrotor systems and apply them in conjunction with low Reynolds number performance models to create a high-level conceptual MRAV design tool.

1.9 Summary of Chapters

This thesis describes the completion of the aforementioned objectives in the following chapters. In Chapter 2, the computational solver (TURNS2D) used in this airfoil study will be introduced and validation at low Re will be shown. The effects of low Re flows between $10^4 – 10^6$ for various airfoils will be discussed. In particular, the effect of airfoil characteristics, such as thickness, camber, and leading edge shape, will be described and airfoil performance sensitivity to changing Re will be assessed.

Chapter 3 describes the design and fabrication of a highly efficient micro-rotor. In addition to the effect of rotor blade airfoil, the effects of solidity, number of blades, chord taper, and blade twist of rotor performance will also be discussed. The systematic, experimental testing process used to evaluate micro-rotor performance is detailed. The micro-rotor fabrication methods are also presented in Chapter 3. Finally, the characteristics of the optimal hovering micro-rotor are summarized.

Chapter 4 discusses the design and flight testing of a high endurance quadrotor prototype. The performance results of coupling the optimal rotor described in Chapter 3 with various motors and gear ratios are the primary focus of Chapter 4. The design of the other quadrotor components, such as the battery, airframe, and avionics are also discussed. Lastly, the results of gimbal-stand and free-hover flight tests are presented.

Chapter 5 describes the development of a sizing design tool for MRAVs. First, the major quadrotor components and the parameters which drive their weights are described. The empirical equations derived from statistically regression analysis which relate quadrotor performance to component weights are provided. The methods to calculate quadrotor performance parameters, such as thrust and power, are discussed and validated. Finally, the results of the complete sizing code predictions compared to existing quadrotors is presented. Chapter 6 summarizes the conclusions of the current research and possible areas of future work.

1.10 Contributions of the Present Research

The overall scope of this work provides improvements and better understanding in the field of MRAV design and development. The work in CFD simulation established the required parameters to model low Reynolds number flows and validated the accuracy of TURNS2D for a range of Reynolds numbers. It also resulted in the generation of an expansive database of airfoil lift, drag, moment, and pressure data at low Re which would have otherwise been costly and time consuming to obtain experimentally. In addition to MRAV design, this database can be used in any application which requires low Re sectional performance values.

The systematic, experimental testing and evaluation of micro-rotors determined the key characteristics which improve low Re rotor efficiency. The optimal rotor designed based on the understanding gained from the present study produced a figure of merit (*FM*) of 0.66, which is the highest value of *FM* reported in the literature for

micro-rotors operating at tip Re less than 70,000. Furthermore, the measurements from the large number of fixed pitch rotors (over 500) serves as an experimental database of performance quantities which can be used for validation of other low Re performance simulations.

The experimental studies in coupled rotor, gear, and motor systems determined the most efficient electric propulsion system for sub-50 gram quadrotors. A high endurance quadrotor weighing 45 grams was designed utilizing this electric propulsion system and flight tested. Presently, the longest continuous hover endurance achieved with this design is 31 minutes, which is perhaps longer than any other multirotor at this weight scale.

A sizing code which encompasses the insights gained from the previous studies has been developed for MRAVs. Given the relatively recent wide-spread use of MRAVs, such design codes are now being developed. The data compiled on the quadrotor components and the derived sizing equations will provide concrete design methods for MRAV designers.

Chapter 2: Computational Fluid Dynamics Studies

2.1 Computational Method

The CFD solver used in this study to investigate 2D low Re aerodynamics is *Transonic Unsteady Rotor Navier-Stokes 2D* (TURNS2D)[46] fluid dynamics solver developed at the University of Maryland. TURNS2D has been widely used in the past for flows past airfoil and rotor blades at high-Reynolds number with confidence[46,37]. TURNS2D uses a dual volume formulation to solve for the Reynolds-Averaged Navier-Stokes (RANS) equations. The inviscid fluxes uses a third-order MUSCL reconstruction scheme in conjunction with Roe's scheme, while the viscous fluxes are computed using a second-order central difference. For steady problems, an Euler implicit formulation was used for time marching with the matrix inversion performed using a lower-upper symmetric line-Gauss-Seidel approach. A key feature in TURNS2D is the inclusion of a laminar-turbulent transition model coupled with the Spalart-Allmaras (SA) turbulence model, which improves the numerical solution by better predicting the flow transition physics[47]. The formulation keeps track of the "intermittency" in the flow, whose value varies between 0 and 1, indicating a fully attached or fully separated flow, respectively. C-meshes were generated around the airfoil of interest and the RANS equations were solved using TURNS2D to generate sectional coefficients of surface pressure (C_p), skin friction (C_f), lift (C_l), drag (C_d), and pitching moment (C_m) for an airfoil under given flow conditions[46].

To generate the following CFD results, a C-mesh was used as the grid type around the airfoil with an outer boundary at 15 chord lengths away from the airfoil surface. A mesh size with 267 grid points in the surface-wrap direction and 123 grid points in the surface-normal direction. Grid spacing within the boundary layer in the normal direction was 0.001% of the chord length. Dual time stepping was implemented with a time step size of 0.1. The freestream Mach number was fixed at 0.1 because the majority of studies did not report an exact Mach number, and the flows were assumed to be within the incompressible range. These parameters were found to be sufficient for solution convergence at the range of low Re investigated. Using these parameters, the solution for a single airfoil at a single Re over a range of ten angles of attack takes approximately nine hours to converge on a typical desktop computer.

2.2 Results and Discussion

To demonstrate the capability of TURNS2D, validation cases were carried out by comparing previous experimental results to the current computational results. The primary validation data used was existing C_l and C_d data versus angle of attack (α). C_p along the chord was also used to validate the TURNS2D results with available test data. Because the NACA 0009 experiment by Lutz, Würz, and Wagner[48] reported both C_l and C_d data as well as C_p data for low Re flows, it was selected as an early validation case. The upper surface pressure coefficient validation for the NACA 0009 airfoil at multiple angles of attack is shown in Figure 2.1(a) ($Re = 5 \times 10^4$). It is evident that at low angles of attack ($\alpha \leq 5^o$), the C_p results from TURNS2D agrees very well with the

experimental data[48]. At higher angles of attack, shown in Figure 2.1(b), the agreement is less satisfactory but still follows the trend as angle of attack increases. Figure 2.2 shows the lift and drag comparison for the same NACA 0009 airfoil at Re = 5 x10^4. It can be seen that for the majority of the lift and drag curves, the C_l and C_d calculated by TURNS2D compare very well until close to stall due to large separated flow regions, which is a limitation of the S-A turbulence model[33]. The SA turbulence model within RANS is known to overpredict the Eddy viscosity, which tends to lead to high-rates of dissipation in the flow. To better predict the onset of stall and the immediate post-stall characteristics, either a Large Eddy Simulation or a Detached Eddy Simulation may be required, which is beyond the scope of the present study.

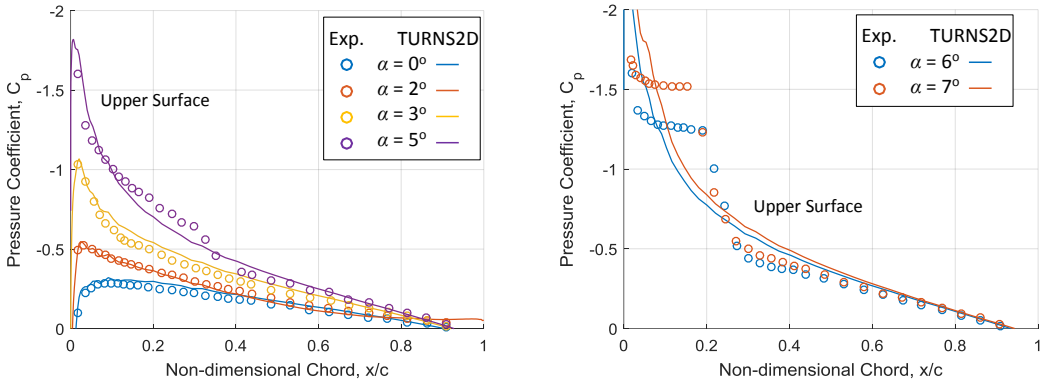

(a) NACA0009: Low angle of attack (b) NACA0009: High angle of attack

Figure 2.1: C_p over the upper surface of a NACA0009 airfoil for various angles of attack at Re = 5x10^4 (Experimental data from Lutz, et al.[48])

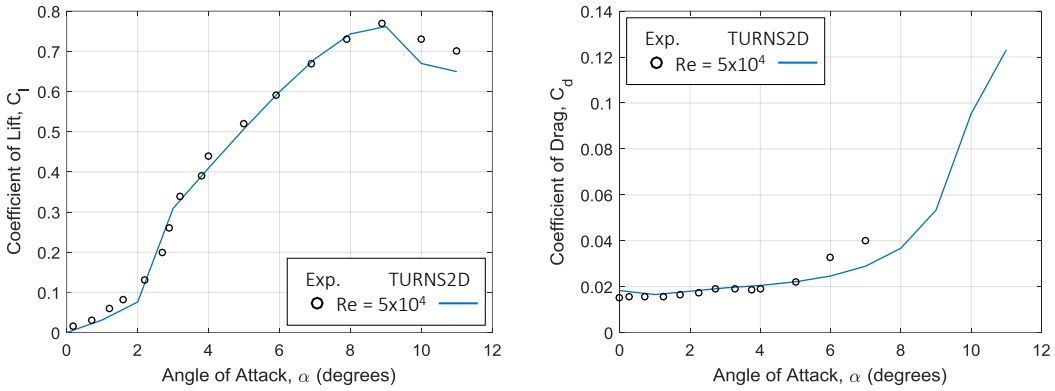

Figure 2.2: C_l and C_d comparison of TURNS2D CFD predictions with experiment for NACA0009 at Re = 5 x10^4 (Experimental data from Lutz, et al. [48])

2.2.1 Effect of Re on NACA 0012

The NACA 0012 is a common airfoil which has been experimentally tested for a wide range of Re. Therefore, the experimental results serve as a useful validation database for both high and low Re. The wide range of Re also provides insight into how strongly Re effects airfoil performance.

Figure 2.3 shows the validation of C_l and C_d predictions from TURNS2D with the experimental measurements taken at Sandia National Laboratories[49] for the NACA 0012 at moderate Re (3x10^5 to 1.8x10^6). The lift and drag correlate well for both Re = 3x10^5 and Re = 10^6 for the range of α shown, including the angles around stall. Already, a 23% drop in peak C_l from Re = 10^6 to Re = 3x10^5 is observed. The drag also rises sharply at a smaller α as Re is decreased. However, the lift curve slope and minimum drag appear to be very similar.

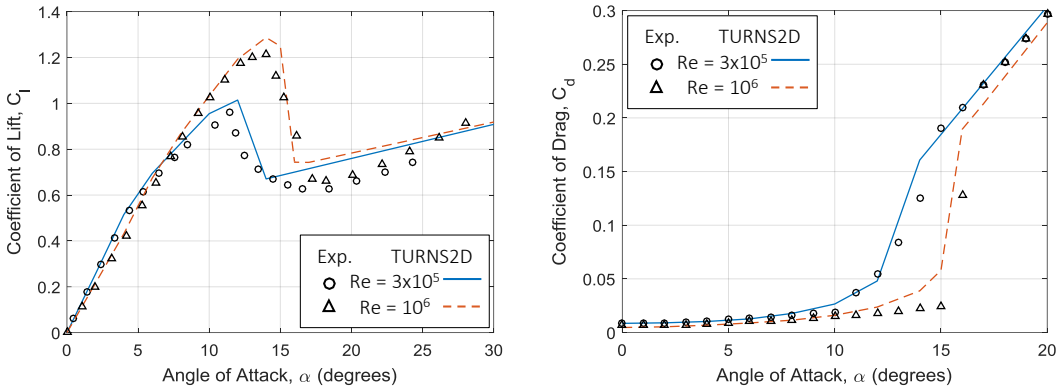

Figure 2.3: High Re C_l and C_d comparison of TURNS2D CFD predictions for NACA0012 at Re = 3x10^5 and 1x10^6 (Experimental data from Sheldahl and Klimas[49])

The C_l, C_d, and C_m comparisons for a NACA 0012 airfoil at various low Re between 10^4 and 10^5, is shown in Figure 2.4. The results show the extreme sensitivity of airfoil performance to changing Re below 10^5 for the NACA 0012. As Re decreases, there is an increase in drag, particularly due to shrinking of the drag bucket, and a large decrease in lift. Here it is shown that peak C_l decreases by approximately 46% between Re = 10^5 and Re = 10^4. Unlike the higher Re results in Figure 2.3, the lift curves are highly non-linear, particularly for $\alpha < 5^o$, and a single lift-curve-slope value cannot be assumed. It should also be noted that the drag bucket is significantly smaller at low Re and the minimum drag noticeably increases compared to the minimum drag in Figure 2.3. The general shapes of the moment curves are shown to vary significantly as Re changes, but these are still predicted moderately well.

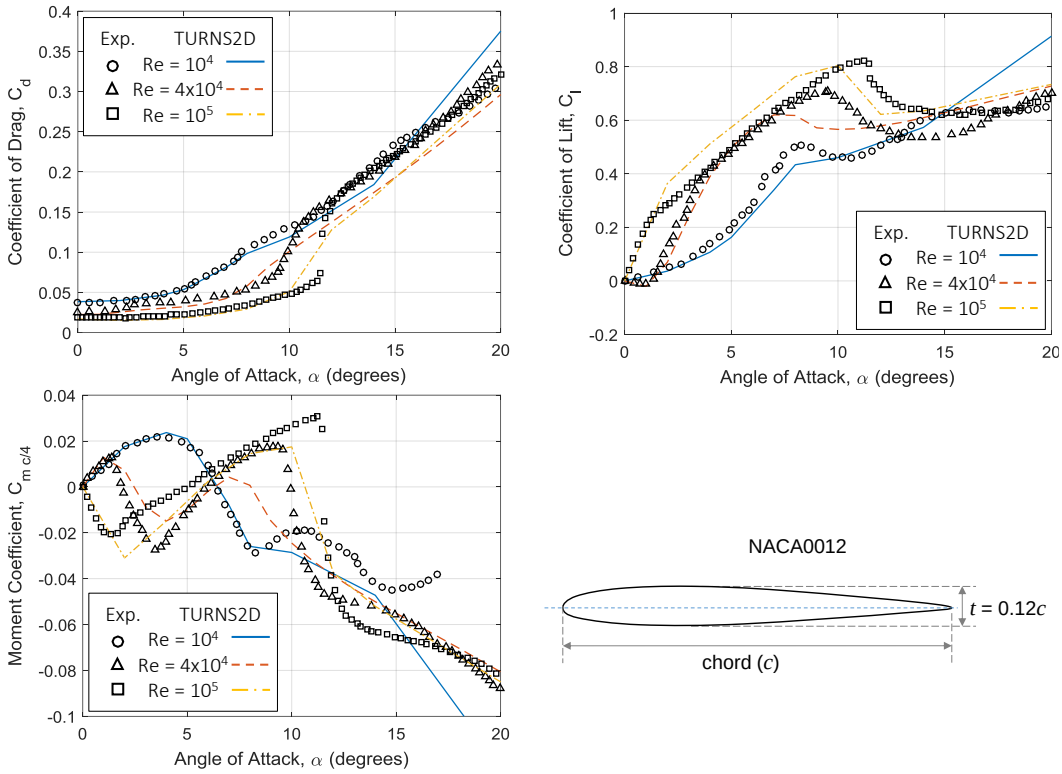

Figure 2.4: C_l, C_d, and C_m comparison of TURNS2D CFD predictions for NACA0012 at 10^4 < Re < 10^5 (Experimental data from Ohtake, et al.[31])

2.2.2 Effect of Thickness on Flat Plates

The specific airfoil parameters, such as camber and thickness, heavily affect airfoil lift and drag characteristics. For example, the effect of thickness (1, 3, and 5%) for simple flat plates at Re of 10^4 is shown in Figure 2.5. Results are shown from both TURNS2D and experimental measurements[25]. It is evident that as flat plate thickness-to-chord (t/c) decreases, lift and drag characteristics improved, with the 1% flat plate being the most efficient. For each flat plate, the lift-curve slope is generally constant up to approximately α < 7º, where the slope then abruptly drops for α > 7º. However,

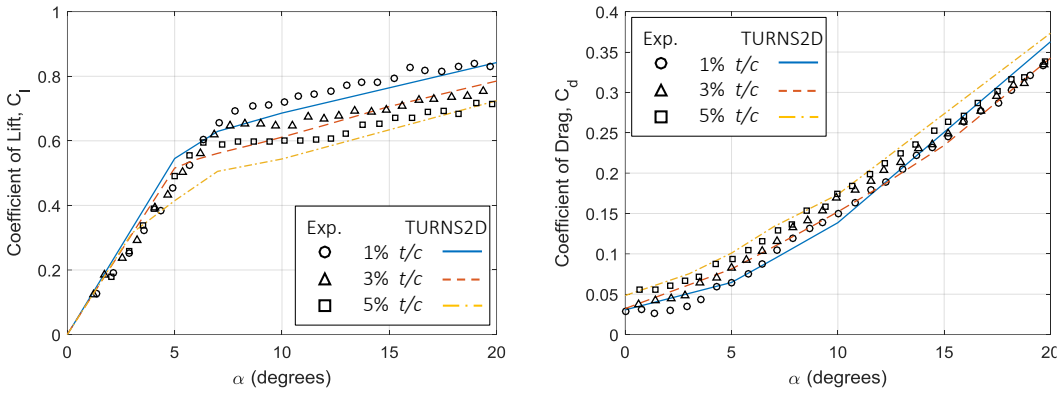

Figure 2.5: Effect of flat plate thickness on C_l and C_d at Re = 10^4 (Experimental data from Okamoto, et al.[25])

the high lift-curve slope is maintained to higher α as t/c is decreased. Flat plate C_d also decreases as t/c decreases. C_d appears to decrease with t/c between $0^o < \alpha < 10^o$, then converges to similar values at high α. Minimum t/c is shown to be a key characteristic for increased aerodynamic efficiency at low Re.

An explanation for the decreased performance as flat plate t/c increases is the increased separation of the flow around the airfoil. The thicker the flat plate is, the blunter its leading edge becomes. The increased bluntness of the airfoil leading edge increases the strength of the adverse pressure gradient. Thus, the flow around the airfoil is separated by a greater distance, which increases form drag. Furthermore, the increased separation of thicker flat plates reduces the pressure differential between the upper and lower surfaces, thus reducing its lifting force.

2.2.3 Effect of Camber on Thin Plates

In order to understand the performance trends at Low Re due to camber, thin plates with varying camber were investigated. C_l and C_d for 1% thick plates with cambers of 3, 6, and 9% at Re = 10^4 are shown in Figure 2.6. Results are shown from TURNS2D with experimental measurements[25] overlaid. The results show that as camber is increased, so does the lift curve and peak lift by a significant margin. However, there is also increased drag as camber is increased, particularly for 9%

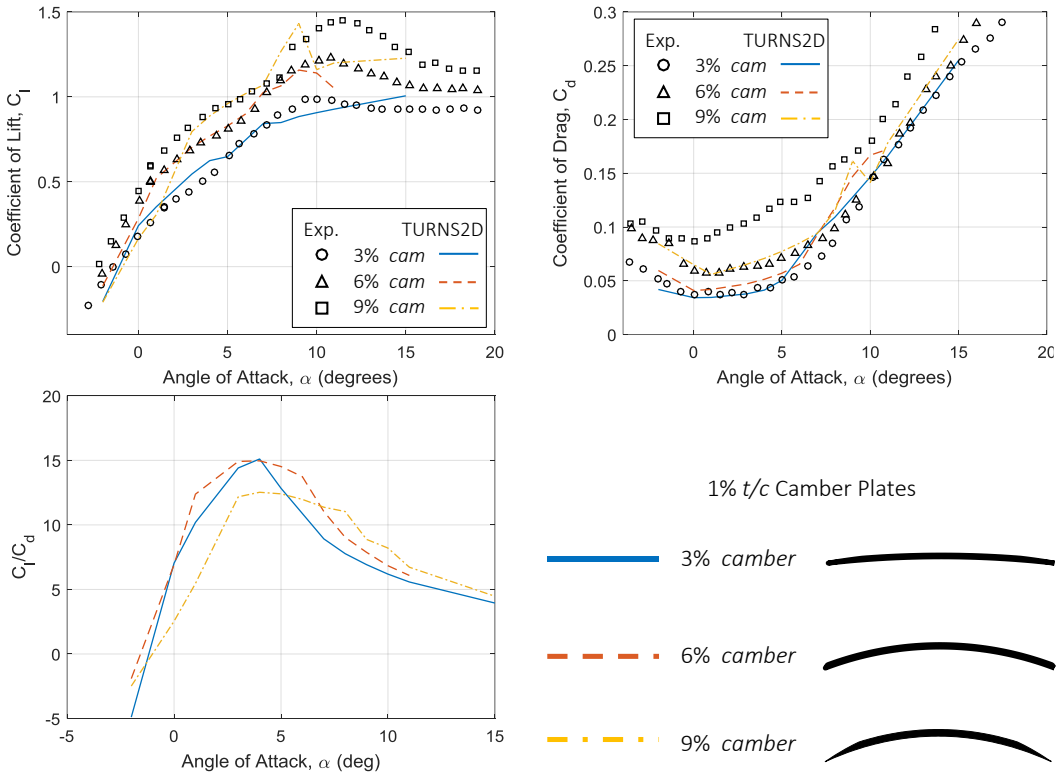

Figure 2.6: Effect of thin plate (t/c = 1%) camber on C_l, C_d, and C_l/C_d at Re = 10^4 (Experimental data from Okamoto, et al.[25])

camber. Figure 2.6 also shows the lift-to-drag ratio of each cambered plate. It is evident that despite the higher C_l of the 9% camber, a moderate camber (6%) yields the highest lift-to-drag. Clearly, camber has a strong effect on low Re aerodynamic performance.

The effect of increasing airfoil camber causes a greater change in momentum of the flow around the airfoil, thus increasing lift. However, the trade-off is that increasing thin plate camber also increases drag. When the camber is too great, a large separation region is created on the aft end the airfoil. This separation region effectively increases the profile size of the thin plate, which increases drag. At low Re, the camber value at which the drag increases begin to outweigh the lift gains appears to be larger than 6%. For a low Re wing design to achieve high lift, approximately 9% camber may be needed. Whereas, 6% camber should be utilized if efficiency is a desired design factor.

2.2.4 Effect of Re on Thin Cambered Airfoils

The effect of camber on thin (3% *t/c*) NACA airfoils was examined with the use of computational results from TURNS2D. The performance results for symmetric (NACA0003), 2% (NACA2403), 4% (NACA4403), and 6% (NACA6403) cambered airfoils are shown in Figure 2.7. Results are shown for two flows, Re = $2x10^4$ and Re = 10^5.

At both Re = $2x10^4$ and Re = 10^5, increasing camber increases the C_l over the given range of angle of attack. However the increase in camber also causes a drag penalty by increasing the minimum drag. As a result, the lift-to-drag curves of the

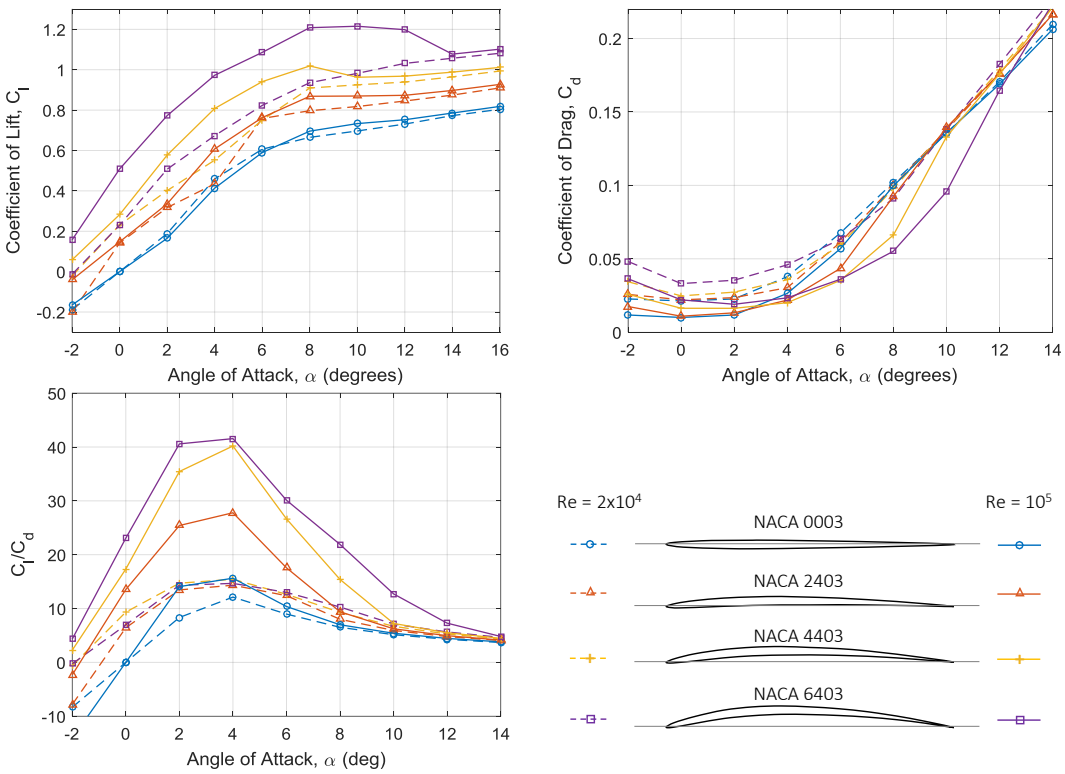

Figure 2.7: Effect of camber on C_l, C_d, and C_l/C_d for NACA Airfoils of 3% *t/c* at Re = 2x10^4 and 10^5

cambered airfoils are similar to each other at Re = 2x10^4, but they are slightly higher compared to the symmetric airfoil's lift-to-drag. At Re = 10^5, increasing camber has a more pronounced effect on performance. It is seen in Figure 2.7 that increasing Re increases C_l by a larger amount for higher camber airfoils. Additionally, C_d decreases more as Re increases for higher camber airfoils, particularly within 4º < α < 12º. As a result the lift-to-drag curves at Re = 10^5 are more differentiated than at Re = 2x10^4. The symmetric airfoil performance changes very little due to the increase in Re. As camber

is increased, the lift-to-drag improves by a greater margin. This result indicates that the degree to which an airfoil's design parameters effect its performance is also dependent on Re.

2.2.5 Flat Plate and NACA 0012

It was seen in Figure 1.3 that simple flat plates can outperform conventional airfoils for Re < $5\text{x}10^4$. To obtain a deeper understanding of this rationale as to why certain airfoil design parameters are better suited to low Re flows than others, the flow field solution from TURNS2D are examined. For example, the comparisons between the NACA 0012 airfoil and a 2% *t/c* flat plate at Re = $2\text{x}10^4$ are shown in Figure 2.8.

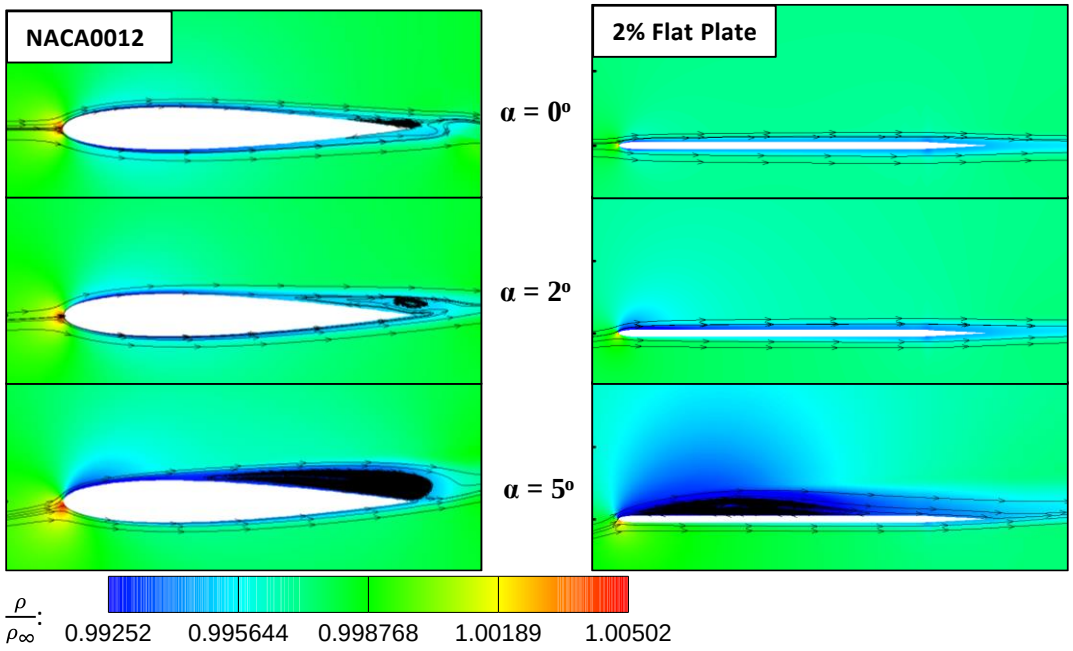

Figure 2.8: Difference in boundary layer characteristics between NACA 0012 and 2% *t/c* flat plate at Re = $2\text{x}10^4$ (contours represent non-dimensional density)

The key, distinguishing factor between the thick NACA 0012 and thinner flat plate is the difference in boundary layer separation. For the NACA 0012, the upper surface boundary layer stays attached for a majority of the airfoil until it separates close to the trailing edge. This separation characteristic is similar to flow-field results from previous studies[19,20] on thick, conventional airfoils at $Re < 5x10^4$. For the range of α shown, the flow separates too close to the trailing edge to gain momentum from the free-stream and reattach as a turbulent boundary layer. The resulting large separation region causes high form drag and prevents formation of the beneficial drag bucket around low angles of attack.

The large trailing edge separation results in low lift due to increased pressure on the upper surface. This low Re separation effect is particularly influential on the C_l curve for $0^o < \alpha < 3^o$ at $Re < 5x10^4$. In this range of angle of attack, the separation region can be large enough that the upper surface C_p actually becomes higher than the lower surface pressure C_p for most of the chord. This effect is evident in Figure 2.9 at $\alpha = 2^o$ where the upper and lower surface C_p curves for the NACA 0012 cross at 30% chord. At $Re < 5x10^4$, this pressure difference causes the lift curve slope close to $\alpha = 0^o$ to be less steep at other angles. It can even cause slightly negative C_l values as seen in Figure 2.4 for $Re = 4x10^4$.

The 2% *t/c* flat plate airfoil exhibits significantly different flow characteristics than the NACA 0012 in the same flow regime. As seen in Figure 2.8, the flat plate does not undergo trailing edge separation. Instead, the laminar flow is tripped early by the sharp leading edge. The separated laminar shear layer gains momentum from the free-

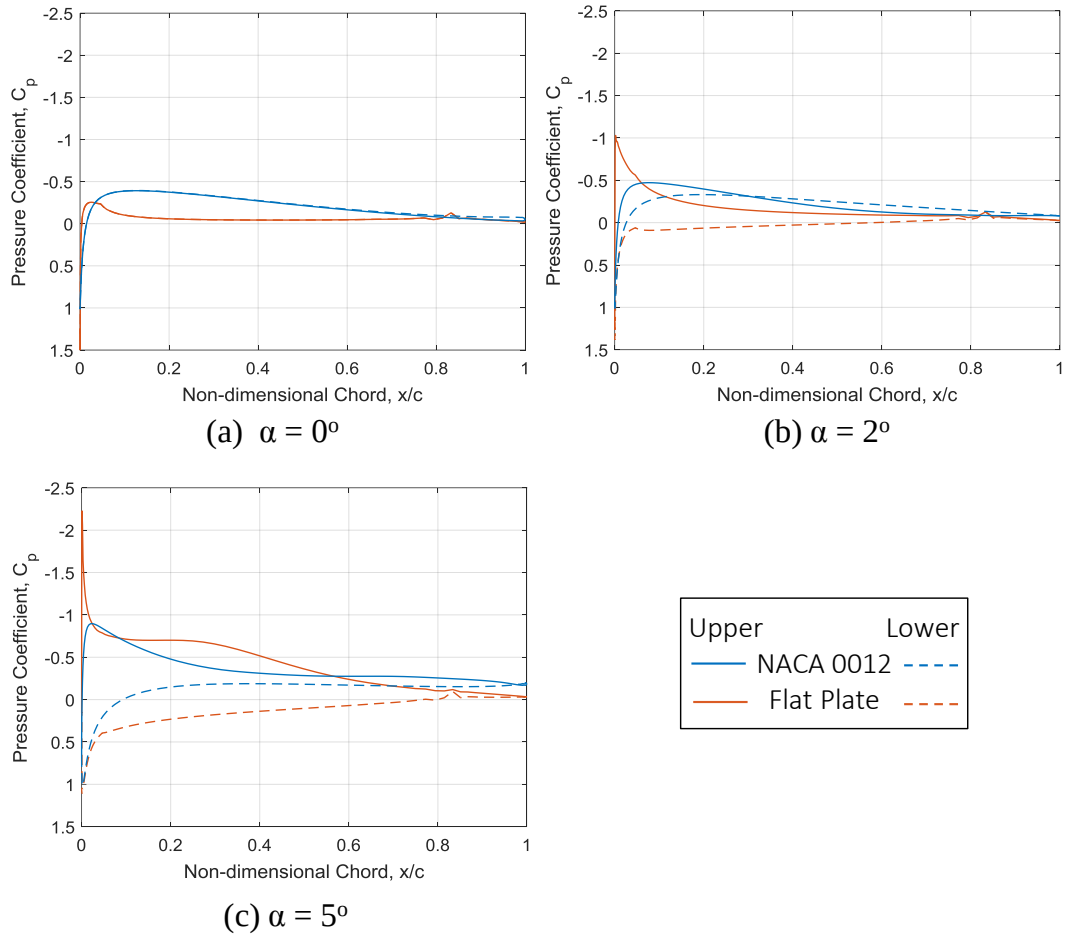

Figure 2.9: Pressure distribution on upper and lower surfaces of a NACA 0012 and 2% *t/c* flat plate at Re = 2x10^4

stream and transitions to turbulent. Since this transition occurs near the leading edge. There is enough chord length remaining for the turbulent boundary layer to reattach, forming a separation bubble. This bubble is most visible at α = 5° in Figure 2.8 for the flat plate. The C_p distribution over the upper surface of the flat plate in Figure 2.9(c) also indicates the presence of the laminar separation bubble. At α = 5°, there is a flattening of the thin flat plate upper C_p, which is typical of a separation bubble. The

reattachment of the upper boundary layer preserves the lower pressure and therefore allow the flat plate to provide more lift than the NACA 0012 at Re < $5x10^4$.

2.2.6 Conventional and Reversed NACA 0012

The effect of reversing airfoils at low Re may actually be beneficial depending on the airfoil. In addition to the maximum thickness of the airfoil, its leading edge (LE) geometry, sharp or rounded, has a strong effect on its performance. By reversing a symmetric airfoil, the LE geometry is essentially changed, but the maximum thickness remains the same.

Figure 2.10 shows the characteristics of a NACA 0012 in its conventional configuration (rounded LE) compared to its reversed configuration. In Figure 2.10(a), both the experimental data[26,31] and TURNS2D predictions show that the reversed configuration yields increased lift at Re = $2x10^4$. In particular, there is a very strong

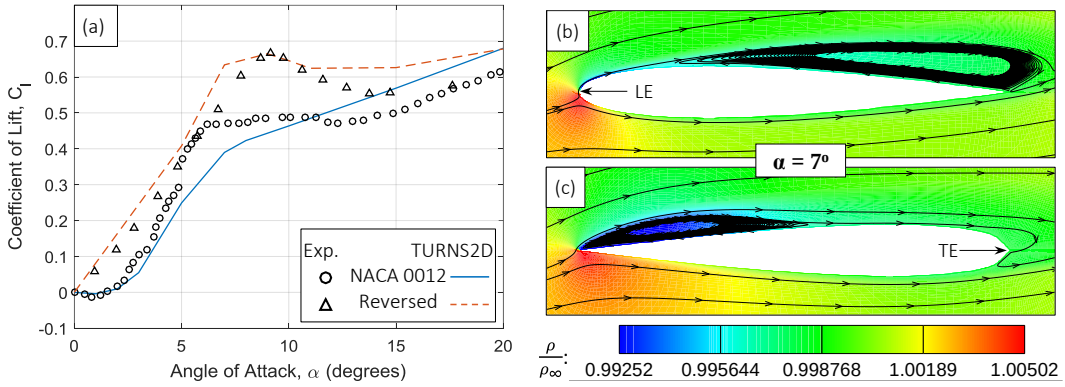

Figure 2.10: Characteristics of a NACA 0012 airfoil in conventional and reversed configurations at Re = $2x10^4$ (contours represent non-dimensional density; experimental data from Laitone[26] and Ohtake[31])

effect on peak lift between α = 7º–10º. The computational flow fields around the NACA 0012 at α = 7º provides insight into the difference in lift values. Figure 2.10(b) shows how the NACA 0012 in its conventional configuration creates a large separation region over 80% of the upper surface. However, when the NACA 0012 is reversed in the same flow conditions, it behaves more like a flat plate. Most notably in Figure 2.10(c), the sharp leading edge creates a similar separation bubble as seen on the 2% *t/c* flat plate in Figure 2.8. The early separation of the boundary layer on the reversed NACA 0012 allows it reattach as a turbulent boundary layer further downstream. The flow reattachment maintains lower pressure on the upper surface and increases lift. Despite the fact that the NACA 0012 has the same maximum thickness in either configuration, these results indicate the distribution of the thickness along the chord, particularly at the LE, has an effect on airfoil performance at low Re that is counter to what is expected at high Re.

2.2.7 Overall Re Effects

TURNS2D has been used as to determine other trends in aerodynamic performance of airfoils at low Re. For example, Figure 2.11 shows the effect Re of multiple types of airfoils: 2% *t/c* symmetric flat plate, 6% cambered plate (2% *t/c*), NACA 0012, and Clark-Y. This comparison was conducted to obtain an understanding of Re effects on vastly different airfoils. The major distinguishing factor between the airfoils is that the more conventional NACA 0012 and Clark-Y are much more sensitive to Re than plate-type airfoils. As seen in Figure 2.11, the peak C_l of the 6% cambered

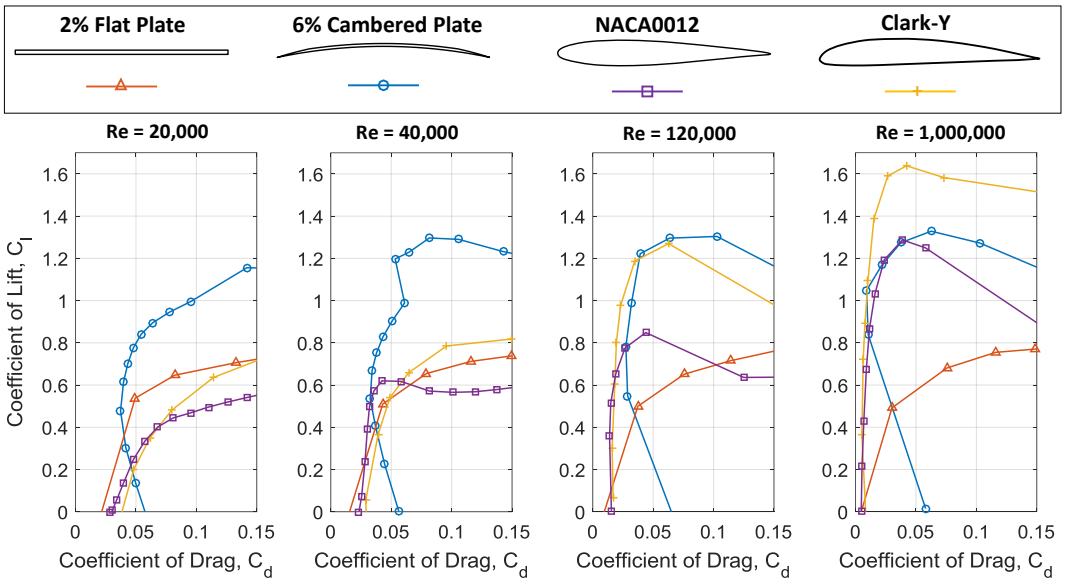

Figure 2.11: Effect of Reynolds number on multiple airfoils in terms of C_l vs C_d

plate only increases from approximately 1.15 at Re = $2x10^4$ to approximately 1.32 at Re = 10^6, and the peak C_l of the flat plat is virtually unchanged. Over the same Re range, the peak C_l more than doubles for the NACA 0012 and Clark-Y, increasing from 0.55 to 1.3 for the NACA 0012 and from 0.72 to 1.63 for the Clark-Y.

In Figure 2.11, the largest change in performance between the four airfoils occurs after Re = 10^5. At Re = $2x10^4$ and $4x10^4$, the thin flat and cambered plates clearly outperform the conventional airfoils in terms of lift and drag. But at Re = $1.2x10^5$, the C_l of the Clark-Y is comparable to that of the 6% cambered plate and the C_l of the NACA 0012 is primarily greater than that of the flat plate for a given C_d. These performance margins increase further at a higher Re of 10^6.

It should also be noted that Re appears to have a uniform effect on the C_d of each of the four airfoils. Figure 2.11 shows that as the Re increases, the C_l vs C_d curves gradually shift to the left, indicating decreasing drag. The minimum C_d appears to decrease by approximately the same amount for all four airfoils. Because the geometric characteristics of the four airfoils are vastly different, the similar decrease in their minimum C_d, is likely attributed to decreasing viscous drag effects as Re increases.

Figure 2.12 shows the effect of Re on each airfoil (2% *t/c* flat plate, 6% cambered plate, NACA 0012, and Clark-Y) separately in terms of lift-to-drag (C_l/C_d)

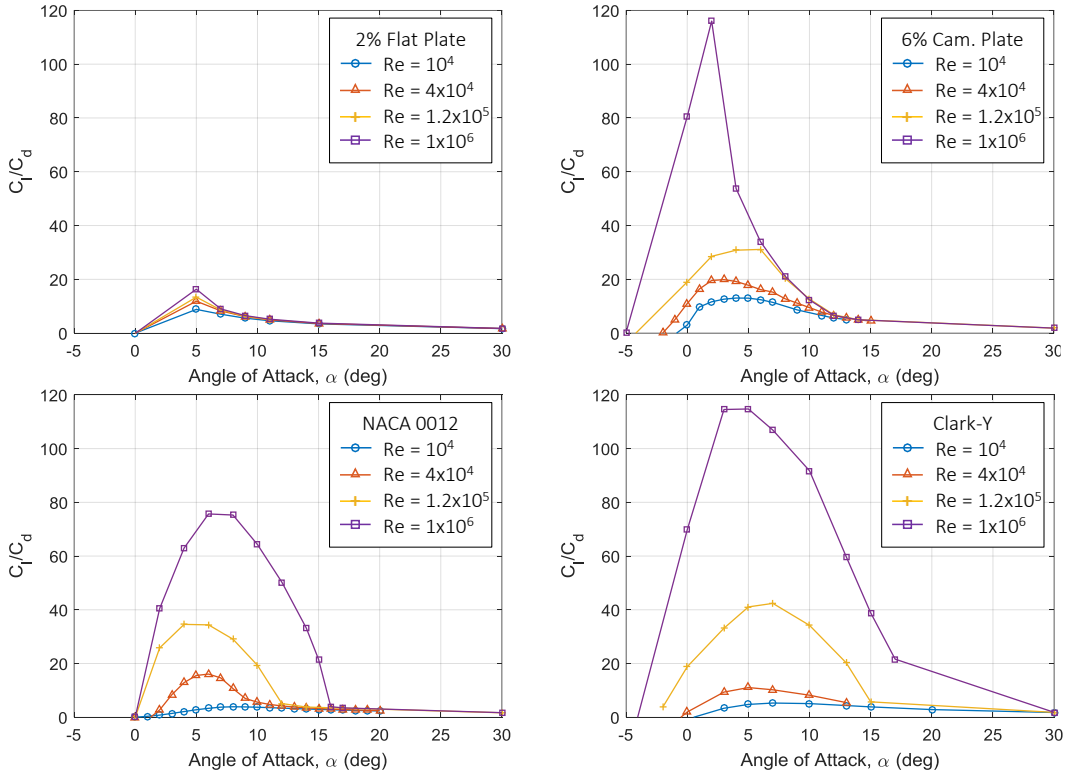

Figure 2.12: Effect of Reynolds number on multiple airfoils in terms of lift-to-drag vs angle of attack

as a function of α. Similarly to the results observed in Figure 2.11, the conventional airfoils' (NACA 0012 and Clark-Y) performance is shown to be more sensitive to Re compared to the plate-type airfoils. Surprisingly, the 6% cambered plate appears to achieve the same peak lift-to-drag as the Clark-Y at Re = 10^6, as seen in Figure 2.12. However, the Clark-Y maintains a larger envelope of higher C_l/C_d for $\alpha > 5^o$.

The primary implications for design drawn from these results are: 1) Below Re = 10^5, cambered plate airfoils will have better lift-to-drag characteristics than conventional airfoils 2) Above Re = 10^5, thicker airfoils will have better lift to drag characteristics than thin flat or cambered plates 3) Below Re = 10^6, lift to drag characteristics for most airfoils cannot be assumed to be constant with Re and 4) Flat plate performance is generally invariant to Re.

2.3 CFD Conclusions

The goal of the preceding chapter was to utilize TURNS2D as a means to understand low Re aerodynamics and provide guidelines for MAV and low Re designs. The results from TURNS2D are compared with available experimental C_l, C_d, C_m, and C_p data, as means of validation. Overall, the calculated values from TURNS2D agree quite well with the experimental measurements at low Re. The C_l, C_d, and C_p curves for the NACA 0009 at Re = $5x10^4$ correlate very well for low to moderate α. The calculated and experimental C_l, C_d, and C_m curves for the NACA 0012 at various Re between 10^4-10^6 are in good agreement. TURNS2D also predicts the performance trends of increasing airfoil camber and thickness at Re = 10^4 quite well.

The results from TURNS2D show the extreme sensitivity of airfoil performance to changing Re below 10^5, particularly for conventional airfoils like the NACA 0012. As Re decreases there is an increase in drag, particularly due to the shrinking of the drag bucket, and a large decrease in lift. C_{lmax} decreases by approximately 46% between Re = 10^5 and Re = 10^4. Unlike performance results above Re = 10^5, the lift curves are highly non-linear, particularly for $\alpha < 5^o$, and a single lift-curve-slope value may not be appropriate. It should also be noted that the drag bucket is significantly smaller at Re < 10^5 and the minimum drag noticeably increases.

The effect of thickness (1, 3, and 5%) for simple flat plates was examined at Re = 10^4. It is evident that as flat plate thickness-to-chord (t/c) decreases, lift and drag characteristics improved, with the 1% flat plate being the most efficient.

The effect of camber (3, 6, and 9%) on thin plate airfoils was examined at Re = 10^4. As camber is increased, both the C_l and C_d increase and the lift-to-drag is significantly improved compared to flat plate airfoils of the same thickness. For a low Re wing design to achieve high lift-to-drag, approximately 6% camber appeared optimum. On the other hand, 9% camber could be utilized if maximum lift is a stronger design factor.

The effect of camber on thin NACA airfoils (NACA 0003, 2403, 4403, 6403) was also examined at Re = $2x10^4$ and Re = 10^5. The high camber airfoils (NACA 4403 and 6403) were shown to have the highest lift-to-drag at both Re. Additionally, the lift-to-drag curves are more similar at Re = $2x10^4$ and more differentiated at Re = 10^5.The

symmetric NACA 0003 airfoil performance changes very little with an increase in Re. As camber is increased, the lift-to-drag improves by a greater margin. This result indicates that the degree to which an airfoil's characteristics effect its performance is also dependent on Re.

Examination of the boundary layer at low Re shows significant differences between thin plate airfoils and thicker airfoils. The NACA 0012 is more susceptible to trailing edge separation at low Re whereas the flat plate trips the laminar boundary layer at the leading edge, allowing it to reattach. The reattachment of the upper boundary layer preserves lower surface pressure and therefore allow the flat plate to provide more lift than the NACA 0012 at $Re < 5x10^4$.

When the NACA 0012 is placed in a reversed configuration at $Re = 2x10^4$, its lift qualities improve. This effect is due to the sharp leading edge creating an early laminar separation bubble similar to the flat plate's. Despite the fact that the NACA 0012 has the same maximum thickness in either configuration, this result indicates that the distribution of the thickness along the chord, particularly at the LE, has an effect on airfoil performance at low Re that is counter to what is expected at high Re.

Chapter 3: Micro-Rotor Design

3.1 Overview

The purpose of this chapter is to present the method used determine the qualities of an MAV-scale rotor which maximize flight endurance, thereby effectively increasing micro rotary-wing air vehicle (MRAV) practicality and mission capability. The insights gained from Chapter 2 were used as a starting point for rotor blade airfoil selection. Other rotor parameters considered include fabrication material, blade pitch, solidity, number of blades, geometric twist, and chord taper. The optimal qualities in each category were determined through comprehensive, systematic, parametric testing of physical rotors.

3.2 Rotor Material and Fabrication

In order to investigate a large variety of rotor parameters in sufficient detail, a considerable number of experimental tests were required. A high degree of precision between the incremental variations of a rotor was desired to ensure an accurate range of performance data was collected. This dictated that a unique rotor be fabricated for incremental variation of each parameter. A quick and cost-effective fabrication method was needed to promptly generate a large number of unique rotors. Typically, rotors at this scale are manufactured with plastic injection molding as a single piece. However, this technique is more useful for mass production of a single design since the molds can be reused. For the purpose of this research, injection molding was deemed

infeasible because it would incur too much cost and lead time to manufacture a mold for each rotor. Instead, rotors were fabricated using PolyJet 3D printing and carbon fiber molding with readily available in-house equipment.

3.2.1 PolyJet 3D Printing

Also known as rapid prototyping, PolyJet printing is an additive material technique, which works very similarly to an inkjet printer. But instead of ink, the PolyJet printer head deposits two types of materials, an ultraviolet (UV) curable liquid resin and a gel-like support material, in thin layers.[50] The gel-like support temporarily holds the resin, which is formed into the designed rotor. Once all the layers have been deposited and cured, the support material can easily be washed from the rotor with a high pressure water jet.

The PolyJet printer used specifically in this research study was the Objet Eden350V with rigid VeroGrey FullCure850 resin and FullCure 705 photopolymer support material. This machine has excellent build quality with a layer resolution of 16 microns,[50] suitable for clean aerodynamic flow. With this machine, virtually any rotor geometry could be produced by generating a computer aided design (CAD) model and then exporting it to the printer as a certificate trust license (.stl) file. To obtain a baseline rotor design as a starting point, existing commercial propellers, such as the EP-0320, were measured and then averaged. The averaged dimensions are shown in Figure 3.1. The total rotor diameter, blade length, and rotor hub diameter were constrained to keep the overall vehicle scale to a minimum. However, other parameters such as airfoil

section, chord length, and blade pitch could be easily modified in the CAD model and then accurately replicated by the Objet printer.

3.2.2 Carbon Fiber Composite Molding

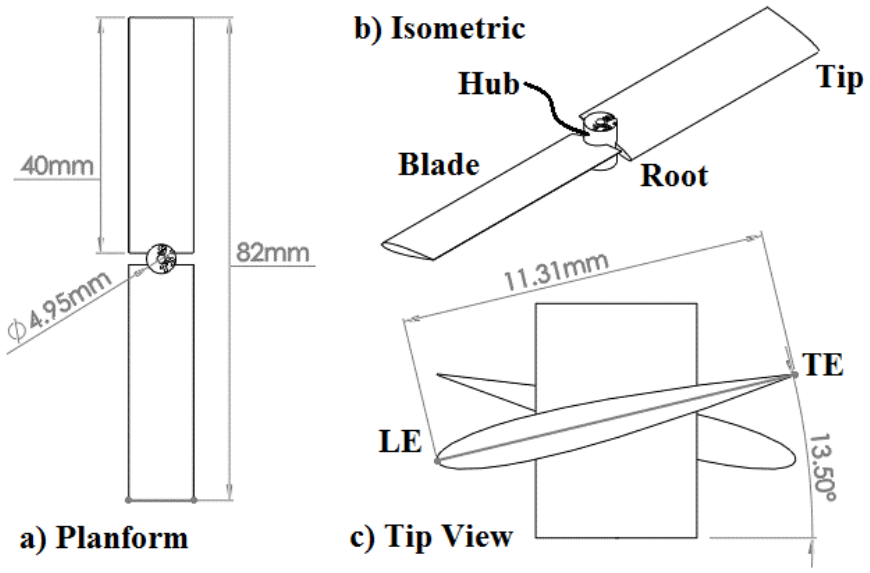

Figure 3.1: Baseline rotor three-view diagram
a) top-down view of the planform, b) isometric, c) inboard view from the blade tip. Blade length (40 mm), rotor diameter (82 mm), and hub diameter (4.95 mm) as seen in the planform view were held as fixed parameters for all rotor variations. Initial blade chord was 11.31 mm and the pitch is 13.5 degrees.

In addition to the PolyJet rapid prototyping process, carbon fiber composite (CFC) blades were fabricated to examine the influence of different materials on rotor performance. CFC is a popular material in the aerospace industry due to its relatively high strength-to-weight ratio, and its thin, woven structure makes it ideal for airfoil surfaces. Becasue carbon fiber is flexible before it is permeated with a curable resin, it

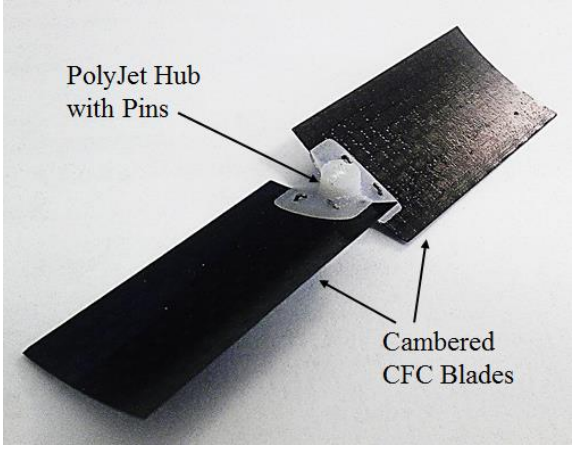

Figure 3.2: Example CFC rotor
Blade chord is 21.4 mm and camber is 6.1%. All CFC rotor blades are nominally 0.25 mm thick. A slot-and-pin configuration held the CFC blades in the rotor hub as testing was conducted.

can be easily molded to a number of shapes. Once the resin cures, CFC maintains a rigid structure. It was observed that at the same thickness, CFC withstood deformation better than VeroGrey FullCure850 resin. This made CFC desirable from an aerodynamic-load-bearing and weight-saving point of view. However, given that CFC molding is not an additive material process like PolyJet printing, the variety of rotor designs is much more limited than those that can be achieved with rapid prototyping. The biggest disadvantage is the inability to quickly and accurately mold airfoil profiles with a chord lengths as small as 11.3 mm.

Factory machined metal molds were viewed as an infeasible option due to the large fabrication costs and lead times required for multiple, incremental design variations. Instead, a more efficient and cost-effective method was used in which a single layer of heat-cured carbon fiber was clamped between two bisected aluminum

tubes. This mold assembly was then heated in an industrial oven at 350 °F for 2 hours to cure the CFC as a thin cambered plate. Multiple camber increments could be achieved by using aluminum tubes with a different radius and/or changing the chord length of the blades. The pre-cured CFC thickness is 0.5 mm. After curing in the clamped tube mold, the blade thickness is uniformly 0.25 mm which is independent of chord length or camber. Fabricating the CFC rotor blades separately from the rotor hub allowed the blades to be reused and tested at multiple pitches. To ensure that the CFC blades could be tested at the correct pitch increments, the same PolyJet printing process as described in the previous section was used to create rotor hubs with tight fitting slots for the blades. To temporarily fix the blades in place, holes were drilled close to the root of the blades, through which metal pins could be inserted as seen in Figure 3.2. While this fabrication process limits the variety of CFC rotor parameters that can be investigated, previous research has shown that carefully designed CFC cambered plate airfoils can outperform conventional airfoil sections at the MAV-scale[51].

3.3 Performance Measurements and Experimental Test Setup

Since the goal of this study was to design the most aerodynamically efficient MAV-scale rotor through systematic experimental testing, measures of performance were required to analyze each rotor. Two such existing measures are figure of merit (*FM*) and power loading (*PL*).

3.3.1 Quantifying Rotor Performance

Figure of merit was the primary means for determining a rotor's overall hover efficiency. It is defined as the ratio of ideal power required to hover over the actual (measured) power required. This relation is represented in equation (3.1):

$$FM = \frac{C_T^{3/2}/\sqrt{2}}{C_P} \tag{3.1}$$

where C_T is the experimentally determined thrust coefficient and C_P is the experimentally determined power coefficient. These are nondimensional parameters with equations given by equations (3.2) and (3.3):

$$C_T = \frac{T}{(\rho A \Omega^2 R^2)} \tag{3.2}$$

$$C_P = \frac{P}{(\rho A \Omega^3 R^3)} \tag{3.3}$$

where T is thrust, ρ is air density, A is the rotor disk area, Ω is rotational speed in rad/s, R is the radius of the rotor disk, and P is rotational power (torque × Ω). These were all quantities which had to be measured for each experimental test to determine the figure of merit. Rotors with higher figures of merit have increased sectional lift-to-drag ratios and decreased induced power losses.

The second measure used to evaluate rotor performance was power loading. Power loading is simply a measure of thrust produced by the rotor over the rotational power required as seen in equation (3.4) below.

$$PL = \frac{T}{torque \times \Omega} \tag{3.4}$$

It is evident from this equation that more efficient rotors increase power loading by maximizing thrust produced and minimizing torque for a given rotational speed, Ω. Since these are three quantities which were also required to calculate figure of merit, no additional measurement equipment was need to quantify power loading.

Though a goal of this research was to increase the flight endurance of MRAVs, electrical power consumption was not yet considered as a measure of performance (see Chapter 4). Electrical efficiency would not be an accurate measure of isolated rotor efficiency since additional power is lost to excess components and wire length required for the test setup. Furthermore, electric motors have an optimal rotational speed which is likely different than the rotor's optimal rotational speed. A set of gears can be incorporated between the motor shaft and rotor which allow each to operate at its optimal rotational speed simultaneously. However, this is not considered in the current chapter since the focus is optimizing the aerodynamic efficiency of MAV-scale rotors.

3.4 Experimental Test Setup

In order to determine the performance of each rotor, a testing apparatus, as seen in Figure 3.3, was devised to measure the necessary, fundamental quantities introduced in the previous section. The rotor itself was placed directly on the motor shaft and held in place by friction. The motor used was an AP03 4000kv brushless DC motor. The motor base was attached to a 155 mm long isolation stand. The purpose of the stand

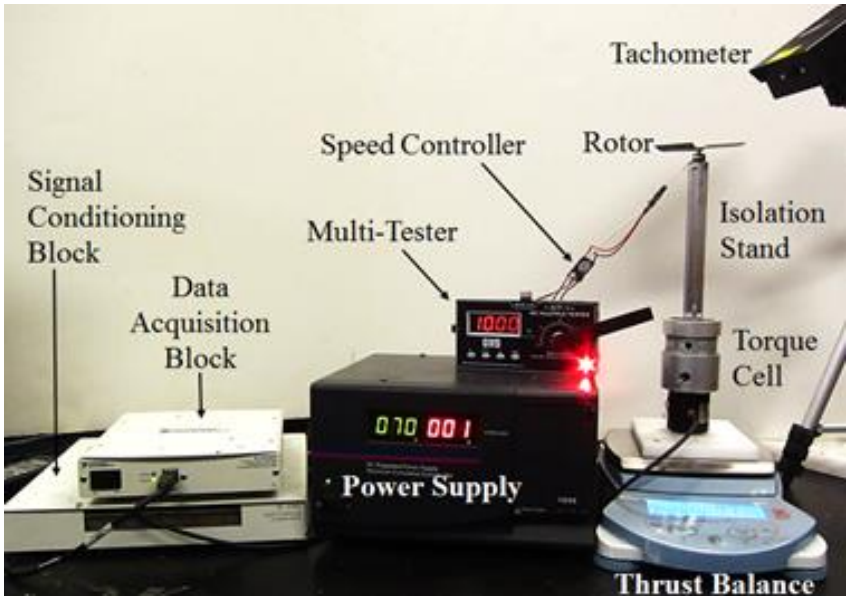

Figure 3.3: Rotor hover testing setup and required hardware
Not pictured is a desktop computer used to gather, process, and store the test data.

was to separate the rotor from any equipment or obstacles that could affect the air flow dynamics and produce inaccurate results. The rotor was also flipped upside down relative to a conventional rotor configuration. This is shown in Figure 3.1 where the leading edge is angled down relative to the trailing edge. In this configuration, the rotor would spin clockwise and would thrust down rather than up. This further isolated the rotor wake from interfering with surrounding equipment which could produce undesirable ground effects.

The thrust produced by the rotor was measured by an OHAUS Adventure Pro AV4101 balance with 0.1 gram precision. Between the isolation stand and thrust balance was a 5 in-oz reaction torque sensor. This was directly connected to a National Instruments (NI) SC-2345 signal conditioning connector block. This was connected to

an NI USB-6251 data acquisition block, which sampled the output voltage signal from the torque cell. The data acquisition block was connected via USB cable to a computer with a LabVIEW 8.6 program which converted and saved the voltage signal as torque measurement in N-m. The angular speed of the rotor was manually measured with a Monarch laser Tachometer. Rotor speed was varied manually with a GWS MT-1 multi-tester. A Thunderbird 9 speed controller regulated the pulse width modulation signal from the multi-tester to the motor. The speed controller also regulated power between the motor and the BK Precision 1690 DC Power Supply. Lastly, a Cole-Parmer digital barometer was used to measure atmospheric temperature and pressure so that the air density could be calculated for each test run.

3.4.1 Experimental Procedure

To obtain rotor performance data, each rotor was tested over multiple rotational speeds, typically 8000 to 12000 rpm. Within this operational range, the rotors typically provided enough thrust (>25 g) to theoretically lift and maneuver its portion of a 100 g quadrotor. Furthermore, the figure of merit results were not consistent with each other at lower rotational speeds (3000 – 7000 rpm), but remained approximately constant at higher speeds. Test runs did not exceed 12000 rpm to avoid motor burnout.

Before each rotor was tested, ambient pressure and temperature measurements were recorded. Experimental test runs for each rotor started at 8000 rpm. The rotational speed was manually varied with the multi-tester to within ± 10 rpm of the target value. Then, the LabVIEW program was started to capture and average the rotor torque over

3 seconds. During this time interval, the actual rpm was recorded from the Tachometer and the thrust was recorded from the digital balance. This process was repeated at 9000, 10000, 11000, and 12000 rpm. Then, the procedure was repeated for second set of measurements from 8000 to 12000 rpm for a total of 10 test runs. The data was averaged for each rpm to obtain more accurate measurements. The figure of merit for the three highest rpms was averaged for an overall measure of rotor performance. The power loading was not averaged over a range of rotational speeds since it is a direct function of Ω.

3.5 Rotor Optimization Methodology and Results

The rotor described in Figure 3.1 was the initial baseline rotor for the systematic, variation-of-parameters optimization method. As stated previously, the only parameters that remained fixed in all design iterations were, blade length, rotor diameter, and hub diameter. Parameters that were systematically varied include airfoil section, camber, blade thickness, solidity, number of blades, geometric twist, and chord taper ratio. For each parameter iteration, blade pitch was incrementally increased by 2° for a total of at least 5 different blade pitches. This had the effect of increasing the blade loading coefficient (C_T/σ) which is defined as the thrust coefficient normalized by the rotor solidity (σ). Solidity is the ratio of solid blade area to rotor disk area (πR^2). For rectangular blades used in this study, solidity can be defined by equation (3.5), where N_b is the number of rotor blades.

$$\sigma = \frac{N_b c}{\pi R} \tag{3.5}$$

Figure of merit was potted against blade loading to generate performance curves for each design iteration. Another set of performance curves was generated by plotting power loading against disk loading. Disk loading is defined as the thrust produced over the rotor disk area. Unlike the *FM* curves, each *PL* curve represents a fixed blade pitch but varying rotational speed. The *PL* curves were only plotted for blade pitches which resulted in the highest figure of merit for a particular design iteration. These two types of performance curves were used to graphically determine which design iteration for each rotor parameter produced the largest increase in aerodynamic efficiency.

3.5.1 Effect of Airfoil Section

As stated previously, it was known that *FM* increases as the rotor blade sectional lift-to-drag increases. Therefore, airfoils with high lift-to-drag ratios at low Reynolds numbers were primarily examined. Theoretical lift-to-drag ratios were obtained from an online airfoil database in order to choose a set of potential high-performance airfoils such as Eppler-63 and AH-7-47-6. These were compared against each other and conventional large-scale helicopter airfoils such as the NACA 0012 airfoil as seen in Figure 3.1. Thin, cambered plate airfoils fabricated from CFC were also examined. A sample of the tested airfoil sections is shown in Figure 3.4. Since

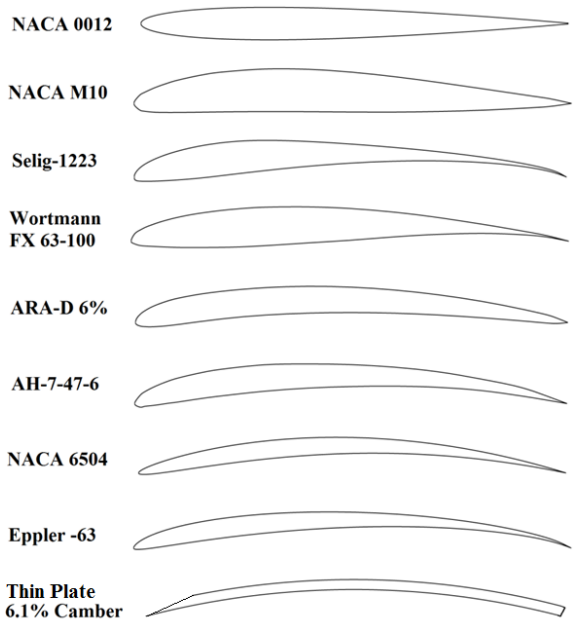

Figure 3.4: Examples of tested airfoils arranged from lower to higher *FM*

only airfoil section was varied for these tests, other fixed parameters were c = 11.3 mm, σ = 0.17, and N_b = 2.

The performance results of varying blade airfoil section are represented by *FM* in Figure 3.5. Rotor tip Re for these data sets is approximately 30,000. From these results, it was observed that the three highest performing airfoils were the NACA 6504 (*FM* = 0.57), Eppler-63 (*FM* = 0.57), and 6.1% cambered plate (*FM* = 0.59). This was dramatic increase from the baseline rotor with a NACA 0012 airfoil (*FM* = 0.46). This large performance gap can be attributed to key airfoil characteristics depicted in Figure 3.4, primarily camber and thickness-to-chord ratio (t/c). The NACA 0012 is symmetric and relatively thick with t/c = 12%, whereas the high performance airfoils are thin and moderately cambered. The cambers of these airfoils are: 6% (NACA 6504), 5.3%

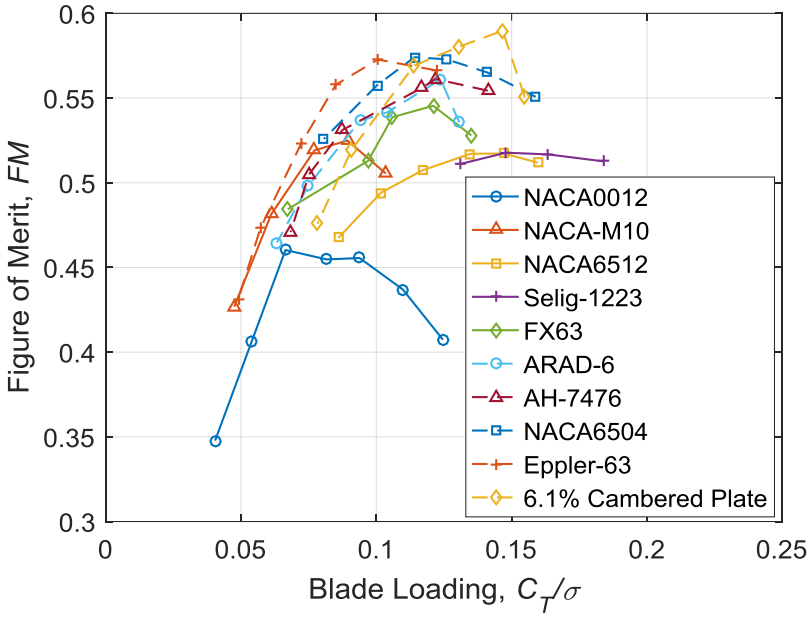

Figure 3.5: Effect of varying blade airfoil section on rotor *FM*

(Eppler-63), and 6.1% (cambered plate). Max camber position is at 50% chord for all three airfoils. The t/c of these airfoils are: 4% (NACA 6504), 4.3% (Eppler-63), and 2.2% (cambered plate). The cambered plate airfoil could only be fabricated from CFC since a PolyJet resin replica was too flexible, resulting in dramatically lower performance. The key trend observed from these experiments was that low Reynolds number rotor efficiency increased as airfoil t/c is decreased to minimal structural limits, and airfoil camber is increased to approximately 6%. Therefore, the effects of pure camber or thickness variation were examined in further detail with standard cambered plate and NACA airfoils.

3.5.2 Effect of Airfoil Camber

It was observed that rotor with a 6.1% cambered plate airfoil produced the highest overall figure of merit in the preliminary airfoils experiments. Therefore, rotor blades with a camber value similar to 6.1% were tested to determine a trend in rotor efficiency. These results are displayed as figure of merit performance curves in Figure 3.6. The performance curves show that the maximum *FM* is more comparable for thin plates with 4.5% and 6.1% camber than 7.4% camber. These findings agreed with results from the previous airfoil tests where airfoils with camber between 4.5% and 6.1% increased rotor performance more than camber values outside this range.

To further investigate the effect of camber on rotor performance, standard 4-digit NACA airfoils were used. These were chosen since the camber can easily be

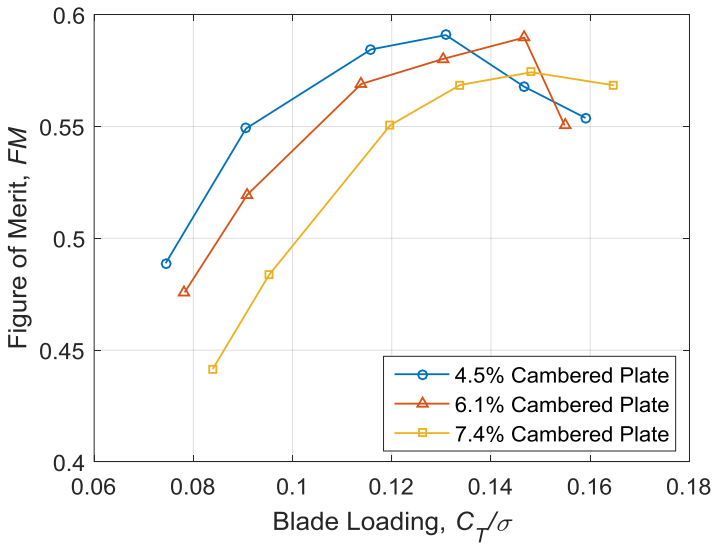

Figure 3.6: Effect of varying CFC blade camber on rotor *FM*

determined from the first digit and *t/c* can be directly determined from the last two digits in the designation. Therefore, the effect of camber variation could be isolated without completely changing the airfoil section. NACA airfoil cambers examined were 3%, 4%, 5%, and 6%. This range of camber was tested in sets of airfoils with constant *t/c* of 4%, 6%, 8%, and 12%. The *FM* performance results of varying camber for 4% *t/c* are shown in Figure 3.7(a). The *FM* performance results of varying camber for 6% *t/c* are shown in Figure 3.7(b). Rotor tip Re for these data sets is approximately 30,000.

It is observed in these results that for both thickness-to-chord ratios, maximum *FM* is relatively unchanged for rotors with airfoil camber between 4% and 6%. However, just below this range, at 3% camber, rotor performance drops significantly. This same trend was also observed for the 8% and 12% NACA airfoil sets. The results of the preliminary airfoil tests indicated that rotors with an Eppler-63 airfoil had the highest aerodynamic efficiency among PolyJet printed rotors. And, the results of the incremental-camber-variation tests indicated that camber values within the 4 – 6% range optimized performance for NACA airfoil and CFC rotors. Therefore, the camber of the Eppler-63 (camber = 5.3%) was slightly varied between 4% and 7.4% to determine if performance could be further optimized. The results showed that an Eppler-63 airfoil with 6.1% camber (designated Eppler-63-61) marginally improved figure of merit to 0.59 from 0.57. This was comparable to the 6.1% cambered plate rotor which also had a figure of merit of 0.59. Therefore, these were the two primary airfoils considered in the next rotor parameter variation tests.

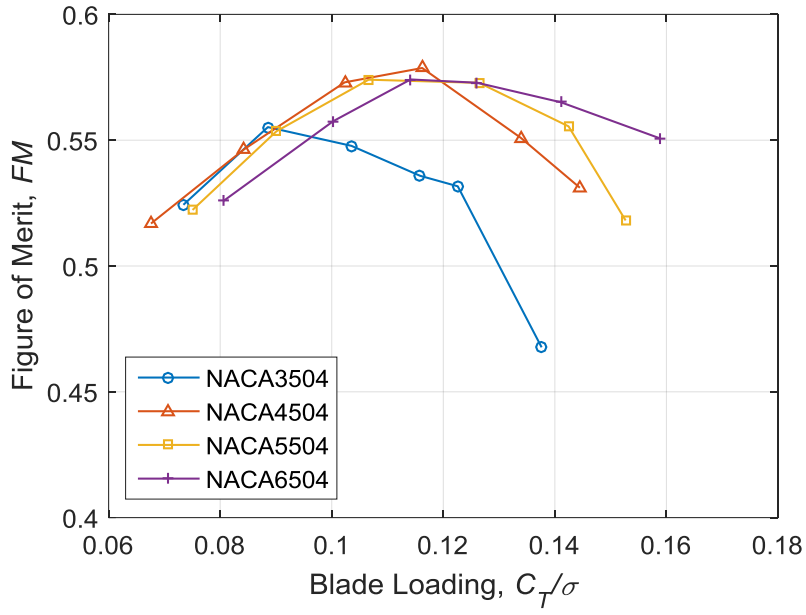

a) 4% thickness-to-chord

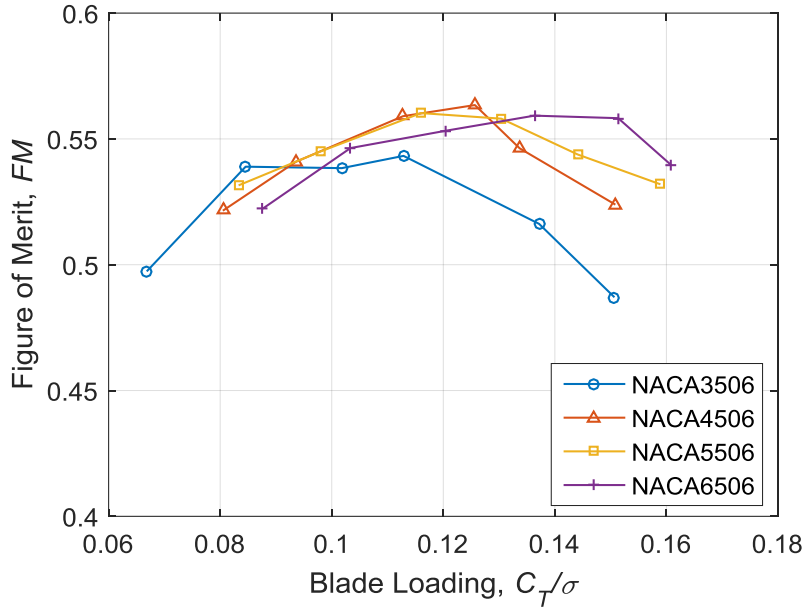

b) 6% thickness-to-chord

Figure 3.7: Effect of varying camber on rotor *FM* with 4% and 6% *t/c*

3.5.3 Effect of Airfoil Thickness

In the preliminary airfoil experiments, it was observed that rotor performance tended to increase as airfoil t/c decreased. The airfoil *t/c* of the three high performance rotors were: 4% (NACA6504), 4.3% (Eppler-63), and 2.2% (6.1% cambered plate). And, the airfoil *t/c* of the three low performance rotors (NACA0012, NACA6512, and Selig-1223) were all 12%. Therefore, the effect of airfoil thickness on rotor performance was further studied with incremental variations in NACA airfoil *t/c*. The thickness-to-chord ratios examined were 4%, 6%, 8% and 12%. This range of *t/c* was compared in sets of airfoils with constant cambers of 3%, 4%, 5%, and 6%. The FM performance results of varying *t/c* for 4% camber are shown in Figure 3.8(a). The FM performance results of varying *t/c* for 6% camber are shown in Figure 3.8(b).

It is evident from these results that, for both 4% and 6% camber, rotor FM increases as airfoil *t/c* decreases. Furthermore, similar results were observed in the 3% and 5% camber sets. Again, this agrees with the trend that emerged from the preliminary airfoil experiments. It should also be noted that the effect on performance is much more pronounced for varying thickness rather than camber. This indicates that a crucial objective for optimizing low Reynolds number rotors is to minimize blade thickness. However, there is a structural limit which prevents decreasing blade t/c past 4% for PolyJet rotors with c = 11.3 mm. Experiments were attempted at 3% *t/c*, but severe blade deformation by aerodynamic loads caused performance to drop significantly. Since the rotors with Eppler-63-61 and 6.1% cambered

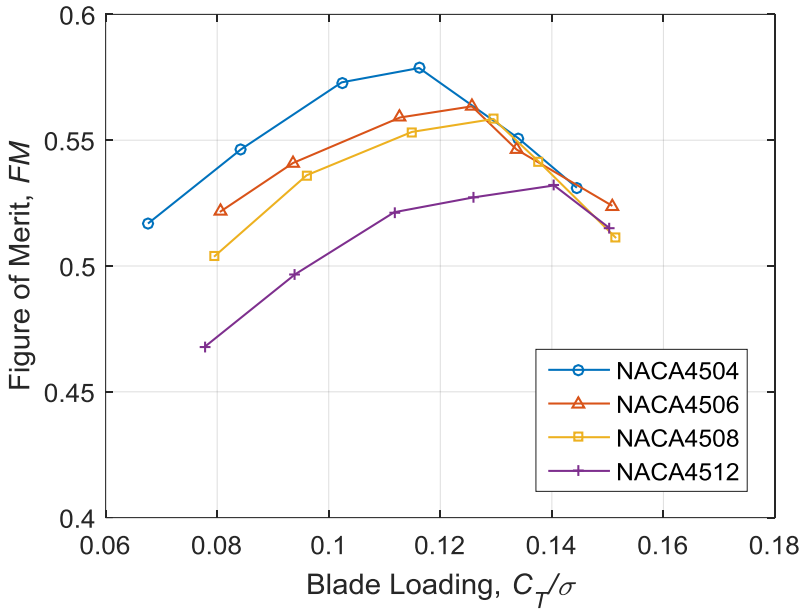

a) 4% camber

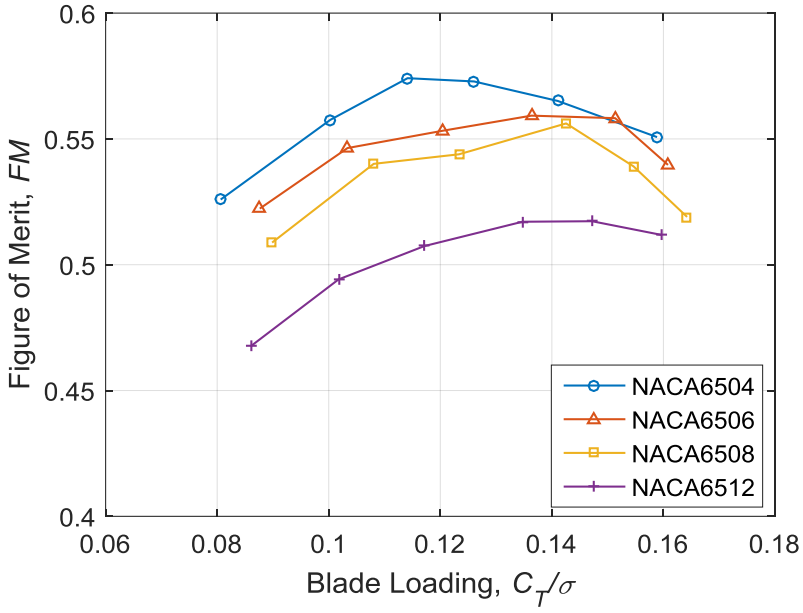

b) 6% camber

Figure 3.8: Effect on rotor *FM* by varying *t/c* for two airfoil cambers

plate airfoils were already at their structural limits, no further optimization could be done in terms of *t/c* for these two airfoils specifically.

3.5.4 Effect of Solidity and Number of Blades

After determining two optimal rotor blade airfoil sections, the next major parameter to investigate was rotor solidity. As defined in Eqn. (3.5), solidity (σ) is the ratio of solid rotor planform area to total rotor disk area. Solidity tests were conducted by varying chord length and/or the number of blades. In all previous tests, rotors were 2 bladed with c = 11.3 mm and σ = 0.17. To maintain 6.1% camber for the thin plate airfoils as solidity changed, different diameter pipe molds were used so that chord length could be varied. For these experiments, the following solidities and their corresponding chord lengths were investigated: σ = 0.14 (c = 9.4 mm), σ = 0.17 (c = 11.3 mm), σ = 0.23 (c = 15.3 mm), σ = 0.32 (c = 21.4 mm), and σ = 0.42 (c = 27.6 mm). Rotor tip Re is approximately 30,000 to 40,000 for these data sets. The results of these experiments are shown in Figure 3.9(a) as *FM* performance curves. The results are also shown as power loading curves in Figure 3.9(b) to provide further validation. From these results, it is evident that performance for 2-bladed, 6.1% cambered plate rotors increases as chord length increases up to 21.4 mm. It should be noted that the maximum *FM* of the high solidity (σ = 0.32) rotor greatly improved compared the standard solidity (σ = 0.17) rotor. Optimizing the chord length of the 2-bladed, 6.1% cambered plate rotor increased the maximum *FM* from 0.59 to 0.62.

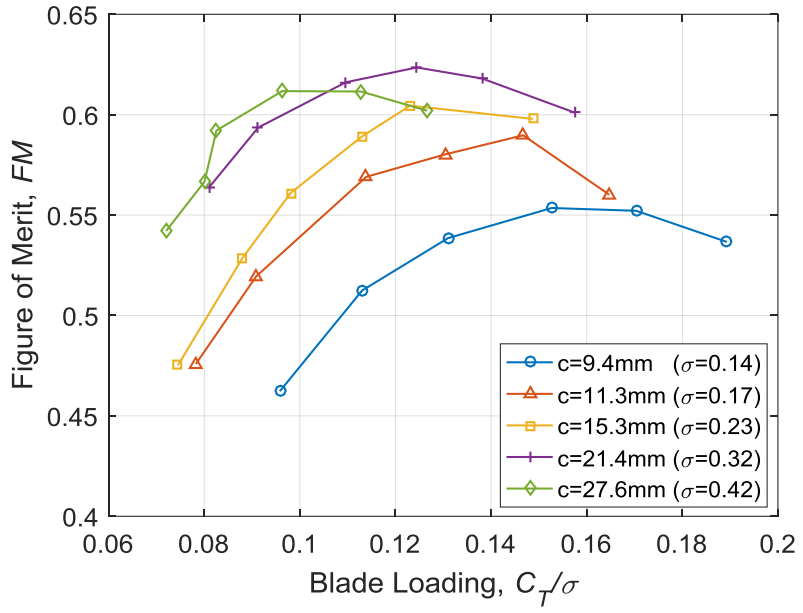

a) Figure of merit vs. blade loading coefficient

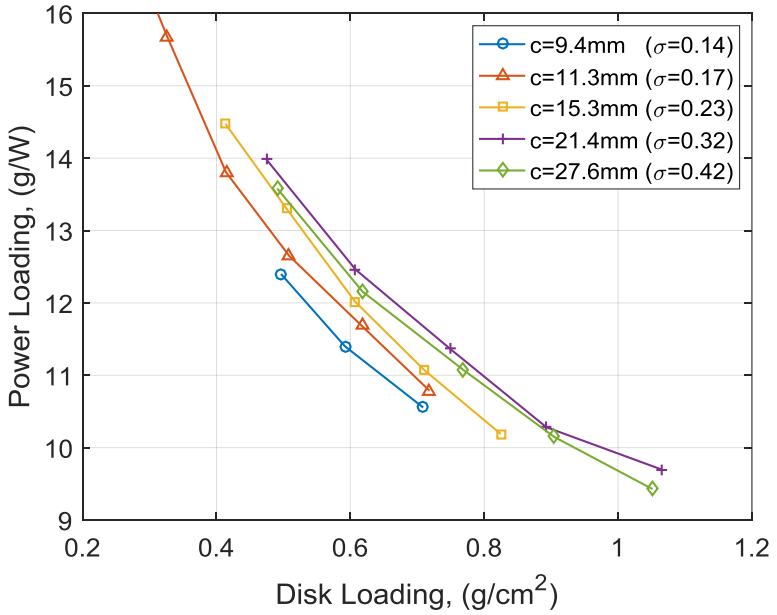

b) Power loading vs. disk loading

Figure 3.9: Effect on rotor performance by varying chord length; N_b = 2, 6.1% cambered plate airfoil sections

However, it is unclear whether the higher aerodynamic efficiency is due to a general increase in solidity or specifically the increase in chord for 2-bladed rotors. To differentiate between the two factors, 3 and 4-bladed rotor test were conducted with the standard chord length (c = 11.3 mm) as a fixed parameter. The comparison between rotors with 2, 3, and 4 blades but fixed chord length is shown in Figure 3.10. Rotor tip Re is approximately 30,000 for these data sets. These results show that even though solidity was increased within a similar range as the previous tests, the increasing *FM* trend is not present. This indicates that low Reynolds number rotor performance is significantly more dependent on chord length rather than general solidity. The results given in Figure 3.10 are further supported by the results shown in Figure 3.11. This

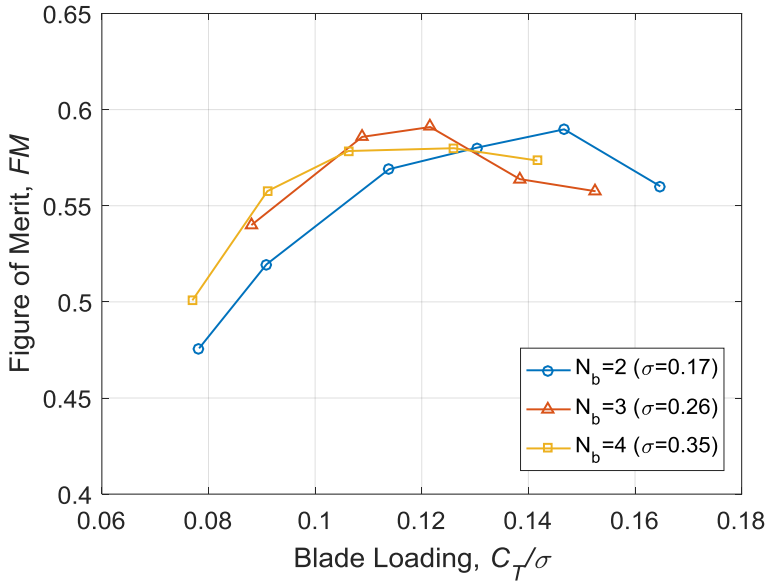

Figure 3.10: Effect on performance by varying blade number with fixed chord length (11.3 mm) and 6.1% cambered plate airfoil sections

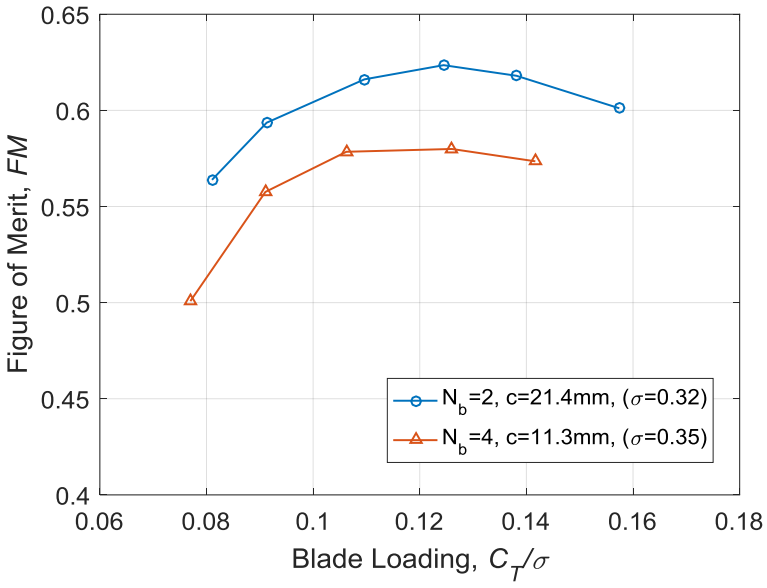

Figure 3.11: Effect on performance by varying blade number with similar solidity (6.1% cambered plate airfoil sections)

plot shows that two rotors with similar solidity have significantly different performance characteristics due the different distribution of planform area over multiple blades.

Similar solidity experiments were conducted with PolyJet rotors with Eppler-63-61 airfoils. However, unlike CFC results, neither increasing chord length nor the number of blades increased aerodynamic performance. This could be attributed to the implicit relationship between chord length and *t/c*. It was known from the airfoil thickness tests that high performance, low Reynolds number rotors are characterized by minimum airfoil *t/c*. Since the CFC thickness is fixed at 0.25 mm, *t/c* will decrease as chord length increases (e.g. *t/c* = 2.3% for *c* = 11.3 mm and *t/c* = 1.2% for *c* = 21.4 mm). However, as the Eppler-63-61 is scaled up by chord length, thickness will also

scale up and *t/c* will remain constant. Therefore, optimal solidity was achieved with a 2-bladed, 6.1% cambered plate CFC rotor with c = 21.4 mm and t/c = 1.2%.

3.5.5 Effect of Chord Taper

Existing research and rotor design theory has determined that tapering the chord along the length of a rotor blade can improve aerodynamic efficiency for large-scale helicopters[52]. Therefore, chord taper experiments were also conducted to determine if similar principles applied to MAV-scale rotors. Chord taper ratio (*CTR*) is defined as the ratio of tip chord length to root chord length (e.g. $CTR = 1$ corresponds to a rectangular blade and $CTR < 1$ corresponds to a blade with tip chord less than root chord). Introducing chord taper has the effect of changing geometric solidity, which

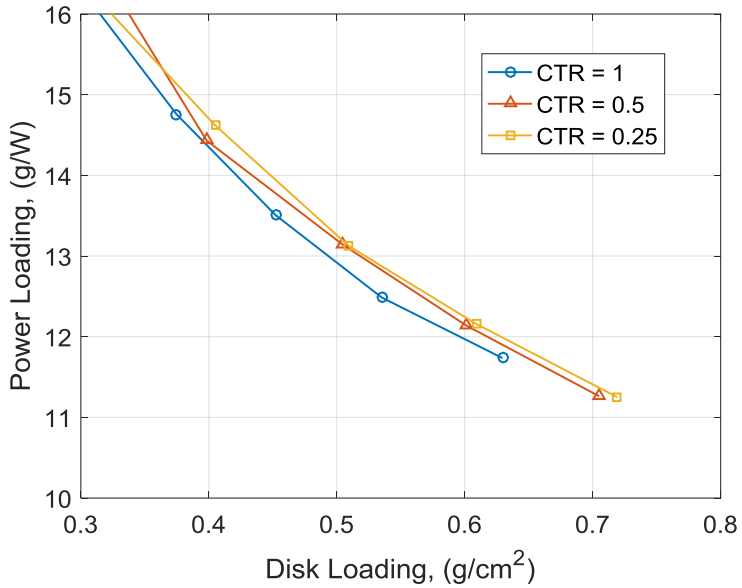

Figure 3.12: Effect of chord taper on power loading (Eppler-63-61 airfoil, $N_b = 2$, $\sigma = 0.17$)

could potential skew results. However, helicopter theory states that tapered and untapered rotors can be considered to have an equivalent trust weighted solidity as long as the chord at 75% blade span for a linearly tapered rotor equals the rectangular blade chord length[52]. Therefore, all rotors in the linear taper experiments were designed with 11.3 mm chord at 75% blade span and 0.17 thrust weighted solidity. To ensure tapered blades were fabricated accurately, PolyJet printed rotors with Eppler-63-61 airfoils were used. As seen in Figure 3.12, the results of the taper variation show that marginal performance improvements can be attained for $CTR < 0.5$.

3.5.6 Effect of Blade Twist

Helicopter rotor design theory predicts that induced power requirements can be drastically reduced by gradually decreasing the sectional blade pitch along the span of the rotor blade (negative twist)[52]. Therefore, incremental blade twist experiments were conducted to determine if induced power could be decreased for low Reynolds number rotors as well. Similarly to the taper experiments, blade twist was incorporated as a linear function of radius where the 75% blade span pitch was a known parameter. A larger negative twist value indicates that the root pitch is much greater than the tip pitch. Because twist could not be easily incorporated into CFC blades, PolyJet printed rotors with Eppler-63-61 airfoils were used. As seen in Figure 3.13, the results of the blade twist experiments show that significant performance improvements are only attained for highly twisted blades (between -10° and -20° of twist).

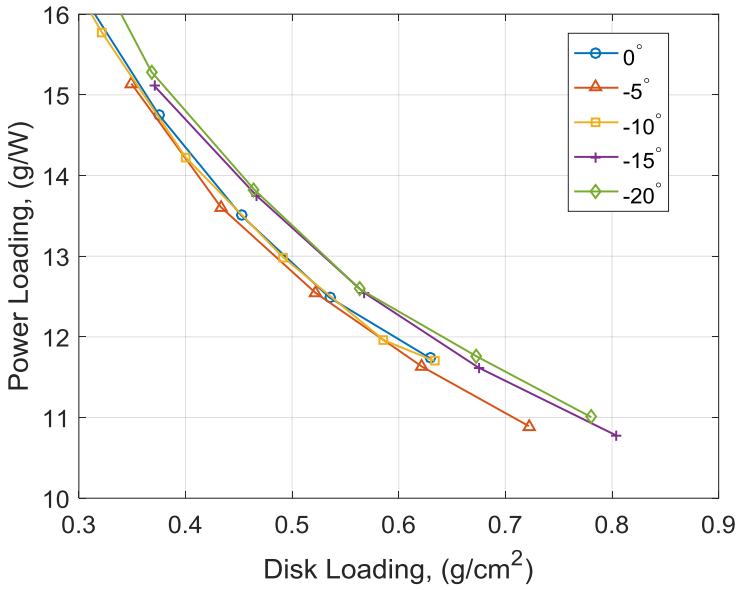

Figure 3.13: Effect of blade twist on power loading (Eppler-63-61 airfoil, $N_b = 2$, $\sigma = 0.17$)

3.5.7 Design of the Optimal Rotor

The final rotor design, shown in Figure 3.14, was based on a combination of the results gathered from the previous studies on individual rotor parameters. These were the optimal parameters that had to be incorporated into the final rotor design:

1) 0.25 mm thick CFC rotor blade material
2) 6.1% cambered thin plate airfoil section
3) 0.32 thrust weighted solidity with 2 blades
4) 0.25 to 0.5 chord taper ratio
5) -10° to -20° twist rate per blade

The key challenge in fabricating the optimal rotor design was determining how to incorporate the chord taper and twist rate. Since the CFC blades are shaped as

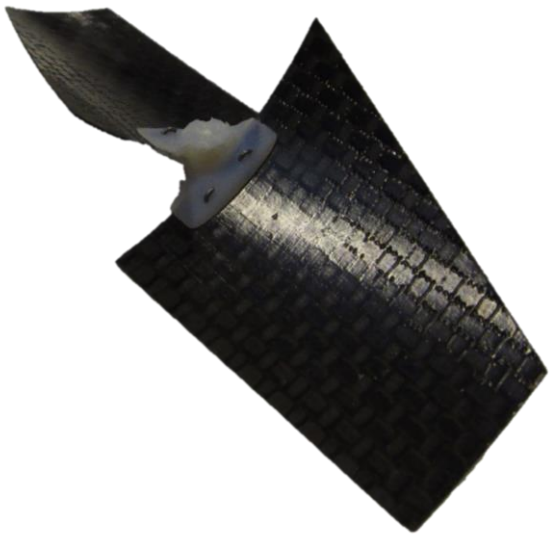

Figure 3.14: Optimized rotor design

cambered plates with constant curvature along the blade span, chord length, camber, and twist rate are automatically coupled. By keeping the leading edge of the blade straight and tapering the trailing edge, spanwise pitch and camber variation could be achieved. Therefore, the trailing edge taper line had to be calculated such that twist rate and camber would be within the optimal ranges. The rotor blade was designed such that the chord at 75% span was 21.4 mm, resulting in a thrust weighted solidity of 0.32. Furthermore, this meant that the camber at 75% blade span was 6.1%. With these fixed parameters, a trailing edge *CTR* of 0.5 was selected which resulted in an approximate twist rate of -11.4°. These rotor blades were tested at multiple collective pitches in the same manner as the previous CFC blades. The results of the tests showed that an optimal pitch at 75% blade span for this rotor design is 19.5°. The performance results of the final micro-rotor design are represented in Figure 3.15. The optimized rotor

design achieved a maximum *FM* of 0.66, which represents a 34% increase in performance from the initial, baseline rotor (denoted NACA0012 in Figure 3.5).

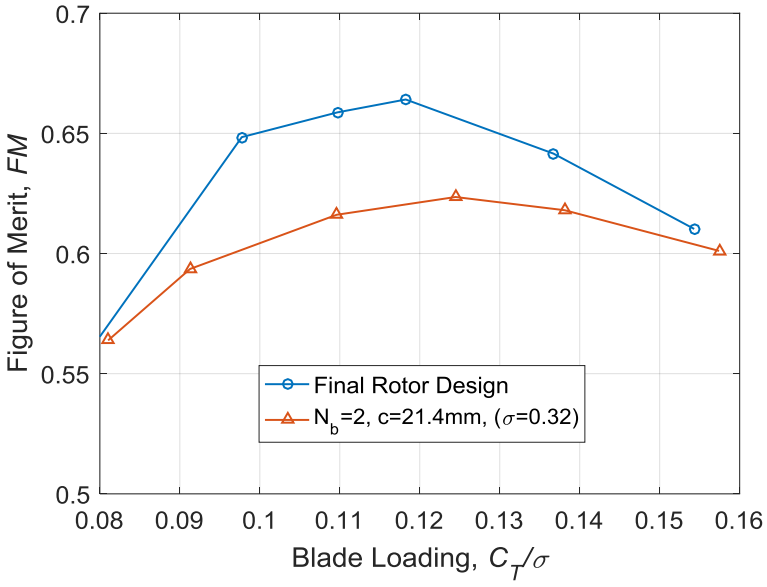

Figure 3.15: Maximum *FM* achieved with the final rotor design

3.6 Micro-Rotor Experiment Conclusions

As described in Chapter 2, sectional aerodynamics at low Reynolds numbers are characterized by efficiency losses such as strong viscous drag forces and large laminar separation bubbles. It was determined that variations in airfoil characteristics, such as thickness, camber, and leading edge shape, have a strong effect on sectional lift-to-drag. Therefore, a comprehensive, multi-parameter investigation was completed to determine how these characteristics effect performance in a low Reynolds number rotor application. Similar to the findings in Chapter 2, thin airfoils with moderate

camber were found to improve aerodynamic efficiency. It was observed in the thickness-to-chord and solidity experiments that a thin (t/c = 1.2%) plate with 6.1% camber is the optimal airfoil design, provided the rotor blade is fabricated from CFC. The results of the N_b solidity experiments indicated that 2-bladed rotors with a large chord (c = 21.4 mm) outperform rotors of the same solidity with 3 or 4 blades. The results of the chord taper experiments showed that highly tapered blades (*CTR* 0.25 - 0.5) improve rotor performance. The results of the blade twist experiments indicated that -10° to -20° of twist per blade is required to further improve performance. A final rotor was designed which incorporated all of the individual optimal parameters determined from the previous tests. This rotor design achieved a maximum *FM* of 0.66 which represents 34% efficiency increase over the initial baseline rotor. However, the effects of twist and taper were not examined as thoroughly as other parameters. In these experiments, twist and taper were only incorporated as linear functions of blade span. To further optimize rotor performance, future experiments should focus on other methods of tapering chord length and twisting blade pitch.

Chapter 4: High Endurance Quadrotor Prototype

An important aspect of the present research was to incorporate the knowledge gained in low Reynolds number sectional and rotor aerodynamics into an improved micro rotary-wing air vehicle (MRAV) design. Even though improving the aerodynamic efficiency of the rotor is a crucial step, increasing MRAV hover endurance will require maximizing the overall system efficiency. Current research-based and commercial micro-quadrotors are not designed to efficiently extract the maximum flight endurance from a limited power source for multiple reasons[53]. The rotors used may not have been designed for low Reynolds number application. The motors and transmissions have not been appropriately paired with the rotors for maximum efficiency. Current designs where brushless outrunner motors directly drives the rotor simplifies the mechanical design, however, a huge price is paid in terms of motor efficiency. Also, motor speed controller losses, particularly for brushless motors is much higher than that of brushed motors[54]. Battery performance characteristics have not been incorporated into the design[53]. And, the airframe structure is heavily overdesigned and constitutes a large fraction of the gross vehicle weight. The present research aims to examine each of these factors and their interactions to improve system level efficiency.

This chapter details the systematic performance studies as follows: evaluation of brushed and brushless motor system characteristics, optimization of the geared transmission system, evaluation of battery performance characteristics, implementation

of control and stability hardware and algorithm, minimization of airframe weight, gimbal endurance test, and free hover endurance results. The ultimate goal of these optimization studies is to develop an efficient micro quad-rotor weighing under 50 grams with a hover endurance over 30 minutes.

4.1 Electric Motor and Speed Controller Experiments

With the optimal rotor design selected in Chapter 3, further systematic tests were required to determine the optimal rotor-motor pairing in terms of motor efficiency (mechanical power produced per electric power input):

$$\eta_m = \frac{Power\ Out}{Power\ In} = \frac{Q \times \Omega}{V \times I} \tag{4.1}$$

and electrical power loading (thrust produced per electrical power consumed):

$$EPL = \frac{T}{V \times I} \tag{4.2}$$

Both brushed and brushless motors were examined.

4.1.1 Brushed DC Motors

Brushed motors are composed of a rotor, stator, and electrical commutator and brushes, shown in Figure 4.1(a). Permanent magnets are located in the stator and conductive wire coils are located in the rotor. The brushes transmit electrical current to the coils which induces magnetic fields and spins the rotor to align the magnetic poles. The polarity of the coils is passively switched during rotation due to the alternating arrangement of the brushes. By increasing the input DC voltage, the magnetic field

strength increases thereby increasing the rotational speed. This is a simple operation compared to the three phase speed controller required for brushless motors. Additionally, due to their simple construction, brushed motors can be easily downsized to much lower weights[54].

4.1.2 Brushless DC Motors (BLDC)

The brushless DC motor is the second type of DC motor examined. These motors do not use brushes since their conductive coils remain stationary, as seen in Figure 4.1(b). Instead, the polarity of the magnetic field is alternated with the use of a three phase speed controller. These speed controllers phase the current supplied to the coils as well as measure the electro-motive force to determine rotational speed[54]. Since this operation does not require brushes contacting the rotor, friction is decreased resulting in higher speeds and efficiency for brushless motors. However, the electronic speed controller (ESC) has disadvantages that must be considered in the full vehicle

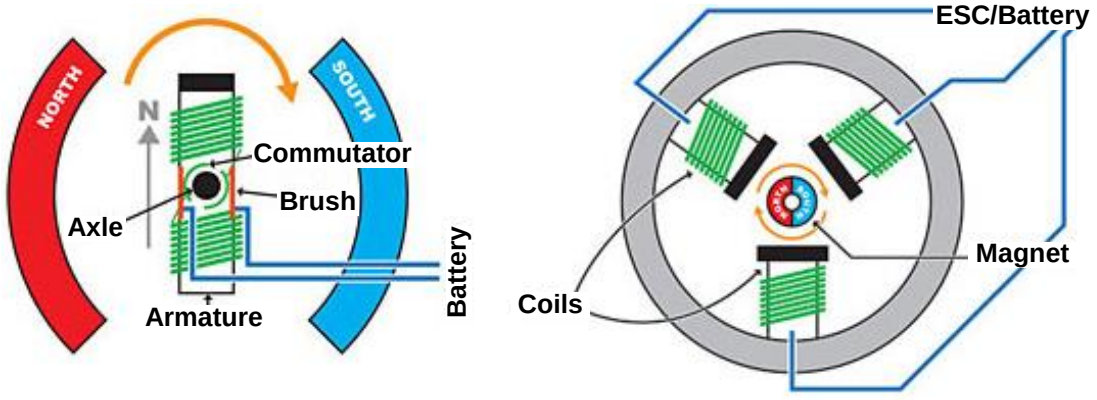

a) Brushed motor b) Brushless (BLDC) motor

Figure 4.1: Schematics for brushed and brushless motors[55]

design. ESCs are usually heavy and incur an additional weight penalty that is disadvantageous for micro air vehicle applications[54]. They also incur their own efficiency losses which will be examined in more detail later.

4.1.3 Motor Performance

Extensive performance studies on small (<5g) brushed and brushless motors were conducted by Harrington and Kroninger[54]. The major findings from these studies are summarized in the current section and were used as a starting point for systematically determining an optimal motor for a micro quadrotor. Figure 4.2 shows that, in general, motor efficiency increases with motor mass.

However, beyond 5 grams, the efficiency gains are marginal as the mass becomes prohibitive for application on a micro quadrotor of size discussed in the

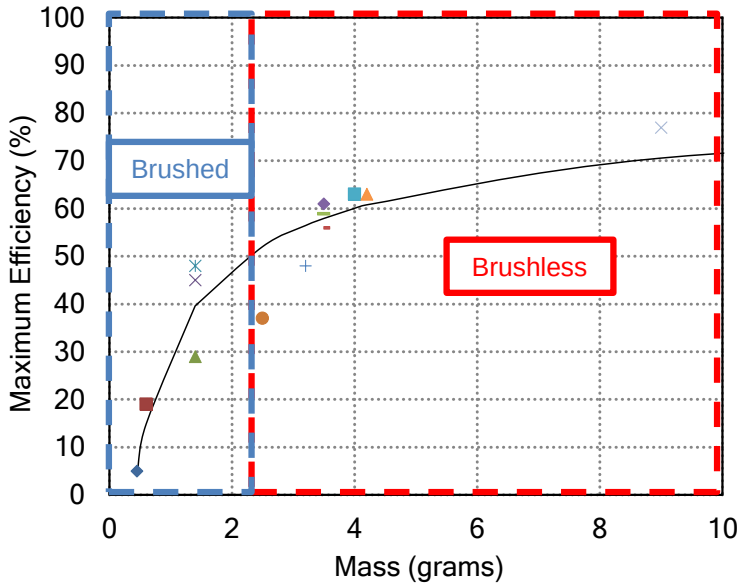

Figure 4.2: Maximum Efficiency vs Mass for a Representative Sample of Brushed and Brushless Motors (adapted from Harrington[54])

present study. According to Figure 4.2, while the brushed motors are lighter, they also tend to be less efficient[54]. Conversely, brushless motors tend to be more efficient but heavier. This means there are only a few brushed motors with high enough efficiency and few brushless motors that are light enough to be considered for a sub-50 gram quadrotor design. Representations of the motor considered in the present research are shown in Figure 4.3

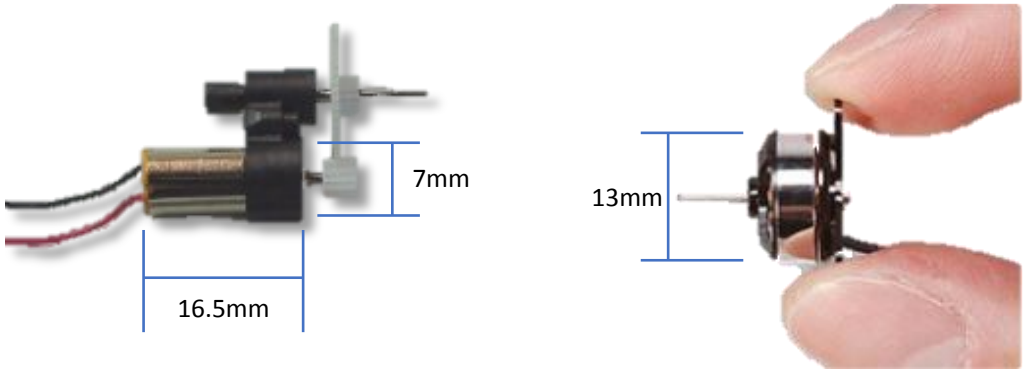

a) SS-type brushed motor with 4:1 gears b) AP03-type BLDC motor

Figure 4.3: Typical small scale brushed and brushless motors

The motor efficiency-weight trade-off needed to be examined further to determine if the increased efficiency of brushless motors was enough to overcome the added weight. This requires an understanding of the operating conditions (torque and RPM) which effect motor efficiency. As seen in Figure 4.4 and Figure 4.5, brushed motor efficiency is strongly influenced by RPM and applied torque for a constant voltage. It is important to note from Figure 4.4 that there are two efficiency values for each power value because of the two possible combinations of RPM and torque. The

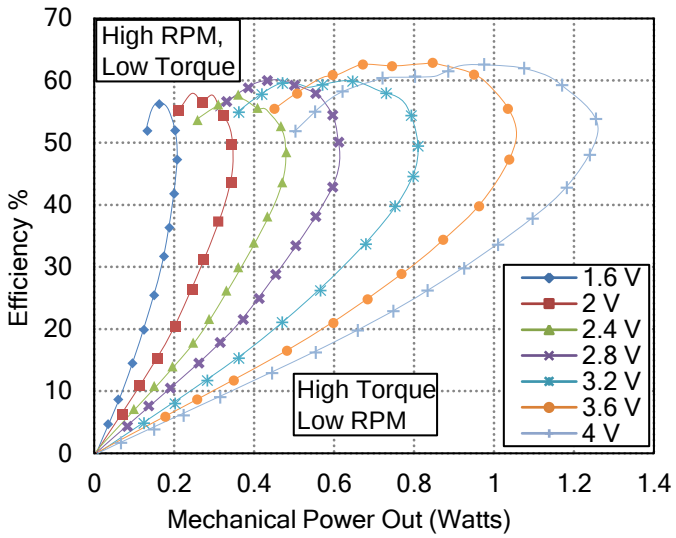

Figure 4.4: Efficiency vs. Motor Power Output for the SS-1.7 Brushed Motor (adapted from Harrington[54])

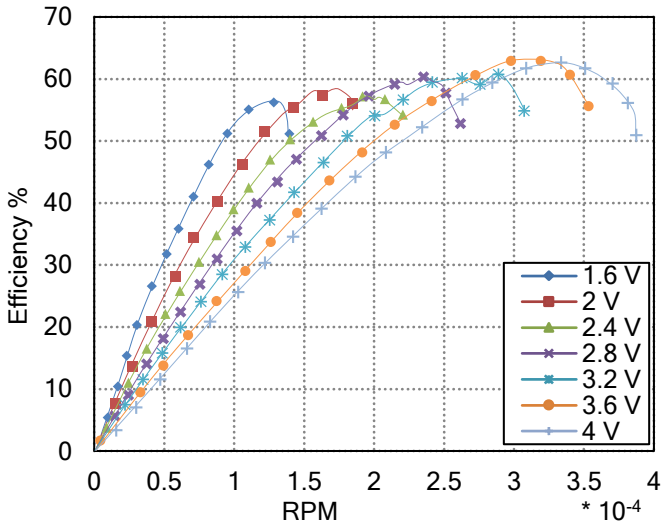

Figure 4.5: Efficiency vs RPM for SS-1.7 Brushed Motor (adapted from Harrington[54])

"no-load side" of the curve is characterized by low torque and high RPM while the "stall side" is characterized by low RPM and high torque[54]. It is evident from Figure 4.4 and Figure 4.5 that the SS-1.7 brushed motor, is most efficient in high-RPM, low-

torque applications. Furthermore, this same characteristic was observed all brushed motors, including the SS-2.3 and SS-3.3, in the Harrington, Kroninger study[54]. The SS-1.7, 2.3, and 3.3 (where the number designates the average internal resistance of the motor in Ohms) yielded the highest overall brushed motor performance in the study, and thus were selected for further optimization testing.

Brushless motors were shown to require different operating parameters compared to brushed motors for maximum efficiency. While both types of motors operate most efficiently at high rotational speeds, brushless motors also require a higher torque to operate more efficiently[54]. Figure 4.6 is a representation of this characteristic for the AP03-4000 brushless motor. It shows brushless motor efficiency as a function of torque and RPM. It is important to note that peak efficiency for the AP03-4000 occurs at a large value of torque (1.5m N-m) and high rotational speed ($1.75x10^4$ RPM).

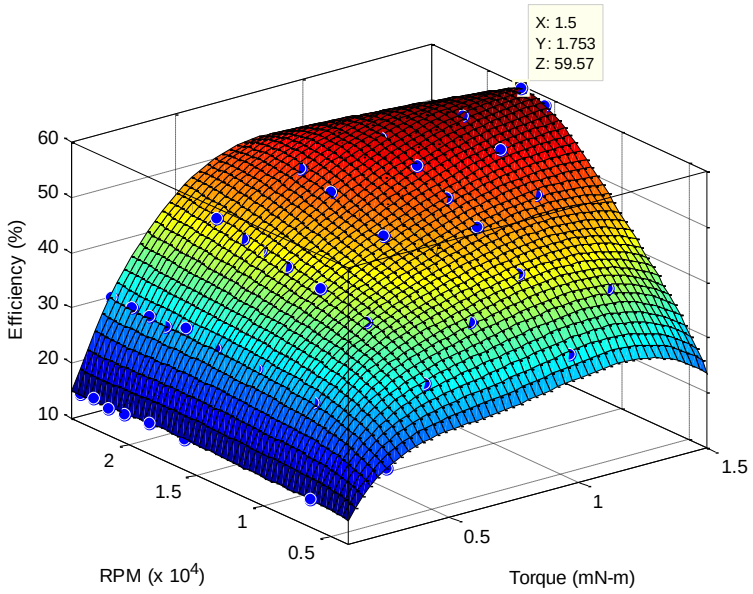

Figure 4.6: Efficiency as a Function of Torque and RPM for an AP03-4000 motor (adapted from Harrington[54])

Furthermore, this trend was generally observed in all other brushless motors in the Harrington-Kroninger study[54]. The AP03-4000 and AP03-7000 were concluded to have the best brushless performance characteristics while still being lightweight (<4g). For these reasons, the performance of the AP03-4000 and AP03-7000 were evaluated with the addition of a speed controller.

As stated previously, brushless motors require an electronic speed controller (ESC) to alternatively phase the voltage and current to the motor windings to rotate the motor shaft. This electronic phase shifting is a complicated process that incurs its own power usage which results in a lower effective efficiency for brushless motors[54]. This effect is evident in Figure 4.7 in which the speed controller efficiency drops as the torque is increased. This results in a decrease in maximum efficiency between 10-20% for brushless motor systems, essentially negating any benefits over brushed motors.

Unlike brushless motors, brushed motors can vary rotational speed simply by changing the supplied voltage. However, in a practical MAV application where a battery is used, the voltage supplied to each motor cannot be directly changed. Instead, brushed ESCs can be used to rapidly switch the current to the motor on and off with a pulse width modulated signal. This effectively decreases the power supplied to the motor proportional to the pulse width. This is a much simpler process than compared to the brushless ESC's and does not incur as much power loss. To confirm this, experimental studies were carried out with the SS-3.3 brushed motor and a 3A single cell brushed ESC. These results, shown in Figure 4.8, were compared with the brushless results from the Harrington-Kroninger study. Though this motor was operating under

similar conditions as the AP03-7000, the efficiency loss is much less. In particular, both isolated motors are operating at approximately 55% efficiency at 1.5 mN-m of

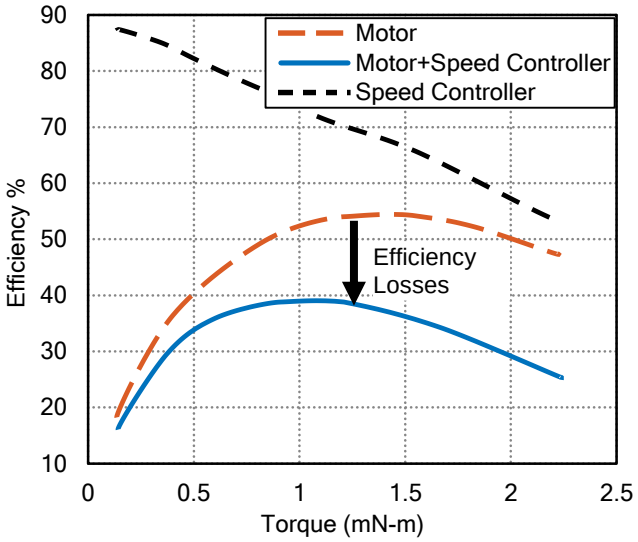

Figure 4.7: Efficiency Loss for the AP03-7000 Brushless Motor with a Castle Creations Phoenix 6 ESC (adapted from Harrington[54])

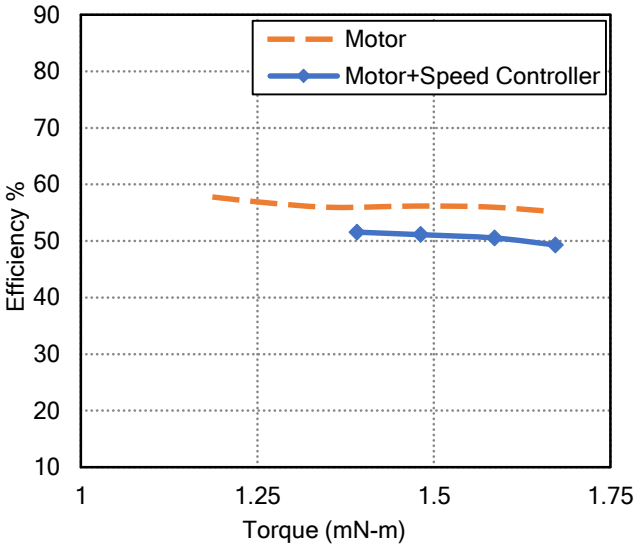

Figure 4.8: Efficiency Loss for the SS-3.3 Brushed Motor with a HobbyKing 3A Single Cell ESC

torque. But when ESC power consumption is accounted for, efficiency dropped 18% for the brushless system and only 5% for the brushed system. This same trend was observed with the AP03-4000, SS-1.7 and SS-2.3 motors as well.

Since it is known that maximum motor efficiency is dependent on specific torque and RPM combinations[54], a transmission can be implemented to achieve the optimal combination. This can be a simple two-gear transmission between the motor shaft and rotor. In a direct drive application (i.e. gear ratio 1:1) the RPM and torque of the rotor is same as the motor's. But with a higher gear ratio (i.e. 4:1), the rotor will operate at a higher torque but lower RPM compared to the motor. Ideally, the optimal gear ratio will allow the motor to operate at its maximum efficiency point while rotor still provides the required thrust.

A gearbox will not substantially increase brushless motor performance given the inversely proportional relationship between torque and RPM depending on the gear ratio. It is known from Figure 4.6 that brushless motors require both high RPM and torque for maximum efficiency. This is best achieved with a direct drive motor-rotor coupling since gear ratios would trade-off torque for RPM or vice versa. However, it was shown in Figure 4.4 that brushed motors operate most efficiently at low torque and high RPM, which is the ideal scenario for a gearbox.

Tests were conducted to determine if geared, brushed motors confirmed increased performance over direct drive brushless motors. SS-1.7, SS-2.3, and SS-3.3 motors were tested with gear ratios between 2:1 and 7:1 and compared against the AP03-4000 brushless motor. The optimized rotor was used in each test to produce 10-

20 g of thrust (~1/4 the thrust needed for a 40-80g quadrotor). As an example, the results from the SS-3.3 brushed motor with 4:1 gear ratio are compared with the AP03-4000 in Figure 4.9. This confirms that the geared brushed motor can produce the same amount of thrust much more efficiently than the brushless motor.

The findings from Harrington and Kroninger have been utilized as a base for further motor optimization studies. It was known that the AP03-4000, AP03-7000, SS-1.7, SS-2.3, and SS-3.3 motors represent the best performance characteristics of small brushless and brushed motors[54]. It was also known that brushed motors operate most efficiently at low torque and high RPM while brushless motors operate most efficiently at high torque and high RPM[54]. Based on the present experimental studies it was determined that ESCs have a more pronounced effect on power losses for the brushless motors than the brushed motors. It was also determined that geared transmissions are

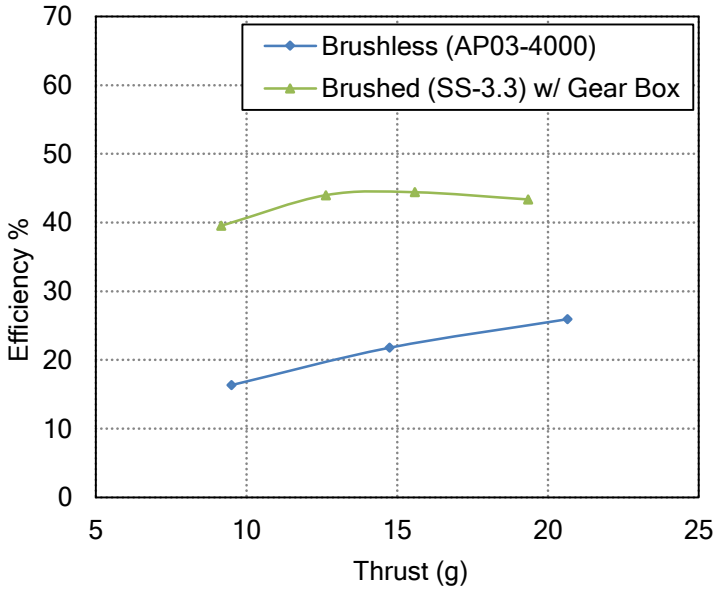

Figure 4.9: Efficiency Comparison between a Direct Drive Brushless Motor and a Brushed Motor with 4:1 Gear Ratio

able to provide substantial performance boosts for brushed motor systems. For these reasons, only the SS-1.7, SS-2.3, and SS-3.3 brushed motors were considered in more extensive optimization studies.

4.2 Coupled Motor-Rotor Experiments

Maximizing the flight endurance of a micro quadrotor requires optimizing the coupling of the optimized rotor with the brushed motor through a power transmission system. While the SS brushed motors were shown to have the highest efficiency with relatively small ESC losses, it was still unknown how this would translate into quadrotor flight endurance. To determine this, two important performance metrics were established: (1) electric power loading (EPL) and (2) and thrust available at an applied voltage (thrust/volt). EPL is another representation for efficiency of the power system. It is simply the thrust produced by the rotor over the electrical power consumption needed to generate that thrust. A higher EPL indicates a higher efficiency of the propulsion system. However, the most efficient systems may not be able to generate the necessary thrust for flight. This is why the second metric was established. A successful, hovering quadrotor must be able to maintain a minimum thrust/volt depending on its gross weight and available battery voltage. Since it was determined that SS brushed motors would be used in the vehicle design, their weights (approximately 2.75g) were factored into the gross weight for a more accurate estimation of 48g. This requires that each motor-rotor pair can supply a minimum of

12g of thrust with the available battery voltage (typically 3.6 – 4.2V for Lithium-Polymer).

To determine the highest performance power transmission system, the optimized rotor was paired with each SS brushed motor via gear ratios (GR) ranging from 2:1 to 7:1, for a total of 21 tested transmission configurations. Each configuration was tested on thrust measurement stand, and the input power was controlled through a power supply. Each configuration was tested over a voltage range which provided 8 – 18 g of thrust since this would be the typical operational range for a micro quadrotor. A summary of results from power transmission configurations are displayed in Figure 4.10 to Figure 4.15 in terms of EPL and thrust/volt.

The EPL as a function of thrust for the SS-3.3 motor is displayed in Figure 4.10. In this chart it is evident that, in general, EPL increases as the gear ratio increases for a

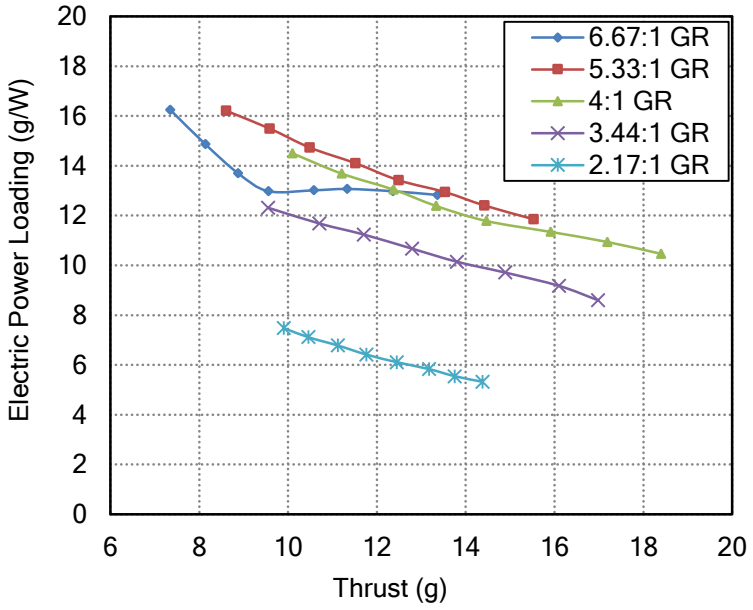

Figure 4.10: Electric Power Loading vs. Thrust; SS-3.3 Motor, varying Gear Ratio

given thrust. However, beyond a gear ratio of 5.33:1 the EPL starts dropping. From this perspective, it appears that a gear ratio of 5.33 would yield the highest vehicle flight endurance. However, increasing the gear ratio also has the adverse effect of decreasing the RPM of the rotor relative to the motor shaft. This results in a decrease in thrust for the same voltage, as seen in Figure 4.11. It is evident in this plot that the 5.33:1 gear ratio may not be able to supply the necessary thrust (12g) at low voltages despite being the most efficient.

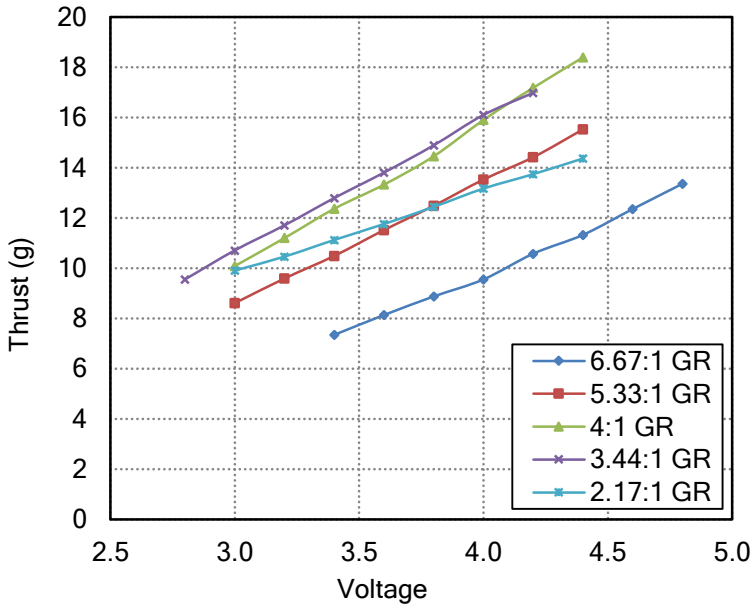

Figure 4.11: Thrust vs. Voltage; SS-3.3 Motor, varying Gear Ratio

Similar tests completed with SS-2.3 and SS-1.7 motors yielded similar trends as the SS-3.3 tests. Again, higher gear ratios tend to increase EPL while decreasing thrust/volt. However, the major difference with the SS-2.3 and SS-1.7 motors is that they can achieve the same thrust levels as the SS-3.3 but at much lower voltages (2 – 3.5V). Therefore, with a typical single cell battery supplying 3.6 – 4.2V (detailed in the

next section), these motors will be able to supply more thrust compared to the SS-3.3. However, it was also observed that they will be less efficient at higher voltages.

To better compare the overall propulsion system characteristics relative to each other, the best performing gear ratio for each motor was obtained. These were the combinations which provided the highest EPL while maintaining more than 12g of thrust for 3.6 – 4.2V. The EPL and thrust of these optimal combinations are re-plotted on Figure 4.12 and Figure 4.13 respectively. With these charts, it is more evident that the SS-3.3 is the most efficient while still providing adequate thrust for a given voltage.

The efficiency loss from the SS-1.7 and SS-2.3 motors outweighs the benefit from the large excess thrust they can provide. For this reason, the SS-3.3 motor with a 4:1 gear ratio was chosen for the preliminary vehicle design iteration.

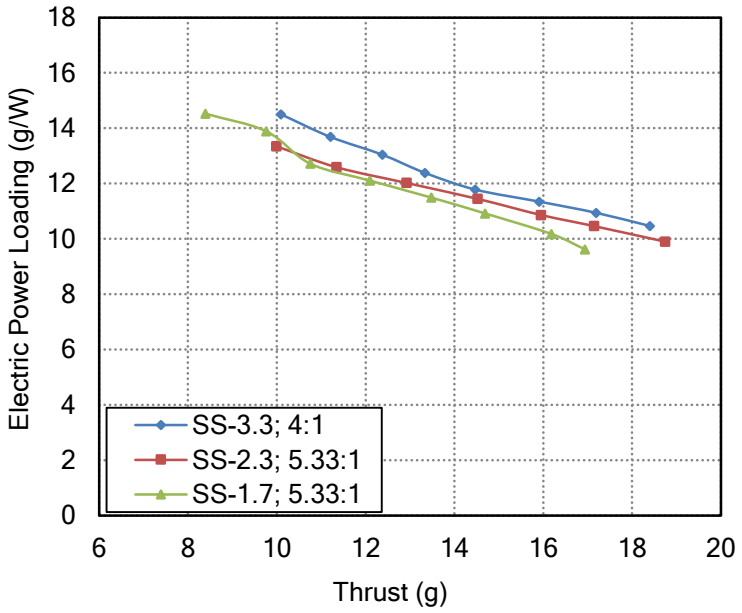

Figure 4.12: EPL vs. Thrust for Optimal Motor and Gear Ratio Combinations

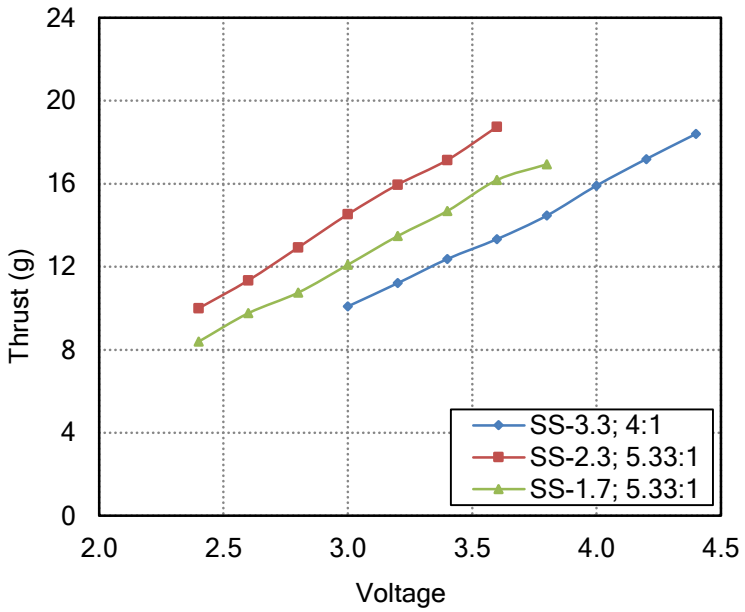

Figure 4.13: Thrust vs. Voltage for Optimal Motor and Gear Ratio Combinations

Initial flight tests of the preliminary vehicle design iteration showed that the quadrotor would quickly reach a point where no more excess thrust could be produced. Thus, controllability was difficulty to maintain with little excess power. This was due to battery voltage drop off, which will be investigated in the next section. Rather than compromising overall flight endurance by using SS-1.7 and SS-2.3 motors for excess thrust, the optimized rotor diameter was increased from 90 mm to 110 mm for improved power loading. The final power transmission optimization tests were completed with the larger diameter rotor. This involved iteratively varying the collective pitch of the rotor blades between 11.5^{o} and 17.5^{o} and systematically testing each pitch with the 4:1 and 5.33:1 gear ratios. Two highest performance results from these experiments relative to the previous optimized transmission (15.5° collective, 4:1 GR, dia.=90 mm) are

shown in Figure 4.14 and Figure 4.15. It was generally observed from these tests that the lower collective pitches increased EPL while decreasing thrust/volt. In particular, it was concluded from these experiments that new power transmission should utilize 13.5^{o} collective pitch in the optimized rotor, a SS-3.3 brushed motor, and a 5.33:1 gear ratio to improve EPL without compromising thrust/volt. Alternatively, utilizing a 4:1 gear ratio would improve excess thrust/volt without compromising EPL.

4.3 Battery Discharge Tests

To keep the mass of the micro quadrotor below 50 g, a lightweight, high energy density power source is required. While many types of batteries exist, including Nickel-Cadmium, Nickel-Metal Hydride, and Lead-Acid, the heavy metals used in these batteries contribute too much weight to be feasibly incorporated in the current quadrotor design[56]. Another battery type known as Lithium-Ion-Polymer (Li-poly) utilizes lightweight lithium and polymers to achieve a large electrochemical potential, and therefore some of the best energy densities. Li-poly batteries can have 2-3 times the gravimetric energy density of standard, heavy metal batteries. Therefore, only Li-poly batteries were examined for use on the micro quadrotor.

As stated in the previous section, batteries do not maintain a constant voltage as they are discharged. Rather, the battery voltage drops steadily as the available charge is drained till it reaches an effective cutoff point. For 3.7V rated Li-poly batteries, this is approximately 3.6V. This battery discharge characteristic was studied with the use of a Computerized Battery Analyzer (CBA). Batteries were tested by discharging at a

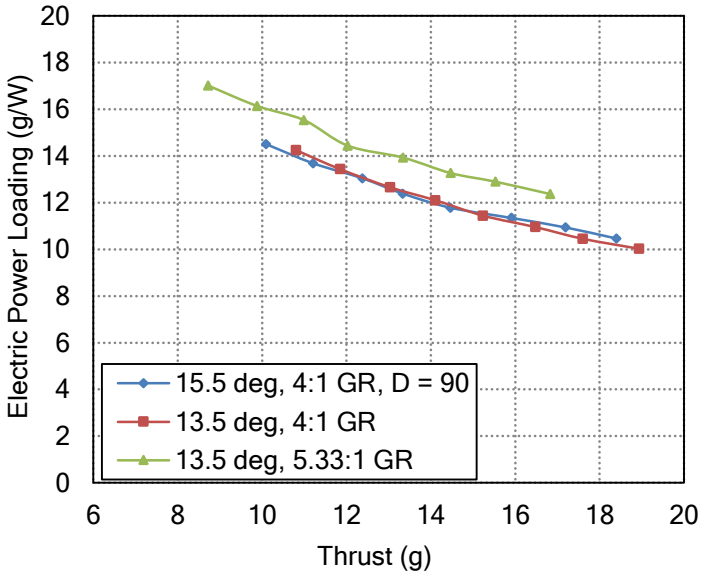

Figure 4.14: SS-3.3 Motor; Electric Power Loading vs. Voltage for Multiple Pitch and Gear Ratio Combinations

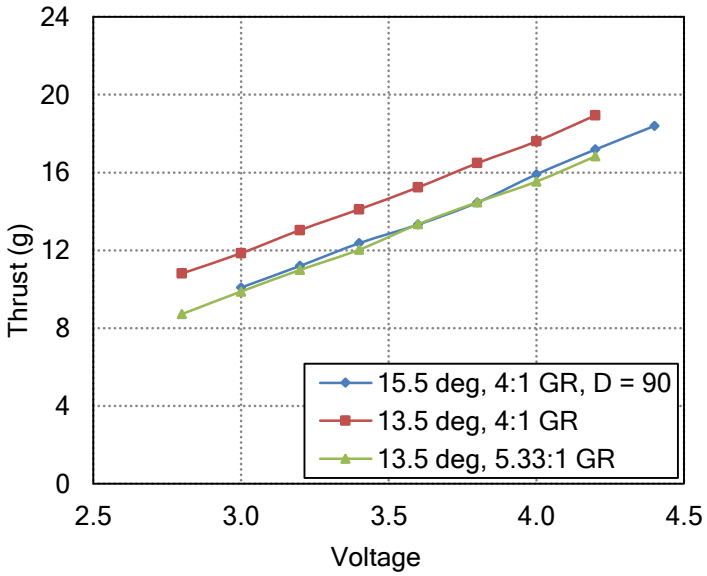

Figure 4.15: SS-3.3 Motor; Thrust vs. Voltage for Multiple Pitch and Gear Ratio Combinations (110 mm Dia.)

constant current draw and recording the battery voltage over time with the CBA. Results from the power transmission studies showed each motor would draw approximately 0.3 A, so it was initially estimated that the quadrotor would draw approximately 1.2 Amps. Therefore, this was the current draw used in the initial battery tests. Batteries of various capacities, manufacturers, and geometries examined to determine which had the best overall characteristics. Batteries are designated by [manufacturer initial]_[capacity in milliamp-hours]_[geometry: Rectangular or Cylindrical]. The results of the tests are shown in Figures 4.16 - 4.18.

It is immediately evident in Figure 4.16 that battery endurance is most directly affected by the rated capacity. This is to be expected as a larger capacity battery will be able to supply the same power for a longer period of time. It was also noticed that the batteries may not maintain the same voltage levels relative to each at the same percent capacity remaining. To make this clearer, the data from Figure 4.16 was normalized by each battery's final time to discharge completely to obtain the voltage level as a function of normalized time. This normalized data is displayed in Figure 4.17. This chart shows that the voltage characteristics are heavily dependent on battery geometry. Though each battery has the same rated voltage (3.7V), it is evident in Figure 4.17 that the two high capacity rectangular batteries (T_950mAh_R and T_750mAh_R) maintain a 0.5 – 1 V higher voltage over the two cylindrical batteries (T_900mAh_C and T_650mAh_C). From a controls perspective, the rectangular batteries may be preferred, as the increased voltage means the rotors would be able to

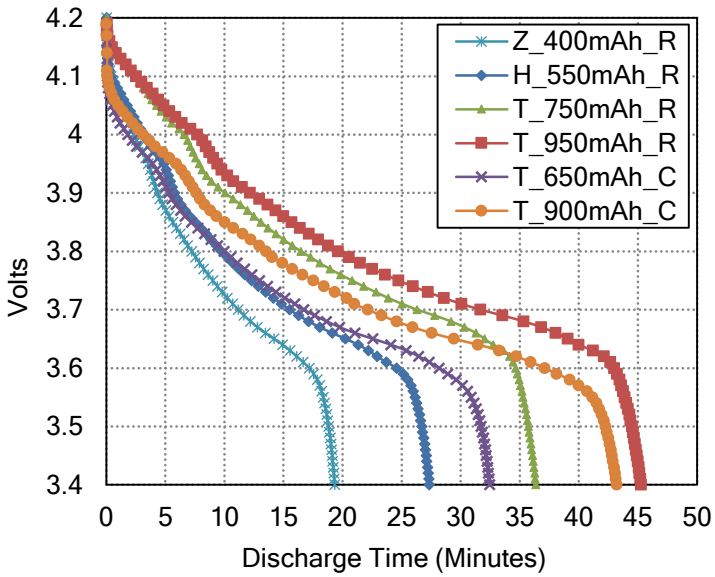

Figure 4.16: Battery Voltage Available Over Time under 1.2 Amp Current Draw

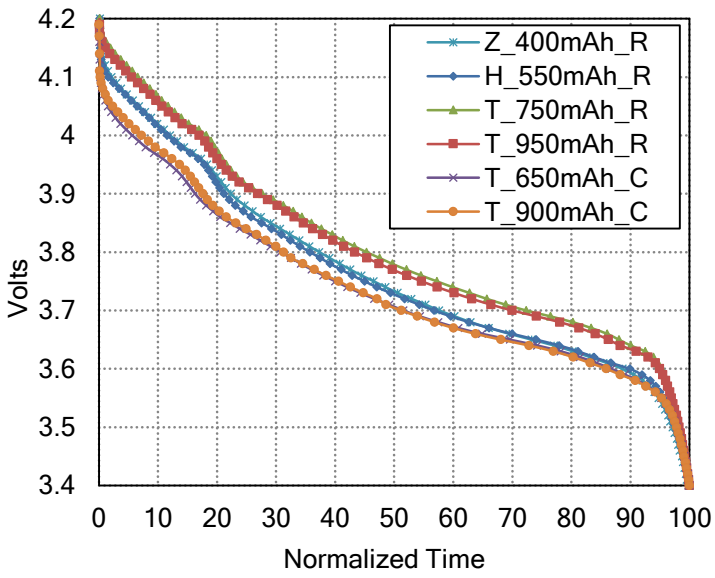

Figure 4.17: Battery Voltage Available as a Function of Normalized Time

supply more excess thrust. The excess thrust would enhance control authority, as faster roll, pitch, and yaw rates could be achieved with more thrust input to the rotors.

However, excess voltage is not as beneficial from a flight endurance perspective. In the hover scenario, the large excess voltage at the beginning of discharge will not be utilized. The speed controllers will regulate the voltage to each rotor via a pulse width modulation signal to supply only the power necessary for hover. Hence, only the minimal voltage needed for sustained hover thrust is required from the battery. The results from the voltage studies in Figure 4.17 confirm that the lowest effective voltage supplied is approximately the same for all batteries (3.6V). Thus, the weight of the battery becomes a bigger factor than lowest effective voltage for hover endurance. As the battery capacity increases so does the weight. Thus, the higher capacity batteries will also require a larger current draw and may not actually produce the largest endurance. A more direct relation between battery weight and endurance was required.

Determining an estimated current draw for each battery required an estimation of the final quadrotor weight. Since the rotors, gears, motors, ESCs, and processor-sensor board to be used were already known from previous studies, an accurate empty weight for the vehicle was estimated at 31.5g. By adding the individual battery weight, and dividing by 4, an accurate estimation of individual rotor thrust could be obtained. By interpolating measured current and thrust data from the power transmission studies, an approximate value of total current draw in hover could be obtained. Each battery was then discharged at its specific current draw for the most accurate prediction of

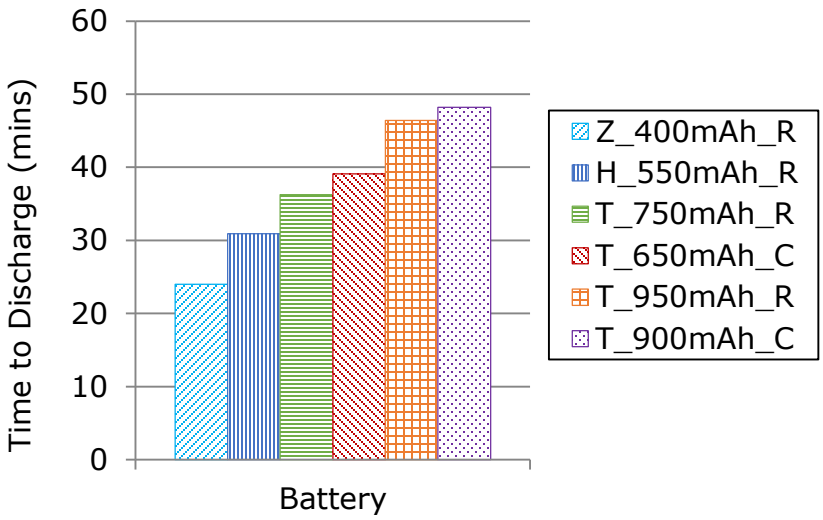

Figure 4.18: Each Battery's Time to Completely Discharge Under Individual Current Draw

hover endurance. The results of this study, displayed in Figure 4.18, indicate battery endurance is dependent on rated capacity as well as battery geometry. Specifically, the two cylindrical batteries have a longer discharge time for their capacity as opposed to the rectangular batteries. This could be due to a more efficient use of cathode/anode surface area within the volume of the battery. Though, more in-depth analysis is required to determine exactly why this is the case. Though the T_950mAh_R battery showed the second highest predicted endurance, it was rejected as a viable option since it caused the quadrotor to weigh more than the desired 50g. Ultimately, only the two cylindrical batteries were chosen for further testing in the full vehicle design. The T_650mAh_C weighs 12.75g and the T_900mAh_C weighs 17g.

4.4 Onboard Avionics and Telemetry

To control and stabilize the quadrotor during flight, a high-bandwidth attitude feedback control is required. This was implemented on the vehicle with a (2 g) processor-sensor board (U.C.Berkeley GINA2.2 board[57]). The board contains integrated ITG3200 tri-axial gyros and a KXSD9 tri-axial accelerometer for attitude measurement and a TI MSP430 microprocessor for feedback controller computation. The inner-loop feedback signals are updated at a 3 ms rate[58]. Wireless communication was provided with an onboard Atmel radio and antenna with a 20–30 ms latency. A pilot controls the quadrotor through a telemetry setup with a LabVIEW interface on a base station. The base station utilizes a 2.4 GHz Atmel AVR transceiver for wireless communication (IEEE 802.15.4 protocol) with the quadrotor. With this communication setup, feedback gains, trim inputs, and pilot commands can be updated in flight[58].

4.5 Stability and Control Architechture

A proportional–derivative (PD) controller serves as the core of the onboard inner feedback loop as shown in Figure 4.19. The inputs to the PD controller are the pitch and roll Euler angles (θ, ϕ) and the pitch q, roll p, and yaw r attitude rates. These attitude rates are measured by the gyros on the processor-sensor board. The gyro measurements are integrated over time to extract the quadrotor Euler angles. However, this integration method causes drift in attitude measurements over time[59]. Therefore, measurements from the accelerometers, which record the tilt of the gravity vector, were

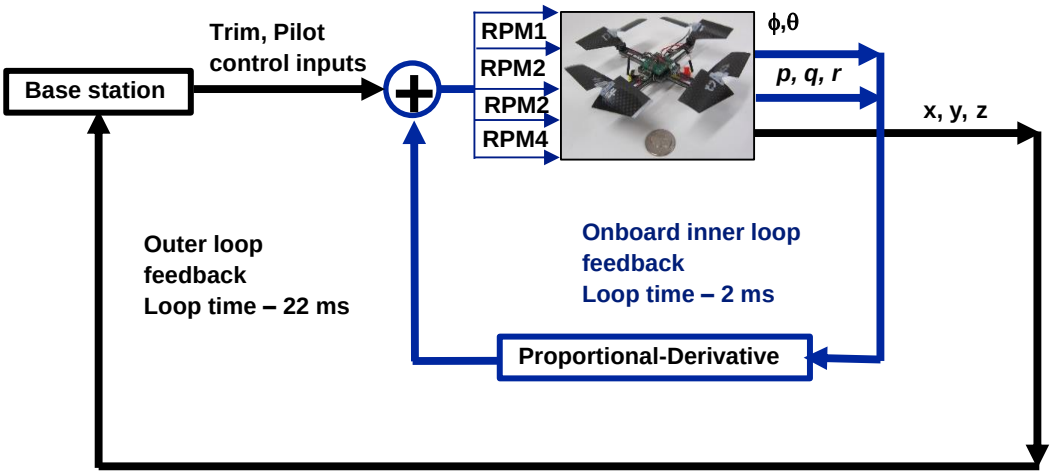

Figure 4.19: Schematic of the Stability and Control Architecture

also used in the controller. Accelerometer measurements, are less susceptible to drift but can be corrupted by high-frequency vibrations[60]. Therefore, a low-pass filter (6 Hz cutoff) was applied to the accelerometers and a high-pass filter (4 Hz cutoff) was applied to the gyros to extract the attitude. A human pilot controls the quadrotor via the outer-loop. The processor sensor board outputs RPM signals to the rotors to control the vehicle.

4.6 Airframe Fabrication and General Configuration

The final component needed to construct the optimized quadrotor was an ultra-lightweight, structural airframe to hold the other components (motors, battery, and processor-sensor board). It was crucial that the airframe minimized the gross weight of the vehicle while still maintaining durability. For this reason, the airframe was chosen to be milled out of a high strength-to-weight carbon fiber-balsa wood composite sheet.

With 1.5mm thick connecting spars, the airframe weight is only 3.3g. The general quadrotor configuration with all components integrated into the airframe is shown in Figure 4.20. To understand the significance of the airframe weight reduction, the weight of each component was compared with a representative sample of similarly sized commercial off-the-shelf (COTS) quadrotors. As seen in Figure 4.21 the airframe weight of the optimized quadrotor takes up 23 - 43% less of the total vehicle weight compared to other models.

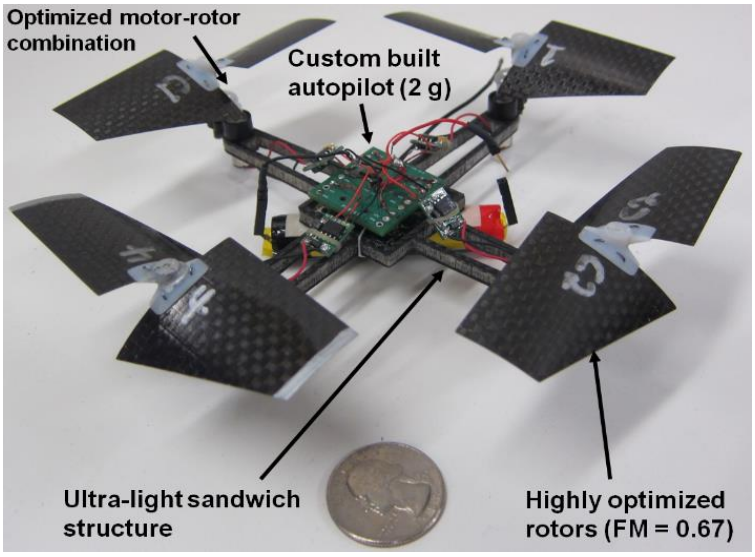

Figure 4.20: Micro-Quadrotor Configuration

4.7 Gimbal Testing

Before flight testing the quadrotor for endurance in free hover, gimbal tests were conducted with the use of the setup pictured in Figure 4.22. An isolation mount supported the quadrotor on a thrust measurement balance. The quadrotor was

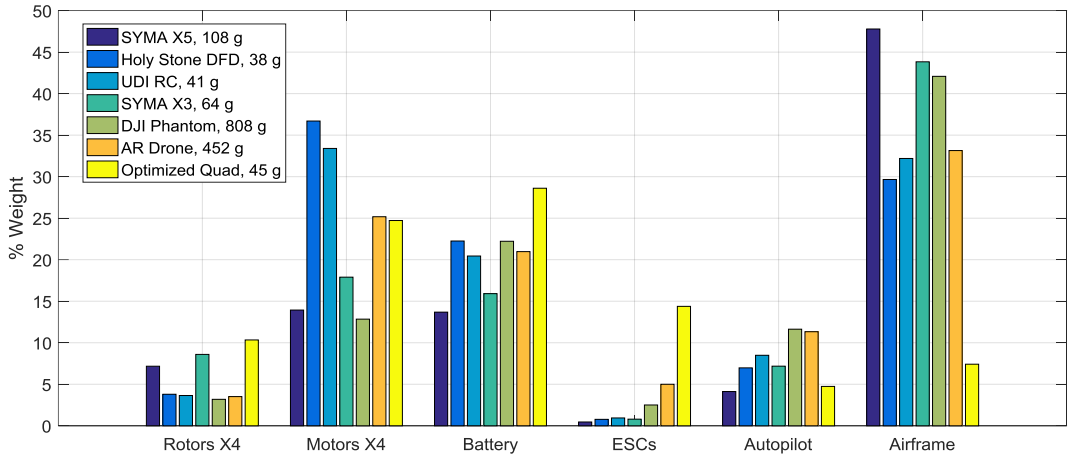

Figure 4.21: Comparison of the Optimized Quadrotor Component Weight % with a Representative Sample of Commercial Quadrotors Micro-Quadrotor Configuration

connected to the mount via a gimbal bearing. The gimbal setup mimics free hover since it allows the quadrotor to yaw, pitch, and roll freely, but constrains it in translational motion. In this way, the quadrotor must expend energy to offset its weight as well as to stabilize itself as it would in a hover scenario. The quadrotor thrust was monitored on the balance to determine when it could no longer offset its own weight on a single battery charge. The purpose of the gimbal tests was to determine which final configuration would be suitable for free hover testing. Two optimal gear ratios and two high energy density batteries were tested to determine which configuration should yield the highest endurance. The results of the gimbal experiment are shown in Table 2. These results show that for either gear ratio, the T_900mAh_C battery will yield a higher predicted endurance, and for either battery, the 5.33:1 gear ratio will yield a higher endurance. This is likely due to the higher energy density of the 900mAh battery

and the higher EPL of the 5.33:1 gear ratio. Furthermore, these tests validated the battery discharge tests since the two endurance values for the 5.33:1 GR match the corresponding battery discharge times in Figure 4.18 within ± 2 minutes.

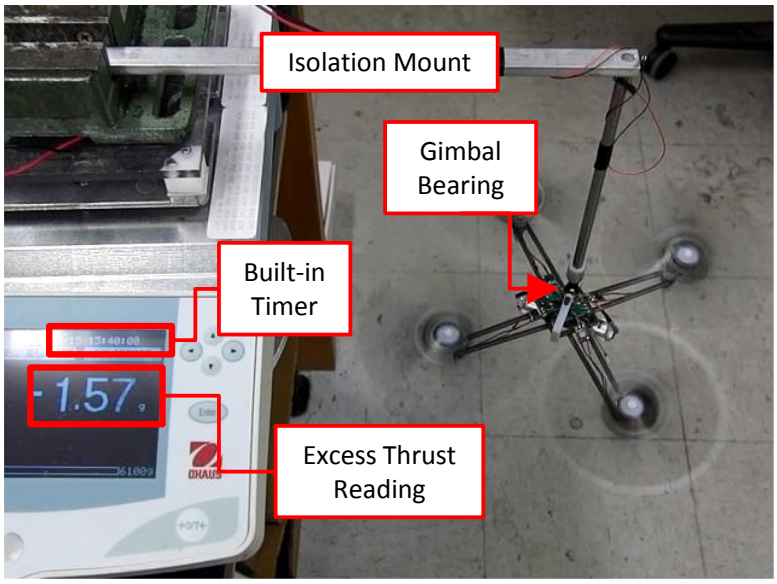

Figure 4.22: Gimbal Testing Setup

Table 2. Gimbal Test Endurance Times

Gear Ratio	Collective Pitch	Battery	Gross Weight (g)	Endurance (minutes)
4:1	13.5º	650 mAh	44.44	32
4:1	13.5º	900 mAh	48.8	37
5.33:1	13.5º	650 mAh	44.13	40.5
5.33:1	13.5º	900 mAh	48.5	49

4.8 Free Flight Hover Testing

The final quadrotor configuration used the SS-3.3 motor with a 5.33:1 gear ratio since this was determined to yield the highest predicted endurance by the gimbal tests. Both the T_650mAh_C and T_900mAh_R battery were tested. Free hover tests were conducted by a human pilot within a 20 ft^3 testing area pictured in Figure 4.23. Hover endurance was measured from the time the quadrotor took off to the time it could no longer stabilize itself and support its own weight in one continuous flight. While the gimbal tests predicted that the 900mAh battery would provide the largest endurance, this was difficult to confirm in free hover since this quadrotor configuration became less controllable as the battery discharged. It is likely the added weight changes the dynamics of the system in a way that must be accounted for in the control algorithm.

Figure 4.23: Optimized Quadrotor in Free Hover[1]

[1] Video available at: https://www.youtube.com/watch?v=TA8B_o3ZvCs

When equipped with the T_650mAh_C battery, the quadrotor maintained controlled hover for 31 minutes. However, this has the potential to be improved, as it is still below the endurance predicted by the gimbal and battery discharge tests. It was observed in the flight tests that the control authority and stability characteristics diminish as the battery is discharged. This indicates that the magnitude of control inputs varies significantly as the battery is discharging. To mitigate this, the differential gains in the PD feedback control loop were increased to be nominally higher than gains required for hover flight under a full battery charge. An area of improvement could be an adaptive gain scheme such that the flight characteristics remain the same throughout the duration of battery discharge, thus improving controllability and reducing pilot workload. The final weight breakdown of the optimized quadrotor design is shown in Table 3.

Table 3. Micro-Quadrotor Weight Breakdown

Component	**Weight (g)**	**% Weight**
Controllers and Wires	8.51	19.12
SS-3.3 Motors	11	24.72
650mAh Battery	12.73	28.61
Rotors	4.6	10.34
Gear Transmissions	4.36	9.80
Airframe	3.3	7.42
Total	44.5	

4.9 Quadrotor Prototype Conclusions

The present research has focused on designing and optimizing a MAV-scale quadrotor helicopter for maximum hover endurance. This has been achieved through systematic testing of each component, including the motors, gear transmission systems, and battery, as well as significantly reducing the airframe weight of the quadrotor. Optimization studies of the quadrotor subsystems yielded the following results:

1. Brushed motors are more suitable than brushless motors for use on an MAV-scale quadrotor. Brushless motors and electronic speed controllers (ESCs) are heavier than brushed motors and brushed ESCs. It was determined that ESCs have a much more pronounced decrease in efficiency in brushless motor systems than in brushed motor systems. It was also determined that geared transmissions are able to provide substantial performance boosts for brushed motor systems but only marginally effect brushless motors. The fundamental reason for this is the fact that brushed motors perform better at high rpms and low torque while brushless motors have higher efficiencies at both high rpm and high torque, which cannot be achieved by a gearbox. For these reasons, the three most efficient brushed motors were considered in more extensive optimization studies.

2. Identically sized brushed motors with different internal resistances will exhibit different power loading and thrust/volt characteristics. High resistance brushed

motors (3.3 Ohms) exhibit higher electrical power loading and lower thrust/volt compared to lower resistance motors (1.7 and 2.3 Ohms).

3. Pairing brushed motors with larger gear ratios has the effect of improving electric power loading while reducing thrust/volt. Smaller gear ratios decrease EPL while increasing thrust/volt. For the same gear ratio, high resistance brushed motors had higher EPL than low resistance motors but produced less thrust/volt. Brushed motors with 4:1 and 5.33:1 gear ratios had the highest overall efficiency while still being able to supply the minimum thrust/volt for controlled flight.

4. Li-poly Battery voltage does not remain constant as it is discharged. The amount of voltage drop is dependent on battery geometry. Rectangular batteries show less voltage drop than cylindrical batteries. The lowest sustainable voltage for 3.7V rated Li-poly batteries is effectively 3.6V. Energy density is also dependent on battery geometry. Cylindrical batteries have longer endurance for their mass than rectangular batteries at the required current draw. Due to this characteristic, the 650mAh and 900mAh cylindrical batteries were studied in the full vehicle configuration.

5. Vehicle control and stability were provided by a lightweight (2g) processor-sensor board (GINA-Mote). A telemetry setup with a base station was used to wirelessly update the feedback gains, trim inputs, and pilot commands to the vehicle in flight.

6. The quadrotor airframe was fabricated from an ultra-lightweight carbon fiber-balsa wood composite for significant weight reduction. This comprises only 7.4% of the optimized quadrotor gross weight compared to 30 - 50% for other similarly sized COTS quadrotors.

7. The highest predicted endurance times on the gimbal test setup were achieved with the 5.33:1 gear ratio. The 650mAh and 900mAh batteries resulted in endurances of 40.5 minutes and 49 minutes, respectively, during gimbal testing. . In free hover flight tests, the maximum hover endurance achieved with the 650mAh battery was 31 minutes, which is almost double the hover endurance of any of the existing MAV-scale helicopters.

Chapter 5: Quadrotor Sizing Design Program

This chapter describes the development and application of a design methodology for small-scale rotary-wing MAVs. First, the primary quadrotor component groups are identified and the empirical trends which drive their weights are presented. These trends have been quantified and organized in multivariable regression equations. The means of calculating and validating rotor power in hover and forward flight are also included. Finally, the schematic of the complete sizing algorithm and validation of its results is presented.

5.1 Quadrotor Components and Weight Trends

The following section describes the general quadrotor component groups in order of sizing consideration: rotors, motors, electronic speed controllers (ESCs), batteries, and airframe. The general layout of these components is shown in Figure 5.1. Additionally, data is presented from measurements and manufacturer specifications, which shows evidence of correlation between component weight and key design parameters (e.g. rotor radius, power output, and energy storage). Figure 5.2 provides the general range of quadrotor gross takeoff weights (GTOW) and disk loadings (GTOW/total rotor area) for which the present study is valid. The symbols in Figure 5.2 represent quadrotors which have been disassembled and weighed for the current study.

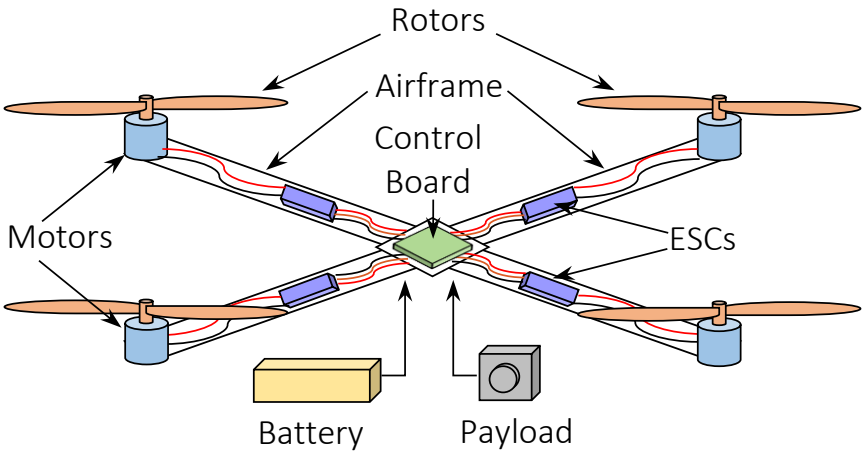

Figure 5.1: General quadrotor schematic

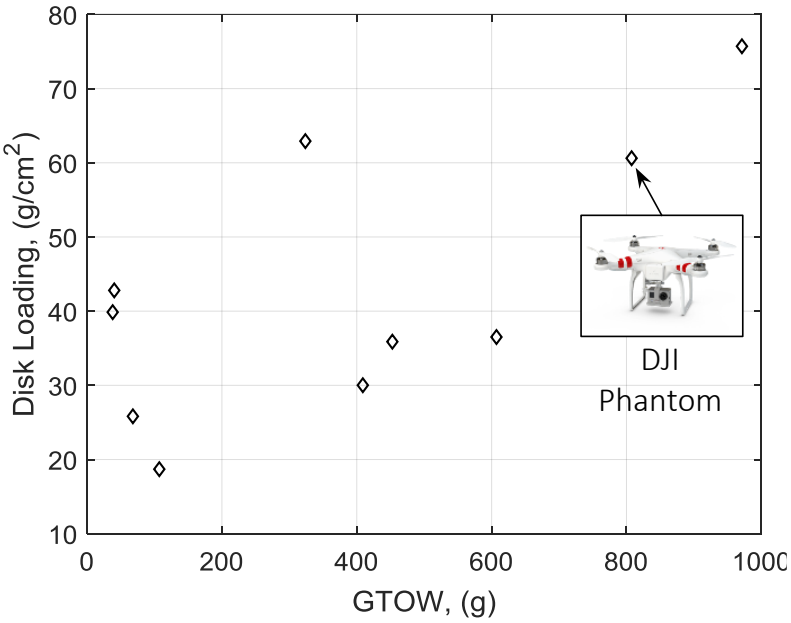

Figure 5.2: Typical small-scale commercial quadrotor disk loading vs. GTOW

5.1.1 Rotors

An aerodynamic analysis of rotors will yield approximate rotor design parameters for a required disk loading, range, and endurance objective. Since these design parameters, such as radius, blade area, and number of blades, influence rotor weight they can be correlated to rotor mass as shown in Figure 5.3.

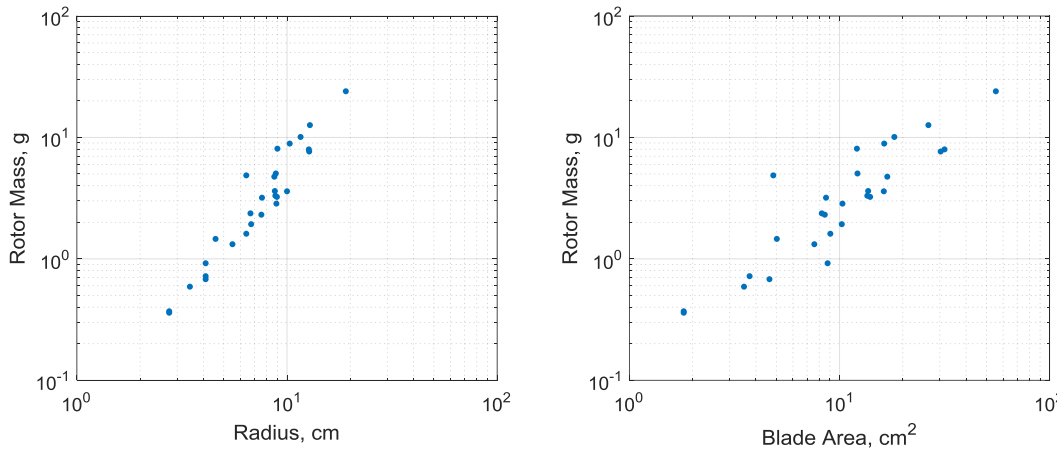

Figure 5.3: Plots of rotor data (log scale) showing correlation between rotor mass, radius, and blade area

Figure 5.3 represents a sampling of polystyrene molded and carbon fiber rotors with various radii, solidity and number of blades. These trends show that for a variety of micro-rotors, radius and blade solidity are key sizing parameters.

5.1.2 Motors

There are two types of electric DC motors commonly used in quadrotor MAVs: brushless (BLDC) motors and brushed motors. For the majority of larger quadrotors (>100 g, GTOW), brushless motors tend to be the more popular choice. This is mainly because their operating principle keeps internal friction low and efficiency high. In BLDC motors, the stator is composed of wire coils to induce magnetic fields while the rotor holds permanent magnets. Since the polarity of the stator coils is phased electronically, metal brushes are not needed to mechanically phase current, thereby reducing friction[61].

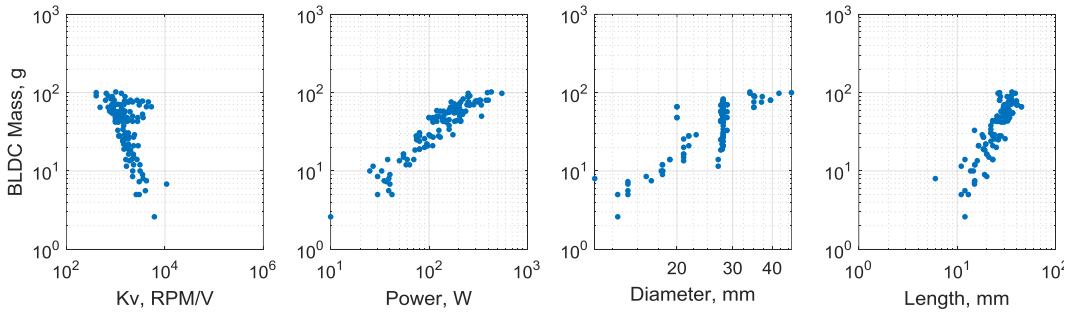

Figure 5.4: Plots of brushless DC motor data (log scale) showing strong correlation between BLDC mass, K_v, max rated power, casing diameter, and casing length

A defining parameter of BLDC motors is the K_v value, which is the no-load speed constant of the motor in units of RPM/V. K_v describes how fast the motor will spin without applied torque when a certain voltage is supplied. For example, a 1000 K_v motor will spin at 1000 RPM when 1V is applied and 2000 RPM when 2V is applied. An optimum propulsion design will utilize a motor with a K_v just large enough to

achieve maximum required RPM[43]. Figure 5.4 shows how BLDC motor weight is affected by K_v as well as the motor's max rated power, outer diameter, and casing length. Data published online for these motors has been collected from established motor manufacturers such as Turnigy, ProTronik, NeuMotors, and Portescap.

The second type of electric motor is the brushed motor, which is typically used for quadrotors <100 g GTOW. At this scale, previous studies have shown that brushed motors yield higher efficiencies than BLDC counterparts[61]. Also, the simple construction of brushed motors allows them to be lighter. The electronic speed controller, described in the next section, also tends to be lighter for brushed motor systems. Figure 5.5 shows that for a brushed motor, its mass is largely related to its maximum output power and torque, casing diameter, and casing length.

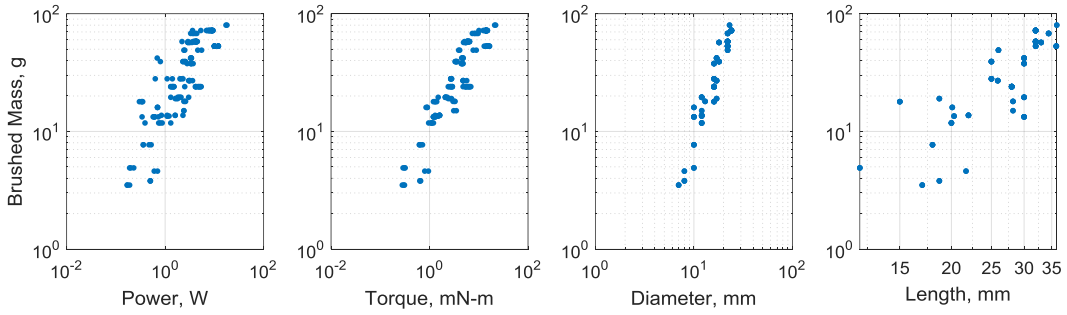

Figure 5.5: Plots of brushed motor data (log scale) showing strong correlation between motor mass, power, max continuous torque, casing diameter, and casing length

However, motor diameter and length are not typically design choices for a MAV propulsion system. Therefore, an additional relationship must be utilized which relates diameter and length to required performance variables. Figure 5.6 indicates that

max rated motor torque can be used to size motor length, diameter, and therefore weight.

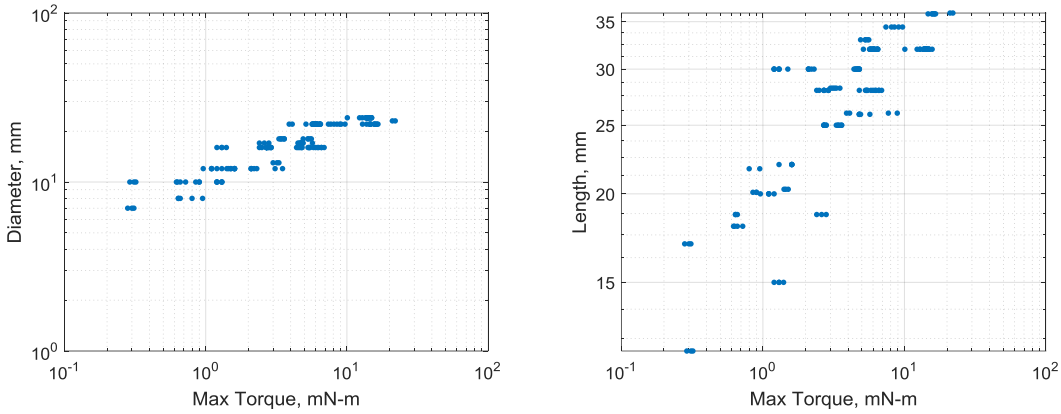

Figure 5.6: Plots of brushed motor data (log scale) showing strong correlation between max continuous torque, casing diameter, and casing length

5.1.3 Electronic Speed Controllers (ESC)

The electronic speed controller (ESC) is the interface between a motor and the onboard autopilot. The ESC receives a digital signal from the autopilot and then determines how much power to supply to motor. BLDC and brushed ESCs operate slightly differently. Brushed ESCs are simple in that they only need to switch the voltage to the motor on and off in a duty cycle, effectively changing the average voltage supplied. BLDC ESCs however, require additional circuits to supply three separate phased signals to the motor and measure back electro-motive force[54]. Despite these differences, compiled data for each type of ESC shows that both are most directly sized

by the amount of electric current passing through. Figure 5.7 shows the increase in weight as maximum allowable current increases for BLDC ESCs.

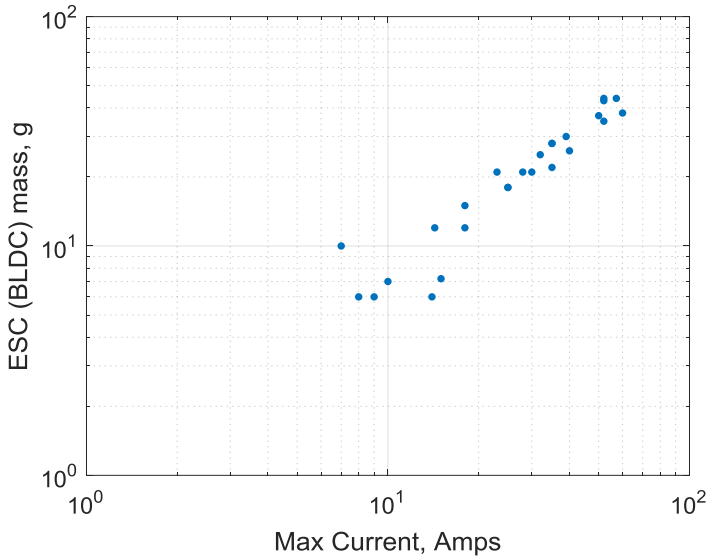

Figure 5.7: Log scale plot of ESC (BLDC) data showing strong correlation between mass and max current

For brushed ESCs, in which continuous rated current is also provided, Figure 5.8 shows a similar trend in which weight increases with both maximum current and continuous current. Maximum current is the amount of Amperage the ESC can sustain for a short time without damage. Continuous current is the amount of amps the ESC can sustain for an extended period of time.

5.1.4 Battery

Lithium polymer (LiPo) batteries are currently the preferred choice for energy storage on small-scale aerial vehicles. This preference is due to their relatively high energy density compared to older battery types, allowing greater energy storage for less

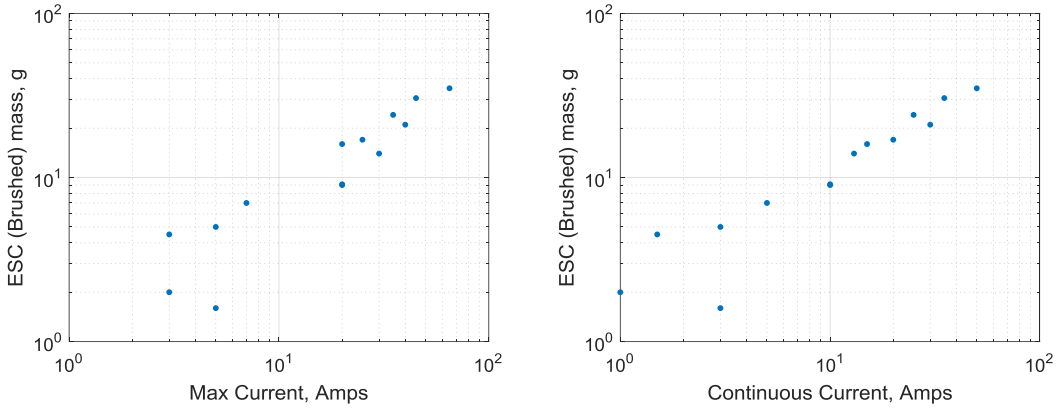

Figure 5.8: Log scale plot of ESC (Brushed) data showing strong correlation between mass and both max current and continuous current

weight. The key characteristics of a LiPo battery are the rated capacity, voltage level and number of cells (S). The capacity of a battery is given in milli-Ampere-hours (mAh). Rated capacity represents the amount of current draw the battery can sustain for one hour before being completely discharged. The nominal voltage for a LiPo battery is approximately 3.7 V. To increase voltage for larger vehicles, battery cells can be connected in series. Each LiPo cell connected in series will increase the overall voltage of the power supply by 3.7 V. The first plot in Figure 5.9 shows how battery weight increases with rated capacity. The second plot in Figure 5.9 shows how energy density effectively decreases as more cells are added. However, since adding cells increases the voltage, proportionally less current will be drawn from the battery for the same power requirements.

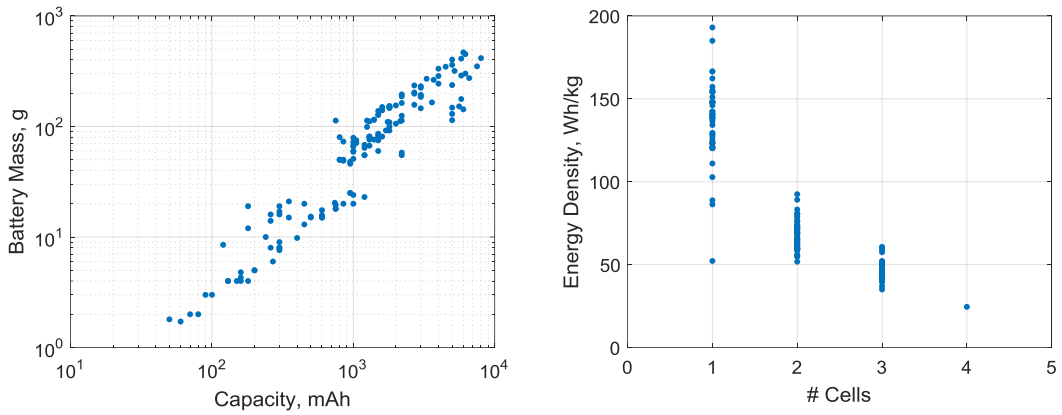

Figure 5.9: Plot of LiPo battery data showing strong correlation of mass with rated capacity and energy density with the number of cells in series

5.1.5 Airframe

The airframe of the quadrotor is the structure on which the payload and all the previously described components are mounted. For most commercially available quadrotors, the airframes are composed of high density plastic, but some may use carbon fiber. Despite the fact that these airframes can vary significantly based on manufacturer preference, Figure 5.10 indicates that for the survey of quadrotors, airframe weight is largely dependent on rotor diameter and battery mass. These relations are reasonable since rotor diameter will dictate minimum airframe dimensions, and the battery comprises a large portion of the GTOW that must be carried by the airframe.

The only components labeled in Figure 5.1, which are not sized, are the payload and the control board. The payload is part of the mission requirements and set by the designer. The control board is a digital interface for maintaining quadrotor stability and

is not dependent on the gross take-off weight of the vehicle. A small control board used on a 50 gram quad can provide equivalent stability and control for a 1000 gram quad.

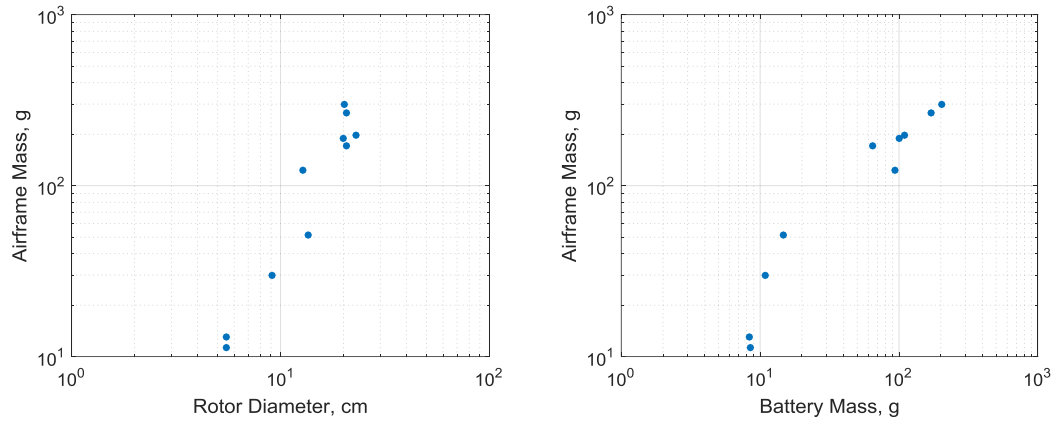

Figure 5.10: Log scale plot of airframe data showing correlation of mass with rotor diameter and battery mass

5.2 Power Requirement Calculation

A key aspect of the sizing methodology is calculating accurate power, torque, and RPM levels based on rotor geometry and required thrust. It was shown in Figure 5.4 and Figure 5.5 that power and torque requirements are strongly correlated to the motor mass. Motor power will dictate current in the ESC which will determine its weight according to Figure 5.7 and Figure 5.8. Additionally, operational power coupled with desired flight time will yield a required energy capacity which will drive the battery sizing as shown in Figure 5.9. Battery weight, in turn, is a strong factor in determining airframe weight as shown in Figure 5.10. Therefore, the rotor power, torque, and RPM requirements ultimately size the rest of the quadrotor subcomponents.

5.2.1 Rotor Aerodynamics (Hover)

Determining thrust and power is even more pertinent at low Reynolds numbers where aerodynamic forces are less understood. In this design tool, a blade element momentum theory (BEMT) function with CFD generated 2D airfoil tables is implemented. This scheme utilizes the simplicity of BEMT for rapid calculations and the high accuracy of CFD for low Reynolds number sectional aerodynamics. Specifically, the CFD program used was TURNS2D, described in detail in Chapter 2. Figure 5.11 shows the close prediction of the BEMT-CFD generated hover efficiency (Figure of Merit) with experimental measurements for the optimized micro-rotor, described in Chapter 3. This rotor is characterized by an 82 mm diameter, 0.5 chord taper ratio, -11.4^{o} twist rate, and a cambered plate airfoil section with 2.2% thickness

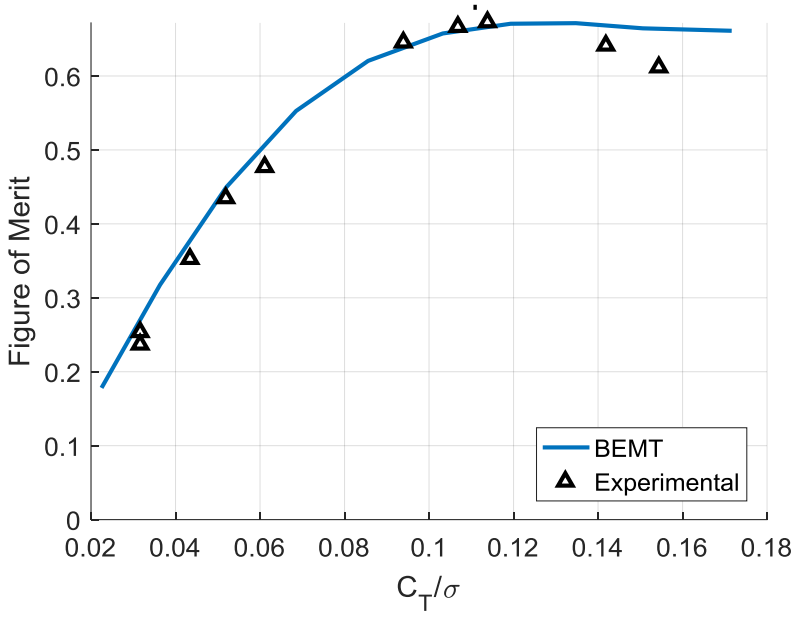

Figure 5.11: Figure of Merit vs C_T/σ validation for the a micro-rotor with 82 mm diameter, 0.5 chord taper ratio, -11.4^{o} twist rate, cambered plate airfoil

and 6.1% camber. Figure 5.12 shows the dimensional thrust, power, and torque quantities generated by BEMT-CFD validated against experimental measurements for a Syma X5 rotor. This rotor is characterized by a 135 mm diameter, 0.58 chord taper ratio, 13^{o} collective, -5^{o} twist rate, and a NACA6504 airfoil section. Both the non-dimensional and dimensional results indicate that BEMT can reliably predict low Re rotor performance when coupled with sectional CFD tables.

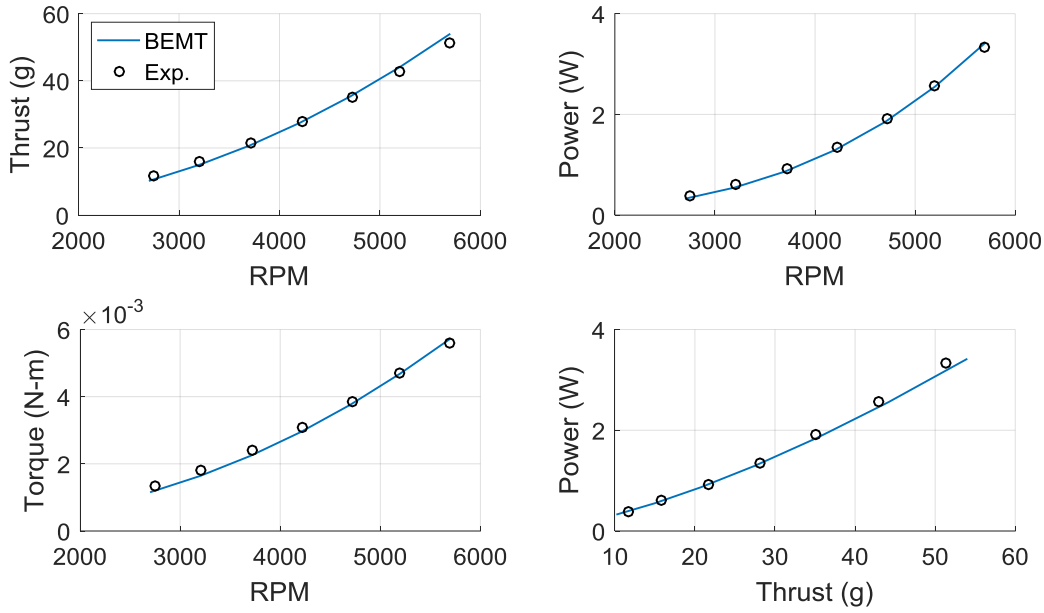

Figure 5.12: Comparison of BEMT with CFD airfoil look-up tables to experimentally tested Syma X5 rotor

5.2.2 Forward Flight Aerodynamics

In order to quickly obtain power, torque, and RPM requirements for forward (edge-wise) flight, a momentum theory analysis outlined by Leishman[52] was used. In

this theory, the power required for steady level forward flight can be separated into three terms: induced (P_i), profile (P_o), and parasitic (P_p) power. However, the equations for these terms contain empirical factors such as the induced power factor (κ), profile power factor (K), and the equivalent flat-plate area (f) for parasitic drag estimation. Due to the difference in Reynolds number, rotor design, rotor configuration, and airframe geometry between large scale helicopters and small scale quadrotors, typical values assumed for these factors are not applicable for MAVs. Currently, experimental data for rotary-wing MAV performance in forward flight is lacking, making it difficult to obtain realistic values for the power factors. A recent study at the NASA Ames Research Center wind tunnel provides force and moment measurements for 5 commercial multicopters at various flow speeds and body-pitch angles[62]. While the results of this study are useful for full vehicle lift and drag data, it does not provide much insight into the induced and profile power contributions from a typical MAV-scale rotor at multiple flight speeds. Furthermore, the vehicles tested were mostly larger (GTOW > 1.27 kg) than the vehicles or interest in the present research.

To obtain a set of validation data for rotor power in forward flight, wind tunnel tests were conducted on a typical MAV rotor which is used on the Syma X5 quadrotor. A depiction of the experimental setup used for wind tunnel testing is shown in Figure 5.13. Force and moment measurements were taken with a 6-axis load cell (Nano-17). RPM was measured by fixing magnets to the motor and recording the frequency at which they pass a Hall Effect sensor. Shaft tilt, α_s, (or body pitch for the fuselage) was precisely changed with a digital servo coupled with a pitching axis below the Nano-17.

In addition to the isolated rotor configuration shown in Figure 5.13, the Syma X5 airframe without rotors was placed on the test stand to acquire equivalent flat-plate area drag measurements. Wind tunnel speeds examined were V_∞ = 2, 4, and 6 m/s. For each wind speed, shaft tilts examined were α_s = 0, 2, 5, 10, 15, 20, 30, and 40 degrees. Nominal rotor speed for hover was determined to be 4200 RPM. Therefore, speeds of 3200, 3500, 4200, 4700, and 5200 RPM where examined at each shaft tilt angle. Additionally, measurements were repeated at each wind speed and shaft tilt with the rotor removed to obtain aerodynamic tares to correct the data in post-processing.

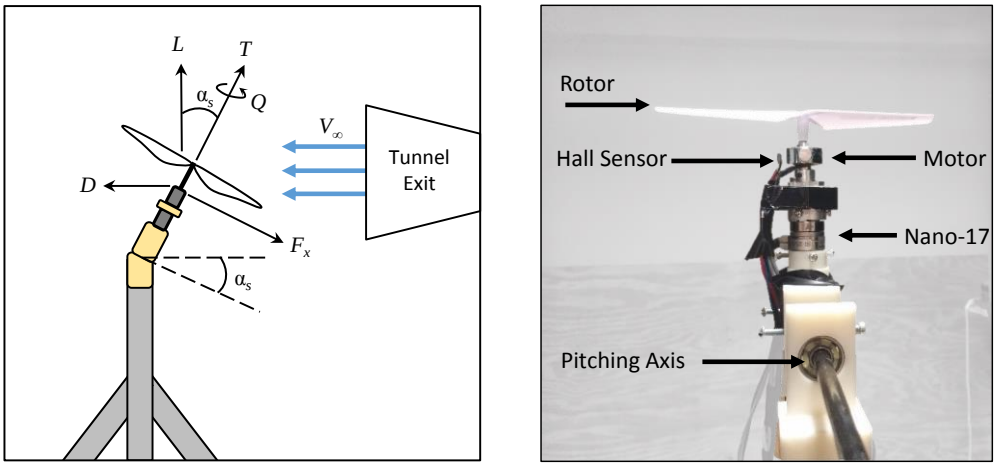

(a) Test stand schematic (with shaft tilt) (b) Actual test stand (no shaft tilt shown)

Figure 5.13: Experimental setup used for wind tunnel testing

The trim condition for steady level forward flight is met when the thrust from the rotor at required shaft tilt is able to balance the both the lift with 1/4 the GTOW (for a quadrotor) and the propulsive force with the drag at a given airspeed. The required

thrust (T), RPM, torque (Q), and shaft tilt (α_s) were interpolated from the wind tunnel data where the trim condition was met for each wind speed. By multiplying the torque and RPM, the required mechanical power from the rotor could be determined and used as validation for the calculated power. The validation for the isolated rotor power is shown in Figure 5.14. These results show that the momentum theory analysis can be valid by assuming larger power factors than would be used for full-scale helicopters. Whereas the induced power factor would be typically be assumed as $\kappa = 1.15$, the present analysis shows that $\kappa = 1.5$ is more realistic for an MAV scale rotor. It should also be noted that the profile power increases with flight speed much more than usual. This is likely due to the increased effect of viscous drag forces in the low Reynolds number regime (20,000 – 40,000 tip Re) at which these rotors operate.

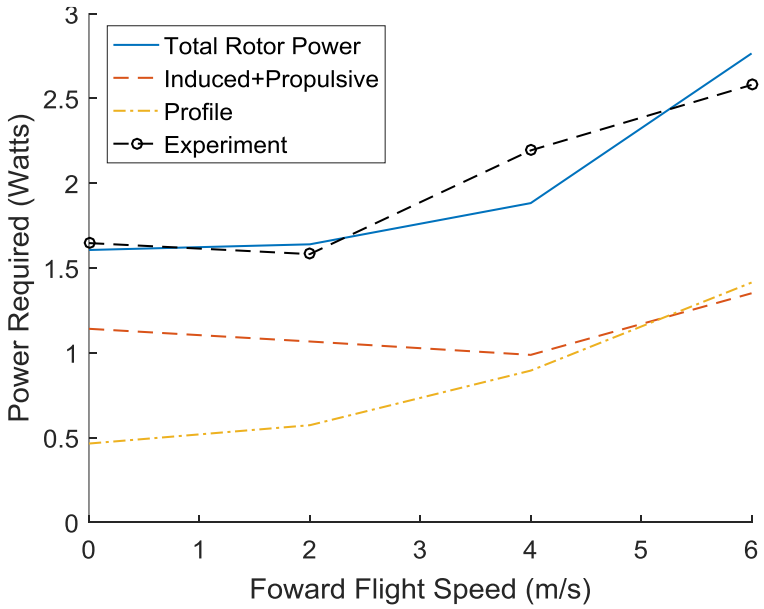

Figure 5.14: Calculated isolated rotor power compared to wind tunnel data

Using the momentum theory analysis, power estimates can be obtained at different desired air speeds. By multiplying the rotor power by the number of rotors and accounting for the drag of the fuselage at its required body pitch angle, a power estimate for cruise can be calculated. Given that the power required varies as a function of flight speed, mission segments for hover or forward flight will drain stored energy at different rates. Additionally, the primary mission requirement (such as long endurance or high speed), will determine maximum power required which will drive different choices of quadrotor subcomponents, particularly the motors.

5.3 Component Weight Regression Analysis

A parameterization technique similar to the RTL sizing methods[45] was utilized to develop empirical equations for sizing quadrotor components. In this method, the dependent variable data (component weight) and the independent variable data (e.g. rotor radius, power output, energy capacity) are first transformed into the $\log_{10}$ domain. Then, a multivariable linear regression algorithm is used to solve for the unknown coefficients which yield the best fit for the given data. The resulting equation is then transformed back to the original domain and the coefficients become the exponents of the independent variables.

This section provides examples of the predicted component weights generated by the regression analysis. Sizing equations for each quadrotor component are provided. Though validation for each sizing equation has been generated, only two examples for the rotor and battery are shown. The subsequent figures represent how

the predicted weight compares to the actual weight of each component. Two measures of accuracy for the predicted weight are provided in each figure: R^2 value and linear-fit slope.

5.3.1 Rotors

Utilizing the weight trends observed in the rotor data, a regression analysis was run on rotor mass with radius, solidity, and number of blades as the dependent variables. Figure 5.15 shows the agreement between predicted rotor weight and measured weight, particularly for lighter rotors.

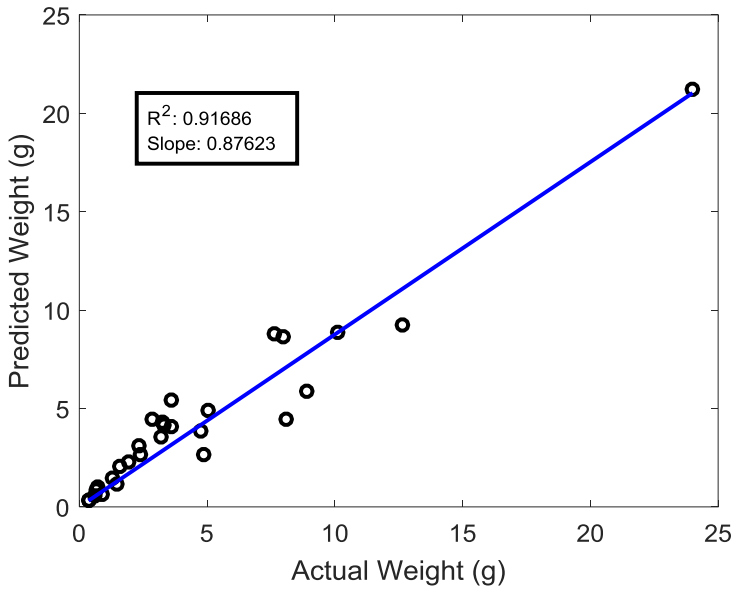

Figure 5.15: Validation of regression derived rotor weight with measured rotor weight

The resulting equation used to generate predicted rotor mass, m_R, in grams is:

$$m_R = (0.0195)R^{2.0859}\sigma^{-0.2038}N_b^{0.5344} \tag{5.1}$$

where R is the rotor radius in cm, σ is the solidity, and N_b is the number of blades.

5.3.2 Battery

Utilizing the battery weight trends with energy capacity and number of cells, a predicted weight equation was generated. Figure 5.16 shows the agreement between predicted battery weight and measured battery weight.

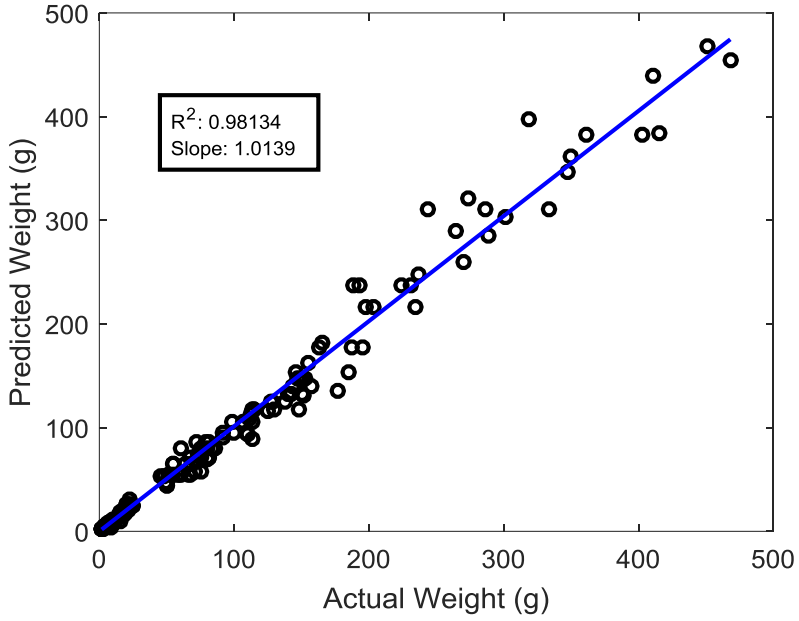

Figure 5.16: Validation of regression derived battery weight with measured battery weight

The regression equation used to generate predicted battery mass, m_B, in grams is:

$$m_B = (0.0418)C^{0.9327}S^{1.0725} \tag{5.2}$$

where *C* is battery capacity in mAh and *S* is the number of cells in series.

5.3.3 Brushless Motors

The regression equation to generate predicted BLDC motor mass, m_{BL}, in grams is:

$$m_{BL} = (0.0109)Kv^{0.5122}P^{-0.1902}(\log l_{BL})^{2.5582}(\log d_{BL})^{12.8502} \tag{5.3}$$

where *Kv* is the motor speed constant in RPM/V, *P* is the maximum rated output power in Watts, l_{BL} is the motor casing length in mm, and d_{BL} is the outer motor diameter in mm.

The equation to generate predicted BLDC motor casing length, l_{BL}, in mm is:

$$l_{BL} = (4.8910)I^{0.1751}P^{0.2476} \tag{5.4}$$

where *I* is the maximum required current for the motor in Amps and *P* is the maximum rated output power in Watts.

The equation to generate predicted BLDC motor diameter, d_{BL}, in mm is:

$$d_{BL} = (41.45){K_v}^{-0.1919}P^{0.1935} \tag{5.5}$$

where *Kv* is the motor speed constant in RPM/V and *P* is the maximum rated output power in Watts.

5.3.4 Brushed DC Motors

The equation to generate predicted brushed DC motor mass, m_{DC}, in grams is:

$$m_{DC} = (10^{-84})P^{-0.2979}{Q_{max}}^{-20.5615}(\log l_{DC})^{746}(\log d_{Dc})^{-212} \quad (5.6)$$

where *P* is the maximum rated output power in Watts, Q_{max} is the maximum output torque in mN-m, l_{DC} is the motor casing length in mm, and d_{DC} is the outer motor diameter in mm.

The equation to generate predicted brushed DC motor casing length, l_{DC}, in mm is:

$$l_{DC} = (20.83){Q_{max}}^{0.1924} \quad (5.7)$$

and the equation to generate predicted brushed DC motor casing diameter, d_{DC}, in mm is:

$$d_{DC} = (11.13){Q_{max}}^{0.2895} \quad (5.8)$$

where Q_{max} is the maximum output torque in mN-m.

5.3.5 ESC for Brushless Motors

The equation to generate predicted ESC mass for BLDC motors, m_{EBL}, in grams is:

$$m_{EBL} = (0.8013) {I_{max}}^{0.9727} \tag{5.9}$$

where I_{max} is the maximum sustainable current through the ESC in Amps.

5.3.6 ESC for Brushed DC Motors

The equation to generate predicted ESC mass for brushed motors, m_{EDC}, in grams is:

$$m_{EDC} = (0.977) {I_{max}}^{0.8483} \tag{5.10}$$

where I_{max} is the maximum burst current through the ESC in Amps.

A second equation to generate predicted ESC mass for brushed motors, m_{EDC}, in grams is:

$$m_{EDC} = (1.9) {I_{cont}}^{0.7415} \tag{5.11}$$

where I_{cont} is the maximum continuous operation current through the ESC in Amps.

5.3.7 Airframe

The equation to generate predicted airframe mass, m_A, in grams is:

$$m_A = (1.3119)R^{1.2767}{m_B}^{0.4587} \tag{5.12}$$

where R is the rotor radius in cm and m_B is the mass of the battery in grams.

5.4 Complete Sizing Algorithm

5.4.1 Description

The sizing equations and BEMT functions have been integrated into a complete parametric sizing tool. A high level schematic depicting the sizing algorithm and component interactions is shown in Figure 5.17. The required inputs are desired flight time, number of battery cells (S), rotor radius (R), solidity (σ), number of blades (N_b), payload weight, and an initial guess for GTOW. The rotor mass can be determined directly from the R, σ, and N_b inputs as shown in Eqn.(5.1). A BEMT sub-routine utilizes the input parameters to generate rotor thrust, power, torque, and RPM. These performance parameters dictate the motor requirements and weight. The GTOW dictates the type of motor to be used, typically BLDC motors for GTOW > 100g and brushed DC motors for GTOW < 100g. The power is also multiplied by flight time and

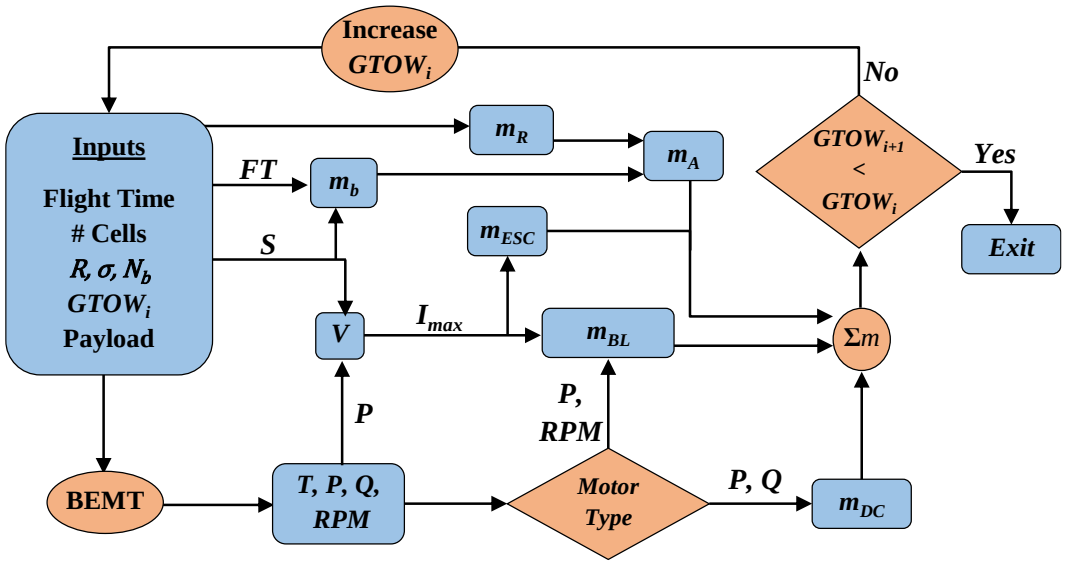

Figure 5.17: Sizing algorithm and interactions

divided by battery voltage to determine the required battery capacity (C in mAh) which is a strong driver of the battery weight as seen in Eqn. (5.2). The battery weight then factors into the airframe weight with the rotor radius via Eqn.(5.12). When all sub-component masses have been calculated, they are summed into a new GTOW. The algorithm checks that new GTOW is less than the previous GTOW. If false, the GTOW is incrementally increased and the sizing loop begins again. If true, then the calculated propulsion system is sufficient to carry out the desired mission and the algorithm stops.

5.4.2 Validation

In order to prove the utility of the proposed quadrotor MAV sizing code, a weight measurement breakdown was conducted on a variety of existing quadrotors. The major weight groups (rotors, motors, ESCs, battery, and airframe) were isolated

and weighed individually in addition to the GTOW of each vehicle. A sample of the calculated sizing results compared to the measured values for each weight group is provided in Table 4. Both brushed and brushless motor based vehicles are presented. The reported flight time and basic rotor information (R, σ, N_b, and assumed airfoil) for each vehicle were the primary sizing inputs. The payload weight contained items such as the autopilot board, LEDs, and cameras, and were not calculated by the sizing algorithm. As seen in in Table 4, the majority of percent error between measured and

Table 4: Comparison of various quadrotor weight groups to sizing code outputs

	Quadrotor	Holy Stone DFD	UDI RC U816A	Syma X5	Syma X8G	DJI Phantom 1
	Motor Type	Brushed	Brushed	Brushed	Brushless	Brushless
Rotors	Meas. (g)	1.44	1.48	7.72	34.3	28.4
	Calc. (g)	1.35	1.35	9.02	28.6	23.4
	% Error	-6.47	-9	16.9	-16.5	-17.8
Motors	Meas. (g)	13.9	13.6	15	122	203
	Calc. (g)	14.7	15.3	14.4	126	198
	% Error	5.63	12.7	-3.91	4.01	-2.73
ESCs	Meas. (g)	0.294	0.383	0.493	21.2	40.4
	Calc. (g)	0.304	0.327	0.5	24	27
	% Error	3.42	-14.6	1.36	13.1	-33.3
Battery	Meas. (g)	8.44	8.3	14.7	110	170
	Calc. (g)	7.37	8.08	15.8	84.8	186
	% Error	-12.7	-2.69	7.27	-22.6	9.46
Airframe	Meas. (g)	11.3	13.1	51.4	198	268
	Calc. (g)	11.9	12.4	53.3	227	283
	% Error	6.03	-4.79	3.58	14.9	5.58
GTOW	Meas. (g)	37.9	40.6	108	608	808
	Calc. (g)	38.3	40.9	111	615	808
	% Error	0.964	0.784	3.36	1.09	-0.011

calculated weights falls within ±10%. Furthermore, the GTOW of each vehicle is predicted well, with percent error within ±4%.

5.5 Sizing Conclusions

A design tool for low Reynolds number (10,000 – 100,000 Re) scale quadrotor aircraft is proposed. Provided with general mission requirements (endurance, speed, and payload) and basic rotor parameters, the design tool outputs required sub-component weights and total vehicle size and weight. In hover scenarios, BEMT in conjunction with CFD generated low Re airfoil tables is a fast and reliable method to calculate required torque and power. Forward flight performance data for a low Reynolds number rotor has been collected, which indicates relatively high power requirements as forward flight speed increases. This data is required to build more accurate semi-empirical models to size quadrotors for different flight speeds depending on mission requirements. However, due to the lack of low Re forward flight rotor data, more experiments should be conducted to further validate the model. Data on each quadrotor component has been compiled and analyzed to determine key weight-driving factors. Sizing equations have been derived using a log-log multivariable linear regression technique. The sizing equations have been validated against the survey of available data for each component. The sizing model has also been compared to existing quadrotor MAVs in terms of individual component weights and GTOW. Individual weight groups can be predicted generally within ±10% error and the GTOW of each vehicle is predicted within ±4% error.

Chapter 6: Conclusions and Recommendations

The goal of the present research is to understand and overcome the design challenges facing micro rotary-wing air vehicles at the aerodynamic and systemic levels and therefore expand their practical capabilities. As such, the scope of the research was divided into four primary areas: (1) Low Reynolds number sectional aerodynamics, (2) Micro-rotor optimization experiments, (3) High endurance quadrotor design and construction, and (4) MRAV sizing algorithm development.

6.1 Low Reynolds Number Sectional Aerodynamics

Chapter 2 explains the studies conducted with TURNS2D as a method of understanding low Re aerodynamics and resulted in the following conclusions:

1. The results from TURNS2D are compared with available experimental C_l, C_d, C_m, and C_p data, as means of validation. Overall, the calculated values from TURNS2D agree quite well with the experimental measurements at low Re. The C_l, C_d, and C_p curves for the NACA 0009 at Re = $5x10^4$ correlate very well for low to moderate α. The calculated and experimental C_l, C_d, and C_m curves for the NACA 0012 at various Re between 10^4-10^6 are in good agreement. TURNS2D also predicts the performance trends of increasing airfoil camber and thickness at Re = 10^4 quite well.

2. The results from TURNS2D show the extreme sensitivity of airfoil performance to changing Re below 10^5, particularly for conventional airfoils like the NACA 0012.

As Re decreases there is an increase in drag, particularly due to the shrinking of the drag bucket, and a large decrease in lift. C_{lmax} decreases by approximately 46% between Re = 10^5 and Re = 10^4. Unlike performance results above Re = 10^5, the lift curves are highly non-linear, particularly for $\alpha < 5^o$, and a single lift-curve-slope value may not be appropriate. It should also be noted that the drag bucket is significantly smaller at Re < 10^5 and the minimum drag noticeably increases.

3. The effect of thickness (1, 3, and 5%) for simple flat plates was examined at Re = 10^4. It is evident that as flat plate thickness-to-chord (*t/c*) decreases, lift and drag characteristics improved, with the 1% flat plate being the most efficient.

4. The effect of camber (3, 6, and 9%) on thin plate airfoils was examined at Re = 10^4. As camber is increased, both the C_l and C_d increase and the lift-to-drag is significantly improved compared to flat plate airfoils of the same thickness. For a low Re wing design to achieve high lift-to-drag, approximately 6% camber appeared optimum. On the other hand, 9% camber could be utilized if maximum lift is a stronger design factor.

5. The effect of camber on thin NACA airfoils (NACA 0003, 2403, 4403, 6403) was also examined at Re = $2x10^4$ and Re = 10^5. The high camber airfoils (NACA 4403 and 6403) were shown to have the highest lift-to-drag at both Re. Additionally, the lift-to-drag curves are more similar at Re = $2x10^4$ and more differentiated at Re = 10^5.The symmetric NACA 0003 airfoil performance changes very little with an

increase in Re. As camber is increased, the lift-to-drag improves by a greater margin. This result indicates that the degree to which an airfoil's characteristics effect its performance is also dependent on Re.

6. Examination of the boundary layer at low Re shows significant differences between thin plate airfoils and thicker airfoils. The NACA 0012 is more susceptible to trailing edge separation at low Re whereas the flat plate trips the laminar boundary layer at the leading edge, allowing it to reattach. The reattachment of the upper boundary layer preserves lower surface pressure and therefore allow the flat plate to provide more lift than the NACA 0012 at $Re < 5x10^4$.

7. When the NACA 0012 is placed in a reversed configuration at $Re = 2x10^4$, its lift qualities improve. This effect is due to the sharp leading edge creating an early laminar separation bubble similar to the flat plate's. Despite the fact that the NACA 0012 has the same maximum thickness in either configuration, this result indicates that the distribution of the thickness along the chord, particularly at the LE, has an effect on airfoil performance at low Re that is counter to what is expected at high Re.

6.2 Micro-Rotor Experiments

Chapter 3 details a comprehensive, multi-parameter investigation to determine how rotor characteristics, such as airfoil section, twist, chord taper, and number of

blades, effect low Reynolds number rotor performance and resulted in the following conclusions:

1. Similar to the findings in Chapter 2, thin airfoils with moderate camber were found to improve aerodynamic efficiency. It was observed in the thickness-to-chord and solidity experiments that a thin (t/c = 1.2%) plate with 6.1% camber is the optimal airfoil design, provided the rotor blade is fabricated from carbon fiber composite.

2. The results of the N_b and solidity experiments indicated that 2-bladed rotors with a large chord (c = 21.4 mm) outperform rotors of the same solidity with 3 or 4 blades.

3. The results of the chord taper experiments showed that highly tapered blades (*CTR* 0.25 - 0.5) improve rotor performance compared to rectangular blades.

4. The results of the blade twist experiments indicated that -10° to -20° of twist per blade is required to further improve performance.

5. A final rotor was designed which incorporated all of the individual optimal parameters determined from the previous tests. This rotor design achieved a maximum *FM* of 0.66 which represents 34% efficiency increase over the initial baseline rotor.

6.3 High Endurance Quadrotor

Chapter 4 focused on designing and optimizing a MAV-scale quadrotor helicopter for maximum hover endurance. This has been achieved through systematic

testing of each component, including the motors, gear transmission systems, and battery, as well as significantly reducing the airframe weight of the quadrotor. Optimization studies of the quadrotor subsystems yielded the following results:

1. Brushed motors are more suitable than brushless motors for use on an MAV-scale quadrotor. Brushless motors and electronic speed controllers (ESCs) are heavier than brushed motors and brushed ESCs. It was determined that ESCs have a much more pronounced decrease in efficiency in brushless motor systems than in brushed motor systems. It was also determined that geared transmissions are able to provide substantial performance boosts for brushed motor systems but only marginally effect brushless motors. The fundamental reason for this is the fact that brushed motors perform better at high rpms and low torque while brushless motors have higher efficiencies at both high rpm and high torque, which cannot be achieved by a gearbox. For these reasons, the three most efficient brushed motors were considered in more extensive optimization studies.
2. Identically sized brushed motors with different internal resistances will exhibit different power loading and thrust/volt characteristics. High resistance brushed motors (3.3 Ohms) exhibit higher electrical power loading and lower thrust/volt compared to lower resistance motors (1.7 and 2.3 Ohms).
3. Pairing brushed motors with larger gear ratios has the effect of improving electric power loading while reducing thrust/volt. Smaller gear ratios decrease EPL while increasing thrust/volt. For the same gear ratio, high resistance brushed motors had higher EPL than low resistance motors but produced less thrust/volt. Brushed

motors with 4:1 and 5.33:1 gear ratios had the highest overall efficiency while still being able to supply the minimum thrust/volt for controlled flight.

4. Li-poly Battery voltage does not remain constant as it is discharged. The amount of voltage drop is dependent on battery geometry. Rectangular batteries show less voltage drop than cylindrical batteries. The lowest sustainable voltage for 3.7 V rated Li-poly batteries is effectively 3.6V. Energy density is also dependent on battery geometry. Cylindrical batteries have longer endurance for their mass than rectangular batteries at the required current draw. Due to this characteristic, the 650 mAh and 900 mAh cylindrical batteries were studied in the full vehicle configuration.
5. Vehicle control and stability were provided by a lightweight (2 g) processor-sensor board (GINA-Mote). A telemetry setup with a base station was used to wirelessly update the feedback gains, trim inputs, and pilot commands to the vehicle in flight.
6. The quadrotor airframe was fabricated from an ultra-lightweight carbon fiber-balsa wood composite for significant weight reduction. This comprises only 7.4% of the optimized quadrotor gross weight compared to 30 - 50% for other similarly sized COTS quadrotors.
7. The highest predicted endurance times on the gimbal test setup were achieved with the 5.33:1 gear ratio. The 650 mAh and 900 mAh batteries resulted in endurances of 40.5 minutes and 49 minutes, respectively, during gimbal testing. . In free hover flight tests, the maximum hover endurance achieved with the 650 mAh battery was

31 minutes, which is almost double the hover endurance of any of the existing MAV-scale helicopters.

6.4 MRAV Sizing Algorithm

Chapter 5 described the development of a design tool for low Reynolds number (10,000 – 100,000 Re) scale quadrotor aircraft and resulted in the following conclusions:

1. Provided with general mission requirements (endurance, speed, and payload) and basic rotor parameters, the design tool is able to output required sub-component weights and total vehicle size and weight.

2. In hover scenarios, BEMT in conjunction with CFD generated low Re airfoil tables is a fast and reliable method to calculate required torque, RPM, and power.

3. Forward flight performance data for a low Reynolds number rotor has been collected, which indicates relatively high power requirements as forward flight speed increases. At these Reynolds numbers, the profile power contributes much more to total forward flight power requirements compared to profile power for large-scale rotors.

4. The semi-empirical analysis is able to sufficiently predict quadrotor power requirements for different flight speeds depending on mission requirements.

5. Data on each quadrotor component has been compiled and analyzed to determine key weight-driving factors. Sizing equations have been derived using a log-log multivariable linear regression technique.

6. The sizing equations have been validated against the survey of available data for each component. The sizing model has also been compared to existing quadrotor MAVs in terms of individual component weights and GTOW. Individual weight groups can be predicted generally within ±10% error and the GTOW of each vehicle is predicted within ±4% error.

6.5 Recommendations for Future Work

In order to directly expand upon the knowledge provided in the present study, several areas of possible research are listed.

1. It was observed in the CFD studies that the airfoil performance characteristics are not modeled well by TURNS2D around stall angles of attack. Future work which improves detached flow simulation should be investigated. Furthermore, variations in freestream turbulence could not be modeled at Re below 100,000 when the boundary layer transition model was on. As a result, airfoil performance sensitivity to turbulence at low Re could not be investigated. Since previous experimental studies have shown that increased turbulence can actually be beneficial at low Re, improved turbulence models for TURNS2D could lead to better predictive capabilities and new insights.

2. In the micro-rotor experiments, the effects of twist and taper were not examined as thoroughly as other parameters. Twist and taper were only incorporated as linear functions of blade span. To further optimize rotor performance, future studies should focus on other methods of tapering chord length and twisting blade pitch. This may require the use of complex, machined blade molds which allow for precise, non-linear variations in twist, taper, and camber.
3. In the development of the high endurance quadrotor, many areas were simultaneously improved. As such, it is currently not clear which improvement resulted in the most increase of vehicle endurance. Sensitivity studies which decouple aerodynamic and electric propulsion improvements should provide insight into which factor is more critical for improving vehicle endurance.
4. The current high endurance quadrotor was initially designed to fit within the 6x6 inch planform constraint set by DARPA for MAVs. However, this doesn't not appear to be a realistic constraint considering the specified maximum weight for MAVs is 100 g. The current vehicle weighs only 45 g but its rotor diameter needed to be lengthened to 4.5 inches to provide sufficient thrust while maintaining high efficiency. Therefore, future quadrotor prototypes should be designed with a 100 g target GTOW while disregarding the planform constraint to attempt to achieve a 1 hour flight endurance.
5. The next iterations of the high endurance quadrotor should also account for a payload, such as a micro video camera, in the design to demonstrate useful mission capabilities.

6. Forward flight power prediction for MRAVs has only been briefly explored in the present study because of time constraints. Though the momentum theory model showed good correlation with the experimentally measured power, only one rotor design was examined. Due to the lack of low Re forward flight rotor data, more wind tunnel experiments should be conducted, especially with the optimum hovering rotor, to further validate the forward flight model.
7. Currently, the MRAV sizing model described in the present study is able to provide reasonable performance and component weight predictions for a given set of user inputs. However, it does not have the capability to optimize designs based on minimum weight, maximum flight time, or cruising flight speed. Future work on the design algorithm should focus on implementing optimization methods.
8. The design code has only been validated based on existing quadrotor vehicles. Once the MRAV sizing code is capable of optimization, it would be useful to validate it by designing a new vehicle for a target capability, such as 1 hour endurance, and then fabricating and flight testing the vehicle to compare its actual capabilities to the designed capabilities.

Bibliography

[1] McMichael, J. M., and C. M. S. Francis USAF (Ret.). "Micro Air Vehicles Towards New Dimension in Flight." *U.S. Department of Defense Weapons Systems Technology Information Analysis Center (WSTIAC) Newsletter* , [online journal] Vol. 1, No. 2 (April 2000), URL: http://www.darpa.mil/tto/MAV/mav Auvsi.html. [cited 16 March 2014].

[2] "AeroVironment Develops World's First Fully Operational Life-Size Hummingbird-Like Unmanned Aircraft for DARPA," AeroVironment, Inc., URL: http://investor.avinc.com/releasedetail.cfm?releaseid=550835, Feb 17, 2011, cited Dec. 2016.

[3] Coleman, D., Benedict, M., Hrishikeshavan, V., and Chopra, I., "Design, Development and Flight-Testing of a Robotic Hummingbird," *AHS 71st Annual Forum*, Virginia Beach, Virginia, edited by A. H. Society, May 2015.

[4] Grasmeyer, J., and Keenon, M., "Development of the Black Widow Micro Air Vehicle," *39th Aerospace Sciences Meeting and Exhibit*, Reno, NV, AIAA Paper No. 2001-0127, Jan. 2001.

[5] Kushleyev, A., Mellinger, D., Powers, C. and Kumar, V., "Towards A Swarm of Agile Micro Quadrotors," *Autonomous Robots*, Vol. 35, No. 4, pp. 287–300, Nov. 2013.

[6] Bohorquez, F,. *Rotor Performance and System Design of an Efficient Coaxial Rotary Wing Micro Air Vehicle*, Ph. D. Dissertation, Department of Aerospace Engineering, University of Maryland, 2007.

[7] Gao, Yuan. "What makes the quadcopter design so great for small drones?" *Quora*, [website], URL: http://www.quora.com/Unmanned-Aerial-Vehicles-UAV/What-makes-the-quadcopter-design-so-great-for-small-drones [cited 17 March 2014]

[8]"Cheerson CX-10," UAV Systems International, URL: https://uavsystemsinternational.com/product/cheerson-cx-10/, Accessed: January 2017.

[9] Heer, M., "Heli-Max 1Si Quadcopter SLT 2.4GHz RTF w/Camera Review," Cgroups, URL: http://www.rcgroups.com/forums/showthread.php?t=2032113, Accessed: March 2014.

[10] "Scorpion Mini Multicopter RTF w/2.4GHz Radio – Blue," HeliProz, URL: http://www.heliproz.com/Scorpion-Mini-Multicopter-RTF-w_24GHz-Radio-Blue/productinfo/SCRPNBLU/, March 2014.

[11] Harrington, A., *Optimal Propulsion System Design for a Micro Quad Rotor*, M.S. Thesis, Department of Aerospace Engineering, University of Maryland, 2011.

[12] "Walkera QR W100S Wi-Fi FPV Micro Quad-Copter IOS And Android Compatible (BNF)," HobbyKing, URL:https://www.hobbyking.com/hobbyking/store/__49782__Walkera_QR_W100S_Wi_Fi_FPV_Micro_Quad_Copter_IOS_And_Android_Compatible_BNF_.html, Accessed: March 2014.

[13] "Nano QX RTF with SAFE," BLADE, URL: http://www.bladehelis.com/Products/Default.aspx?ProdID=BLH7600#quickOverview, Accessed: January 2017.

[14] Liang, O., "DIY MINI QUADCOPTER," URL: https://oscarliang.com/diy-mini-quadcopter/, Accessed: January 2017.

[15] Ramasamy, M., Johnson, B., and Leishman, J. G., "Understanding the Aerodynamic Efficiency of a Hovering Micro-Rotor," *Journal of American Helicopter Society*, Vol. 53, No. 4, October 2008, pp. 412–428.

[16] McMasters, J. H., Henderson, M. L., "Low Speed Single-Element Airfoil Synthesis", NASA Langley Research Center, *The Science and Technology of Low Speed and Motorless Flight*, Hampton, VA, March 29-30, 1979.

[17] Mueller, T., J., "Aerodynamic Measurements at Low Reynolds Numbers for Fixed Wing Micro-Air Vehicles", *RTO AVT/VKI Special Course on Development and Operation of UAVs for Military and Civil Applications*, VKI, Belgium, September 13-17, 1999.

[18] Abbott, I., H., and Von Doenhoff, A., E., "Theory of Wing Sections", 2nd ed., Dover Publications, Inc., New York, New York, 1959.

[19] Mueller, T. J., and DeLaurier, J. D., "Aerodynamics of small vehicles", *Annual Review of Fluid Mechanics*, Vol. 35, pp. 89–111, January 2003.

[20] Tsuchiya, T., Numata, D., Suwa, T., and Asai. K., "Influence of Turbulence Intensity on Aerodynamic Characteristics of an NACA 0012 at Low Reynolds Numbers", *51st AIAA Aerospace Sciences Meeting including the New Horizons Forum and Aerospace Exposition*, 07 - 10 January 2013, Grapevine, Texas.

[21] Schmitz, F. W., "Aerodynamik des Flugmodells", C. J. E. Volckmann Nachf. E. Wette, Berlin-Charlottenburg, 1942.

[22] Hoerner, S.F., "Fluid-Dynamic Lift: Practical Information on Aerodynamic and Hydrodynamic Lift", 2 Ed., Published 1985.

[23] Selig, M. S., Donovan, J. F., and Fraser, D. B., "Airfoils at Low Speeds", SoarTech Publications, Virginia Beach, VA, 1989.

[24] Mueller, T. J., and Batill, S. M., "Experimental studies of separation on a two-dimensional airfoil at low Reynolds numbers", *AIAA Journal*, Vol. 20, No. 4, pp. 457–463, 1982.

[25] Okamoto, M., Yasuda, K., and Azuma, A., "Aerodynamic Characteristics of the Wings and Body of a Dragonfly", *The Journal of Experimental Biology* No. 199, pp. 281–294 (1996).

[26] Laitone, E. V., "Wind tunnel tests of wings at Reynolds numbers below 70000", *Experiments in Fluids*, Vol. 23, pp. 405–409, 1997.

[27] Williamson, G. A., et.al., "Summary of Low-Speed Airfoil Data", Vol. 5, Department of Aerospace Engineering, University of Illinois at Urbana-Champaign, 2012.

[28] Lyon, C. A., Broeren, A.P., and Giguère, P., Gopalarathnam, A., Selig, M.S., "Summary of Low-Speed Airfoil Data", Vol. 3, Department of Aerospace Engineering, University of Illinois at Urbana-Champaign, 1997.

[29] Selig, M. S., Lyon, C. A., Giguere, P., Ninham, C. P., AND Guglielmo, J. J., "Summary of Low-Speed Airfoil Data", Vol. 2. Publisher: SoarTech Publications, Virginia Beach, Virginia, 1996.

[30] McAurthur, J., *Aerodynamics of Wing at Low Reynolds Numbers: Boundary Layer Separation and Reattachment*, Ph.D. Dissertation, Department of Aerospace and Mechanical Engineering, University of Southern California, 2008.

[31] Ohtake, T., Nakae., Y., Motohashi, T., "Nonlinearity of the Aerodynamic Characteristics of NACA 0012 Aerofoil at Low Reynolds Numbers", *Japanese Society for Aeronautical and Space Science Papers*, Vol. 55, No. 644, pp. 439–445, 2007.

[32] Bush, B., L., *A Computational Study of the Force Generation Mechanisms in Flapping-Wing Hovering Flight*, Ph. D. Dissertation, Department of Aerospace Engineering, University of Maryland, 2013.

[33] Medida, S. and Baeder, J. D., "Application of the Correlation-based $\gamma - \overline{Re_{\theta t}}$ Transition Model to the Spalart-Allmaras Turbulence Model", *20th AIAA Computational Fluid Dynamics Conference*, 27 - 30 June 2011, Honolulu, Hawaii.

[34] Kroo, I., and Kunz, P., "Analysis and Design of Airfoils for use at Ultra-Low Reynolds Numbers," Fixed and Flapping Wing Aerodynamics for Micro AirVehicle

Applications, edited by T. J. Mueller, *Progress in Astronautics and Aeronautics*, AIAA, Reston, VA, 2001, pp. 503-517.

[35] Kunz., P.J., *Aerodynamics and Design for Ultra-Low Reynolds Number Flight*, Ph.D. Dissertation, Department of Aeronautics and Astronautics, Stanford University, CA, June 2003.

[36] Benedict, M., *Fundamental Understanding of the Cycloidal-Rotor concept for Micro Air Vehicle Applications*, Ph. D. Dissertation, Department of Aerospace Engineering, University of Maryland, 2010.

[37] Yang, K., *Aerodynamic Analysis of an MAV-Scale Cycloidal Rotor System Using a Structured Overset RANS Solver*, M.S. Thesis, Department of Aerospace Engineering, University of Maryland, 2010.

[38] Sabatino, F., *Quadrotor Control: Modeling, Nonlinear Control Design, and Simulation*, M.S. Thesis, Department of Electrical Engineering, KTH Royal Institute of Technology, Sweden, 2015.

[39] Fraundorfer, F., et. al., "Vision-Based Autonomous Mapping and Exploration Using a Quadrotor MAV," *IEEE/RSJ International Conference on Intelligent Robots and Systems*, Vilamoura, Algarve, Portugal, October 7-12, 2012.

[40] Hein, B., and Chopra, I., "Hover Performance of a Micro Air Vehicle: Rotors at Low Reynolds Number," *International Specialists' Meeting Unmanned Rotorcraft: Design, Control and Testing*, Chandler, AZ, January 18–20, 2005.

[41] Bouabdallah, S., Siegwart, R., "Design and Control of a Miniature Quadrotor," *Advances in Unmanned Aerial Vehicles*, Springer Netherlands, 2007.

[42] Ampatis, C., Papadopoulos, E. "Parametric Design and Optimization of Multi-Rotor Aerial Vehicles." *Applications of Mathematics and Informatics in Science and Engineering*, pp. 1-25. Springer International Publishing, 2014.

[43] Bershadsky, D., Haviland, S., and Johnson, E. N., "Electric Multirotor Propulsion System Sizing for Performance Prediction and Design Optimization," *AIAA SciTech 2016*, AIAA, San Diego, CA, 2016.

[44] "xcopterCalc - Multicopter Calculator" http://www.ecalc.ch/xcoptercalc.php Accessed: November 2016.

[45] Stepniewski, W. Z., and Shinn, R. A., "A Comparative Study of Soviet vs. Western Helicopters: Part 2 - Evaluation of Weight, Maintainability, and Design Aspects of Major Components," NASA AVRADCOM Technical Report 82-A- 10, 1983.

[46] Srinivasan, G. R., and Baeder, J. D., "TURNS: A Free-Wake Euler/Navier-Stokes Numerical Method for Helicopter Rotors", *AIAA Journal*, Vol. 31, No. 5: Technical Notes, 1992.

[47] Medida, S. and Baeder, J. D., "Application of the Correlation-based $\gamma - \overline{Re_{\theta t}}$ Transition Model to the Spalart-Allmaras Turbulence Model", *20th AIAA Computational Fluid Dynamics Conference*, 27 - 30 June 2011, Honolulu, Hawaii.

[48] Lutz, T., Würz, W., and Wagner, S., "Chapter 9: Numerical Optimization and Wind-Tunnel Testing of Low Reynolds-Number Airfoils", Fixed and Flapping Wing Aerodynamics for Micro Air Vehicle Applications, Mueller, TJ., editor, AIAA, Vol. 195, pp. 169-190, 2001.

[49] Sheldahl, R. E., and Klimas, P. C., "Aerodynamic Characteristics of Seven Symmetrical Airfoil Sections Through 180-Degree Angle of Attack for Use in Aerodynamic Analysis of Vertical Axis Wind Turbines", Sandia National Laboratories, Albuquerque, New Mexico, printed March 1981.

[50] "Objet Eden350V," Statasys, [website] URL: http://www.stratasys.com/3d-printers/design-series/precision/objet-eden350v [cited 22 March 2014]

[51] Bohorquez, F., Pines, D. and Samuel, P. D., "Small Rotor Design Optimization Using Blade Element Momentum Theory and Hover Tests," *Journal of Aircraft*, Vol. 47, No. 1, Jan. – Feb. 2010, pp. 268-283.

[52] Leishman, J. G., *Principles of Helicopter Aerodynamics*, 2nd ed., Cambridge University Press, New York, 2006, pp. 99-121.

[53] Petricca, L., Per Ohlckers, and Grinde, C., "Micro- and Nano-Air Vehicles: State of the Art," *International Journal of Aerospace Engineering*, Volume 2011, Article ID 214549, February 2011.

[54] Harrington, A., and Kroninger, C.,"Characterization of Small DC Brushed and Brushless Motors." ARL-TR-6389, March 2013.

[55] "Brushed vs Brushless Motors," thinkRC, [website] URL: http://www.thinkrc.com/faq/brushless-motors.php, Accessed: January 2017.

[56] Hammonda, G., Hazeldinea, T., "Indicative Energy Technology Assessment of Advanced Rechargeable Batteries," *Applied Energy*, Volume 138, January 2015, Pages 559–571

[57] Mehta, A., and Pister, K., "WARPWING: A Complete Open Source Control Platform for Miniature Robots," *Proceedings of the 2010 IEEE/ RSJ International Conference on Intelligent Robots and Systems* (IROS 2010), Curran Associates, Inc., Oct. 2010, pp. 5169–5174.

[58] Benedict, M., Shrestha, E., Hrishikeshavan, V., and Chopra, I., "Development of a Micro Twin-Rotor Cyclocopter Capable of Autonomous Hover," *Journal of Aircraft*, Vol. 51, No. 2, March-April 2014.

[59] Georgy, J., Noureldin, A.,Korenberg, M., and Bayoumi, M., "Modeling the Stochastic Drift of a MEMS-Based Gyroscope in Gyro/Odometer/ GPS Integrated Navigation," IEEE Transactions on Intelligent Transportation Systems, Vol. 11, No. 4, Dec. 2010, pp. 856–872. doi:10.1109/TITS.2010.2052805

[60] Thong, Y. K., Woolfson, M. S., Crowe, J. A., Hayes-Gill, B. R., and Challis, R. E., "Dependence of Inertial Measurements of Distance on Accelerometer Noise," Measurement Science and Technology, Vol. 13, No. 8, 2002, pp. 1163–1172. doi:10.1088/0957-0233/13/8/301

[61] Winslow, J., Benedict, M., Hrishikeshavan, V., and Chopra, I., "Design, Development, and Flight Testing of a High Endurance Micro Quadrotor Helicopter," *AHS International Specialists' Meeting on Unmanned Rotorcraft Systems*, AHS, Chandler, Arizona, 2015.

[62] Russell, C., Jung, J., Willink, G., Glasner, B., "Wind Tunnel and Hover Performance Test Results for Multicopter UAS Vehicles," *AHS 72nd Annual Forum*, AHS, West Palm Beach, Florida, May 16-19, 2016.